Fall 12-20-2019

Nanomedicine-driven neuropathic pain relief in rat model is associated with macrophage polarity and mast cell activation

Muzamil Saleem

NANOMEDICINE-DRIVEN NEUROPATHIC PAIN RELIEF IN RAT MODEL IS ASSOCIATED WITH MACROPHAGE POLARITY AND MAST CELL ACTIVATION

A Dissertation

Submitted to the Bayer School of Natural & Environmental Sciences

Duquesne University

In partial fulfillment of the requirements for

the degree of Doctor of Philosophy

By

Muzamil Saleem

December 2019

NANOMEDICINE-DRIVEN NEUROPATHIC PAIN RELIEF IN RAT MODEL IS ASSOCIATED WITH MACROPHAGE POLARITY AND MAST CELL ACTIVATION

By

Muzamil Saleem

Approved September 13th, 2019

_____ Dr. John A. Pollock Professor of Biological Sciences (Committee Chair)	_____ Dr. Jelena M. Janjic Associate Professor of Pharmaceutical Sciences (Committee Member)
_____ Dr. Benedict J. Kolber Associate Professor of Biological Sciences (Committee Member)	_____ Dr. Nicholas F. Fitz Assistant Professor of Environmental and Occupational Health (Committee Member)
_____ Dr. Philip Paul Reeder Dean and Professor, Bayer School of Natural & Environmental Sciences	_____ Dr. Joseph R. McCormick Chair, Biological Sciences Professor of Biological Sciences

ABSTRACT

NANOMEDICINE-DRIVEN NEUROPATHIC PAIN RELIEF IN RAT MODEL IS ASSOCIATED WITH MACROPHAGE POLARITY AND MAST CELL ACTIVATION

By

Muzamil Saleem

December 2019

Dissertation supervised by John A. Pollock.

Adapted from:

Saleem, M., *Deal, B., Nehl, E., Janjic, J., Pollock, J. A. Nanomedicine-driven neuropathic pain relief in a rat model is associated with macrophage polarity and mast cell activation. Acta Neuropathol Commun. 2019; 7: 108, doi: 10.1186/s40478-019-0762-y.*

Saleem, M.*, Stevens, A. M., Deal, B., Liu, L., Janjic, J., Pollock, J. A. A New Best Practice for Validating Tail Vein Injections in Rat with Near-infrared-Labeled Agents. J. Vis. Exp. (146), e59295, doi:10.3791/59295 (2019).*

Jelena M. Janjic, Kiran Vasudeva, ***Muzamil Saleem****, Andrea Stevens, Lu Liu, Sravan Patel, John A. Pollock. Low-dose NSAIDs reduce pain via targeted nanoparticle delivery to*

neuroinflammation in Rat. Journal of Neuroimmunology 2018; 318, doi: 10.1016/j.jneuroim.2018.02.010.

We explored the immune neuropathology underlying multi-day relief from neuropathic pain in a rat model initiated at the sciatic nerve by using a nanoemulsion-based nanomedicine as a biological probe. The nanomedicine is theranostic: both therapeutic (containing celecoxib drug) and diagnostic (containing near-infrared fluorescent (NIRF) dye) and is small enough to be phagocytosed by circulating monocytes. A model of neuropathic pain is initiated by tying four 1mm spaced knots around the sciatic nerve with chromic gut suture, which results in neuroinflammation, and a resultant pain-like behavior manifests. We show that pain-like behavior reaches a plateau of maximum hypersensitivity 8 days post-surgery, and is the rationale for intravenous delivery at this time-point. Pain relief is evident within 24 hours, lasting approximately 6 days. The ipsilateral sciatic nerve and associated L4 and L5 dorsal root ganglia (DRG) tissue of both nanomedicine and control (nanoemulsion without drug) treated animals was investigated by immunofluorescence and confocal microscopy at the peak of pain relief (day 12 post-surgery), and when pain-like hypersensitivity returns (day 18 post-surgery). At day 12, a significant reduction of infiltrating macrophages, mast cells and mast cell degranulation was observed at the sciatic nerve following treatment. In the DRG, there was no effect of treatment at both day 12 and day 18 on the numbers of macrophages and mast cells. Conversely, at the DRG, there is a significant increase in macrophage infiltration and mast cell degranulation at day 18. The treatment effect on immune pathology in the sciatic nerve was investigated further by assessing the expression of macrophage cyclooxygenase-2 (COX-2)—the drug target--and extracellular prostaglandin E2 (PGE2), as well as the proportion of M1 (pro-inflammatory) and

M2 (anti-inflammatory) macrophages. At day 12, there is a significant reduction of COX-2 positive macrophages, extracellular PGE2, and a striking reversal of macrophage polarity. At day 18, these measures revert to levels observed in control-treated animals. Here we present a new paradigm of immune neuropathology research, by employing a nanomedicine to target a mechanism of neuropathic pain—resulting in long-lasting pain relief--whilst revealing novel immune pathology at the injured nerve and associated DRG.

The pathology of pain relief that these studies reveal, highlights a crucial concept: that a single nanomedicine dose targeted to general peripheral neuroinflammation, may not be sufficient—that a treatment plan could be modified to firstly include additional treatment points, and secondly target the associated DRG in order to dampen the inflammation and pain signaling emanating there.

DEDICATION

I dedicate this thesis to my wife, Alexandra Caffee, who I met at the beginning of my doctoral studies, and whose patience, love and support has been unwavering—and essential--throughout.

ACKNOWLEDGMENT

I am grateful for the mentorship and guidance of Dr. John A. Pollock, my PhD advisor. I learned a considerable amount from his graceful, and honest style of mentorship. He helped to develop my abilities to exercise good science. He reinforced in me the importance of zooming out of a scientific question, thinking dynamically, and to be confident in my creativity of thought. It was a pleasure to watch him teach, as his TA – I learned an awful lot. And, he was very patient with me. I will always have a lot of respect for John. He is the coolest. Thank you.

I am thrilled to have both collaborated with the lab of Dr. Jelena M. Janjic and to have her provide expert guidance and wonderful support as a committee member. I will always be grateful for the privilege of working in a multidisciplinary collaboration that was very impactful in the research we published together. I am grateful for the provision of the dual labelled nanoemulsion that was so instrumental as a biological probe to shed some light on the inflammatory aspects of chronic pain.

I am sincerely thankful to Dr. Benedict Kolber for his support as a valued member of my committee. He held me to a high standard, and I appreciate his expert input into my thesis. I learned a considerable amount from the way he conducts basic science, mentors students and immerses himself in the community aspects of academia.

I am very thankful to Dr. Nicholas Fitz for being a valued member of my PhD committee. He supervised me during my time as a predoctoral research fellow at the University of Pittsburgh and was instrumental in honing my abilities as a scientist and preparing me for undertaking this Ph.D.

I am profoundly thankful to Dr. Kiran Vasudeva for teaching me how to perform rat animal experiments. I am grateful to Dr. Nicole Scheff for teaching me how to perform DRG dissection—at the time a PhD student under the supervision of Dr. Michael Gold at the University of Pittsburgh. I thank Emily Nehl for assisting me in the task of sectioning nerve tissue and refining histology methods. I thank Brooke Deal for assisting me with the sectioning of nerve tissue. I am thankful to Ms. Denise Butler-Buccilli for her wonderful support at the Duquesne University animal care facility, as well as the administrative team at the Department of Biological Sciences, including Pamela Ferchak, Judith Quinque and Terri Widenhofer.

TABLE OF CONTENTS

ABBREVIATIONS

CCI	Chronic constriction injury
COX-2	Cyclooxygenase-2
CXB-NE	Celecoxib nanoemulsion
DF-NE	Drug-free nanoemulsion
DRG	Dorsal root ganglia
MGC	Multinucleated giant cell
NE	Nanoemulsion
NIR	Near-infrared
NIRF	Near-infrared fluorescent
NSAID	Nonsteroidal anti-inflammatory drug
PGE2	Prostaglandin E2
TFRC	Transferrin receptor

LIST OF FIGURES

Chapter I.

Introduction

Chronic pain is a disease epidemic

Adapted from Saleem *et al. Acta Neuropathologica Communications volume 7, Article number: 108 (2019)*

Pain remains the most pervasive reason for medical visits worldwide and affects more people than cancer, heart disease, and diabetes combined [1]. It is a burden to society, as well as the wider economy [2] and afflicts at least 20% of the world's population [3]. Pain is ineffectively managed, largely because the underlying neuropathology is poorly understood, and because it has been mischaracterized by health care systems solely as a symptom of other diseases. When pain transitions from acute to chronic, it becomes a neurobiological disease in its own right [4] as defined by the World Health Organization [5]. Traditionally, efforts to understand the mechanisms underlying chronic pain have centered on neuronal plasticity [6,7]: nociceptor sensitization in the peripheral nervous system [8,9], and sensitization of pain circuits in the central nervous system [10]. In the last two decades, it has been shown that there is a non-neuronal input—largely from the immune system--that contributes to nociceptor sensitization [10]. This includes neuroinflammation, which results from a number of insults, such as injury, neurodegeneration, autoimmunity, and infection [11].

Treatment of chronic pain

Research linking acute and chronic pain to inflammation has its root in the early seventies when Sir John Vane showed for the first time that aspirin worked by inhibiting prostaglandin synthesis [12]. This led to a path of investigation that uncovered the cyclooxygenase-1 (COX-1) and cyclooxygenase-2 (COX-2) enzymes [13,14], and eventually led to the first trials of selective COX-2 inhibitors [15]. Blocking the action of the inducible COX-2 enzyme, which is largely expressed peripherally at sites of inflammation, infection and cancer where it was effective in reducing pain and inflammation [16]. COX-2 drives the production of PGE2, a potent inflammatory mediator capable of sensitizing nerves and causing neuropathic pain.

Analgesics currently used to treat pain include: Acetaminophen, nonsteroidal anti-inflammatory drugs (NSAIDs), cyclooxygenase-2 (COX-2) inhibitors, and opioids. All these drug treatments in their current form are biodistributed systemically, which requires a relatively high dose in order to achieve efficacy at the site of injury. A higher dose subsequently poses a greater risk of tolerance, addiction and adverse side effects. In the case of Acetaminophen, its mechanism of action is not completely understood; although it readily crosses the blood brain barrier and is thought to reduce the active form of cyclooxygenase (COX) enzyme in the brain—independent of direct binding to the active site--, as well as modulating the cannabinoid system [17]. In high doses, it is toxic to the liver, and has been found to be toxic in brain tissue [18]. In terms of long-term toxicity from use to treat chronic pain, there have been reports of kidney disease, bleeding in the digestive tract, heart attack, stroke and high blood pressure [19]. NSAIDs can act in the peripheral nervous system—unlike acetaminophen-- and in high doses, are able to lower inflammation, which is an underlying mechanism contributing to pain. Common anti-

inflammatory drugs such as naproxen and ibuprofen target the enzyme, as well as its isoform, COX-1. These drugs have off-target upper gastrointestinal side effects, including diarrhea, abdominal pain and upset stomach. Selective inhibitors of the COX-2 enzyme such as Vioxx (rofecoxib; Merck) solved this problem in part, however, in the early 2000's, it was found that Vioxx adversely affected the cardiovascular system, causing over 100,000 heart attacks with greater than 30% mortality [20]. Vioxx was subsequently withdrawn from the market. Other COX-2 inhibitors, like Celecoxib, are effective selective inhibitors, however large systemic doses cause adverse side effects by blocking constitutively expressed COX-2 not associated with inflammation, which is indirectly essential for normal homeostatic functioning—as a result of countering infection and initiating wound healing. It is thus important to explore drug therapies that target the drug to the site of injury or inflammation, and that can also dramatically reduce the total body burden of the drug.

Additionally, opioids cannot be mentioned without considering the unprecedented opioid epidemic in the United States. More than 700,000 people in the United States have died from a drug overdose from 1999 to 2017. In 2017 alone, approximately 68% of the 70,200 deaths from drug overdose involved an opioid [21]. Taken together, current pain medication strategies are flawed, and very often dangerous. There is a great need for a dynamic, innovative way to treat pain in the clinic, and current research in the field of pain medicine is offering a hope of filling this demand.

We seek to better understand some of the neuroinflammatory mechanisms underlying neuropathic pain, by utilizing the sciatic nerve chronic constriction injury (CCI) model in rat [22] and introducing a single micro-dose (0.24 mg/kg) of nonsteroidal anti-inflammatory (NSAID) drug (celecoxib) that is packaged in a nanoemulsion (NE) along with near-infrared (NIR)

detection capability [23]. This model results in an inflammatory response to four loosely tied chromic gut ligatures on the right sciatic nerve, causing swelling and subsequent constriction of the nerve. As a result of the CCI procedure, rats exhibit hypersensitive pain behavior approximately eight days following surgery [23–25]. The inflamed nerve is infiltrated by a complex milieu of immune cells, inflammatory mediators [25] and signaling molecules that sensitize it to receive increased nociceptor input, resulting in persistent pain [26]. This inflammatory response is largely driven by the infiltration of macrophages [27,28], which express COX-2, producing PGE2 among other cytokines and chemokines [25].

Advent of pain nanomedicine to personalize treatment and reverse opioid epidemic

It can be considered a high and outstanding goal of medicine to possess the technology to cure a disease by manipulating its pathology on the molecular level, in a precision-targeted manner that is personalized to the individual. Consider Richard Fleischer's 1966 Oscar-award-winning film *Fantastic Voyage*; a 'submarine' crew is shrunk to microbial size in order to be injected into a patient—their goal being to remove a blood clot in the brain. The diagnostic medical utility has similarly been imagined in science fiction, in the case of the medical tricorder in Star Trek—a device that can be scanned over the body and visualize readings from a patient on the nanoscale and diagnose various conditions. Qualcomm, a semiconductor company recently sponsored a $10 million prize to create a device inspired by this science fiction [29], the

efforts of which culminated in a scanner that could diagnose 13 different conditions, and read 5 vital signs simultaneously.

Now very much a disruptive technology, the global nanotechnology market is growing rapidly; estimated at $45 to $50 billion in 2018 by a report from IndustryARC. For example, the use of nanoparticle-based theranostics – a term that describes an agent that is both therapeutic and diagnostic - for application in health and medicine is termed nanomedicine. It is a new frontier that can contribute to tackling the deadliest and most pervasive diseases worldwide. Nanomedicine formulations have the potential for improvements in efficacy and safety by way of improvements in precise targeting to sites of pathology [23,24,30]. The application of nanomedicine has been used in treating cancer--submissions to the U.S. Food and Drug Administration (FDA) for nanomedicines to treat cancer increased by 40% between 2012 and 2017 [31]. Nanoparticle technology was initially explored to tackle the challenge of cancer by targeting the discontinuous nature of blood vessels in tumors [32,33] and culminated in the first FDA-approved nanomedicine in 1995, Doxil® [34].

The size of a nanoparticle ranges from approximately 10 to 200 nanometers, and its design at this scale allows for the opportunity to be targeted to, and interact specifically with cellular components, such as membranes, receptors and nucleic acids--structures that are also nanoscale [35]. This allows for the possibility of nanoparticles traversing biological membrane barriers such as blood vasculature, and the blood brain barrier, as well as endocytosis into immune effector cells such as macrophages [24,36,37]. In addition to advantages in biological interaction rendered by the scale of nanoparticles, incorporating a drug inside of a nanoparticle results in an increase in bioavailability and extended half-life [38]. Another advantage of nanomedicine is a decrease in toxicity—due to vastly less drug being required for efficacy. The

inherent design of a nanomedicine functions to reduce the toxicity of the therapeutic molecule it encapsulates—and the earliest nanomedicines approved by the FDA were based on showing lower toxicity than the traditional drug formulations they were replacing [39].

The bioengineering of nanomedicines has advanced to integrating dynamic functions in addition to the primary therapeutic use, such as incorporating diagnostic contrast agents to track nanoparticles *in vivo* [23,24,40] using optical and MRI imaging [24,41–43]. Termed 'theranostic', combining both therapeutic and diagnostic functions, a nanomedicine with this utility offers the ability to track its biodistribution—and through this, and by measuring disease symptoms in a patient-- tailor a treatment strategy. This begins to realize a personalized medicine paradigm.

Types of nanomedicines

Nanomedicines can be produced from various types of nanomaterials, including perfluorocarbon (PFC) nanoemulsions [36,42–46], liposomes [47], polymeric nanoparticles [48], nanogels [49,50], exosomes [51] and metal-based nanoparticles [52,53] (Fig. 1A). Liposome-based nanoparticles are a versatile delivery platform; for example, they can contain nucleic acids such as siRNAs, as well as traditional pharmacological agents. Polymeric nanoparticles are composed of a polymeric core that is hydrophobic, and have the advantage of a higher capacity to load drugs that are poorly water soluble [54]. Nanogels (or hydrogels) are composed of a three-dimensional lattice of hydrophilic, crosslinked arrays of polymers that can be loaded with drugs [49].

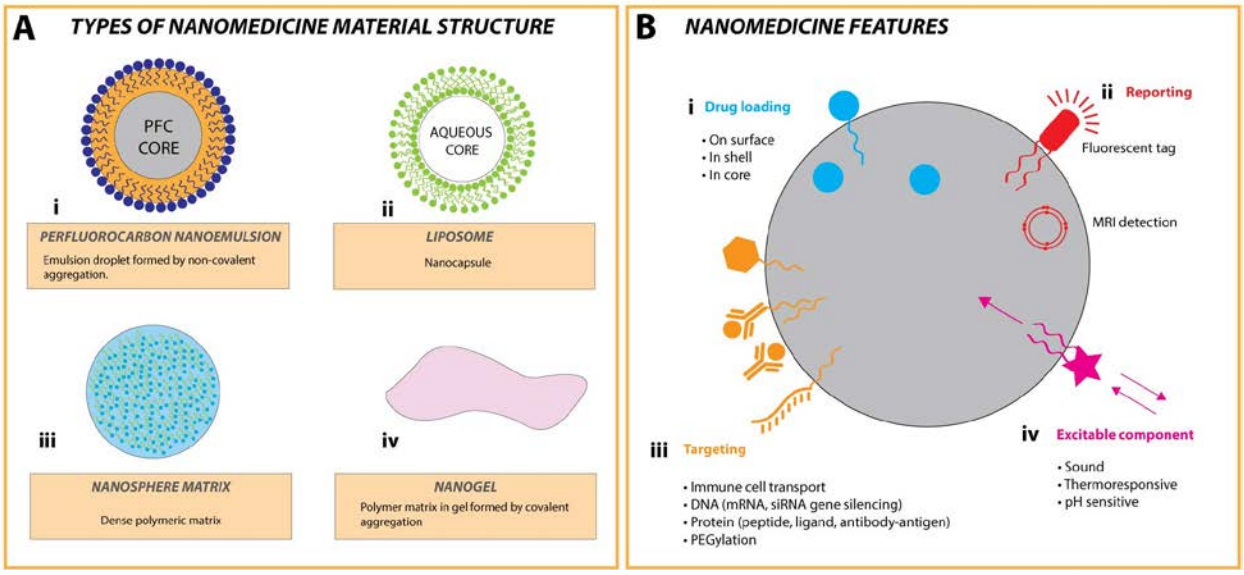

Figure 1. Nanomedicine targeting strategies, types of formulation and the realization of personalized medicine.

Various types of nanomedicine formulations have been produced and they can have a multitude of applications [55]*(**A**), which include but are not limited to, perfluorocarbon nanoemulsions* [36,38,41–46,56,57] *(i), liposomes* [47,58–61] *(ii), a polymeric matrix in the form of nanospheres* [62] *(iii) and nanogels* [49,50,63,64] *(iv). A nanomedicine can be designed to incorporate a variety of different targeting and reporting paradigms (**B**). Drug-loading (i) can be incorporated on the surface, in a shell or at the core of a nanoparticle* [65] *(shown in blue). Reporting functions (ii) can be designed into a nanomedicine, such as a fluorescent component* [42]*, or an atom like* ^{19}F *that can be detected by MRI* [41] *(shown in red). Further functionality can be added by designing reporting elements (such as fluorescence) that can be activated by an excitable component (iv), that is for example sensitive to sound, temperature* [66]*, or pH* [67] *(shown in pink). Nanomedicine can be targeted (iii) to immune cell endocytosis* [68] *and transport to sites of inflammatory pain* [23,24]*. Targeting design can be further enhanced by incorporating an anchored protein* [69] *(such as a peptide, ligand, antibody or antigen) or DNA molecule* [70] *(such as mRNA or siRNA) (shown in yellow). PEGylation is a strategy used to improve the bioavailability of a nanomedicine* [68] *by coating the surface with polyethylene glycol.*

Nanomedicines can also be designed to incorporate a targeting element on the nanoparticle, such as an antibody that can bind to a key protein involved in the disease process, resulting in an indirect reporting of pathological information about the local environment (Fig.

1B). The information is very useful to a clinician, who can monitor and alter the treatment plan accordingly, in a personalized manner [46].

Nanomedicine research for the treatment of pain

Perfluorocarbon nanoemulsions targeted to the COX-2 enzyme in macrophages have been developed by Janjic and colleagues [36,37,57,71,72,38,41–46,56]. In a rat model of neuropathic pain, these nanoemulsions target infiltrating macrophages to nerve injury, and are shown to be effective in reversing pain-like behavior and macrophage-related inflammation [23,44,57].

Nanoparticles based on lipids—such as liposomes and solid lipid nanoparticles (SLNs)—are another class of nanomedicine that have been in development for over two decades [60]. Researchers recently conjugated Leu-enkephalin (LENK)—an endogenous neuropeptide that is usually rapidly metabolized to the lipid squalene (SQ) to create nanoparticles that showed pain relief in a rat model of inflammation [73]. The drug-release profile of LENK-SQ nanoparticles could be engineered into the design by using different chemical linkers. The anti-hyperalgesic effects outlasted morphine treatment, and the nanoparticles were able to bypass the blood-brain barrier. The ability to modulate the rate of drug release is an advance that could allow a nanomedicine to be engineered so that subsequent dosing could have varying release profiles based on the underlying pain pathology—a significant advance in personalized medicine.

Clinical studies involving cannabis and synthetic cannabinoids as a way to manage chronic pain have been gaining traction [74]. Researchers investigated the utility of nanoparticles

composed of poly(lactic-co-glycolic acid) (PLGA)—a copolymer--loaded with a cannabinoid derivate, and found that neuropathic pain was alleviated for eleven days after a single oral dose of a nanoparticle formulation optimized with a polyethylene glycol (PEG) coating [75].

In another study investigating the efficacy of a polymeric nanomedicine, researchers loaded nanoparticles with curcumin and observed significantly reduced pain-like behavior resulting from diabetic neuropathic pain via the attenuation of the DRG expressed P2Y12 receptor [76]. Curcumin, while possessing anti-inflammatory and antioxidant properties, exhibits low bioavailability and stability in its free form [76]. This study demonstrates an improvement in efficacy by encapsulating the compound in a nanoparticle.

Nanoparticles formulated into a hydrogel matrix offer the advantage of improving viscosity and making nanomedicine application more feasible for topical application. This presents a particularly useful application in the case of post-operative pain, or muscle pain. In one study, a hydrogel containing Hyptis pectinata (Lamiaceae) Leaf Essential Oil was formulated to be thermoreversible—and lowered pain-related behavior in an acid saline-induced chronic muscle pain model [64]. Another study utilizing hydrogel-based nanomedicine found that this method of delivery prevented the precipitation of the bioactive compound—nobiletin—which is hydrophobic. Delivering the hydrophobic drug to the bladder by a cationic nanoparticle and thermo-sensitive hydrogel composite system resulted in preserving the stability of nobiletin in the GI tract, resulting in a sustained release and absorption[54]. A method such as this could conceivably be applied to a pain medicine delivered orally, resulting in an improvement in bioavailability and efficacy.

The realization of personalized pain nanomedicine

The heterogeneity of pain is further compounded by sex-differences in both peripheral and central molecular cell biological mechanisms as well as underlying aspects of pain perception [77,78] that equates to a need for a personalized approach to treatment. Current nanomedicine design is factoring in approaches that meet this need, the most prominent of which is the advent of theranostic nanomedicine [36,37,57,72,38,41–46,56]. Conceptualized by Dr. Jelena Janjic, a personalized medicine approach has been applied for the first time to pain therapy [46]. This promises to track the underlying pathology of pain for each individual patient, and determine if treatments need to be modified. The utility of machine learning could also be used to compute patient data and use it to screen not only existing pain nanomedicines on the market, but suggest ways in which to modify them to offer the most effective treatment. The advances in personalized pain nanomedicine have the advantage of limiting drug toxicity further, by administering treatment only for as long as it is required—as reported by the nanomedicine [23,46]. In another example of the utility of nanomedicine as personalized medicine, the bodies endogenous extracellular vesicles are used to transport drug—a technology that has been demonstrated recently to treat liver disease [51]. The limiting of toxicity and the ability to target the PNS pathology of pain places nanomedicine treatment as a potential resource distinct from CNS targeted drugs such as opioids. By attenuating or eradicating the source of the pain with a targeted, low-dose strategy, there is not a need to rely on high doses of drugs that target pain processing centrally [46].

Personalized nanomedicine represents a desperately needed advance to effectively manage severe chronic pain disorders such as fibromyalgia, neuropathic pain and migraine, and

begin to reverse the opioid epidemic. Further pain nanomedicine research, as well as translating advances in terms of precision drug targeting from the oncology field, will be required to improve the treatment of acute and chronic pain and realize a truly personalized approach. Considerations of toxicity, environmental impact and manufacturing potential will also need to be addressed in order to fast-track pain nanomedicines onto the market.

Macrophage and mast cell mechanisms of neuropathic pain

Reprinted with modification from Saleem et al. Acta Neuropathologica Communications (2019). ***volume 7, Article number: 108 (2019)***

We sought to further our understanding of the immune-cell pathology underlying neuropathic pain by utilizing the chronic constriction injury (CCI) rat model [22]. In this model, an inflammatory response is produced by loosely tied chromic gut ligatures on the right sciatic nerve, causing swelling and subsequent constriction of the nerve. The inflamed nerve is infiltrated by a complex milieu of immune cells, inflammatory mediators [25] and signaling molecules, resulting in nociceptor sensitization, and causing persistent pain [26]. This inflammatory response is largely driven by the infiltration of macrophages [27,28], which express the cyclooxygenase-2 (COX-2) enzyme. COX-2 synthesizes PGE2, and in addition, the macrophage releases various other cytokines and chemokines [25]. Rats exhibit progressive hypersensitive pain-like behavior reaching a maximum approximately eight days following surgery [23–25].

In earlier studies, Janjic and colleagues have designed and developed theranostic nanoemulsions that exhibit a preferential targeting of circulating monocytes via phagocytosis [36–38,42–46,57,72], and subsequent natural migration and accumulation at sites of inflammation [57], including injured nerve [23]. In this paradigm, we are also able to image the extent of neuroinflammation by detecting a near-infrared fluorescent (NIRF) signal from the nanoemulsion-contained DiR fluorescent dye that accumulates at the site of injury in live animals [23,24]. We have previously described the formulation of drug loaded perfluorocarbon nanoemulsions [23,44]. The rationale described previously by Janjic and colleagues [23,44,57] for drug-loading nanoemulsion droplets with celecoxib is to directly attenuate the COX-2 enzyme, which synthesizes PGE2, a potent proinflammatory mediator. PGE2 perpetuates the neuroinflammation that sensitizes nociceptors, leading to neuropathic pain. Celecoxib directly binds to the active site on the COX-2 enzyme, thereby blocking the synthesis of PGE2 [79]. We have previously shown that nanomedicine treatment reverses pain-like behavior and reduces inflammation in a neuropathic pain model in rats [23] and in an inflammation model in mice [57].

We designed an experiment with the aim of exploring key aspects of macrophage and mast cell neuropathology whilst pivoting at key events on a timeline of neuropathic pain: a state where the animal exhibits pain-like behavior, a state where the animal experiences peak pain-relief (day 12 post-surgery)—as a result of nanomedicine treatment [23]—and a state when the animal returns to pain-like behavior (day 18 post-surgery). Testing groups of CCI rats are intravenously administered with nanomedicine or vehicle treatment (nanoemulsion without celecoxib) 8-days post-surgery—due to animals showing peak pain-like behavior at this time point. A control group of animals undergoes a sham CCI surgery. Key in the design of the nanomedicine is the capability of visualizing macrophages [36,37,42,43,45,57,71] that have phagocytosed

the nanoemulsion (~ 140 nm per droplet). In this way, the theranostic nanomedicine—that is both 'therapeutic' and 'diagnostic'—serves as a biological probe to both influence and/or label aspects of the underlying neuropathology.

Pivoting on the behavioral states of *pain*, *pain relief*, and *return to pain* as compared to control animals, we first present the extent of inflammation measured by NIRF imaging of the live animal and then report on our findings from histological analysis of sciatic nerve and its associated L4 and L5 DRG. Using confocal microscopy, the quantity of infiltrating macrophages is measured—marked by anti-CD68 antibody, a pan-macrophage marker [80]—in the injured sciatic nerve and associated L4 and L5 DRG neurons.

Along with macrophages, resident mast cells constitute another major cell group involved in the inflammatory response. They are found close to nociceptive neuron cell bodies [81]—as well as in a progenitor form in the blood circulation—and are associated with a number of clinical pain disorders [82]. With respect to the inflammatory component of neuropathic pain, mast cells provide an input to cause neurogenic inflammation, which propagates along afferent nociceptors via the release of substance P [82]. Mast cells are filled almost entirely with secretory granules and contain a vast assortment of inflammatory mediators and other bioactive molecules such as cytokines, lysosomal hydrolases and proteases [83]. In this study, mast cell count and extent of degranulation in the sciatic nerve and associated DRG is investigated by labeling with an antibody targeted to mast cell protease 1 (Mcpt-1). Mcpt1 constitutes a major component of the secretory granules released by mast cells during an inflammatory response and is specific to this cell type. The cellular expression of Mcpt1 labels mast cells, and when expressed extracellularly, indicates that a mast cell has been activated and degranulation has occurred. We present data

reporting on the numbers of mast cells, and the extent of their degranulation, at the sciatic nerve—and the associated DRG—following nanomedicine treatment.

The treatment effect observed at the sciatic nerve was probed further by investigating individual macrophages to reveal details of their inflammatory phenotype, in addition to whether they are positive for nanomedicine NIRF signal. We also report on the expression of COX-2 in macrophages and their release of PGE2 in the milieu of the injured sciatic nerve tissue. Macrophages play a dual role in damaged tissues—a subset performs inflammatory functions and are termed M1 pro-inflammatory macrophages, while those that are anti-inflammatory effectors, promoting tissue repair, are termed M2 macrophages [84,85]. A recent membrane proteome study [86] was able to discriminate M1 (pro-inflammatory) and M2 (anti-inflammatory) macrophages with high precision by their expression of the costimulatory protein, Cluster of Differentiation 40 (CD40), and transferrin receptor (TFRC) respectively. These markers were thus used to investigate the percentage of M1 and M2 macrophages in the injured sciatic nerve. Our present paper [87] details the relative macrophage polarity in the context of treatment, and pain-like behavior. We also report on the presence of CD68-positive multinucleated giant cells (MGCs) in the injured nerve—cells formed from the fusion of their M2 polarized macrophage precursors. MGCs have been reported to enhance the removal of debris from tissues [88], aiding tissue regeneration.

This thesis and published paper [87] proposes a mechanism for nanomedicine-driven pain relief in a rat model of neuropathic pain. We present the interplay of COX-2 attenuation, PGE2 production and the resulting effect on macrophage polarity. In addition, macrophage infiltration to the injured nerve is investigated, as well as the formation of multinucleated giant cells, which contribute to tissue regeneration and repair. The numbers of mast cells localized in the injured

nerve and DRG and the extent of their degranulation is investigated. Based on patterns of macrophage infiltration, changes in their phenotype, and levels of mast cell degranulation, we suggest a mechanism that could underscore the return to pain-like behavior when the treatment effect has subsided. Taken together, this observation provides key insights into the neuropathology underlying neuropathic pain, by utilizing a nanomedicine as a biological probe. Having the ability to track patterns of macrophage infiltration both during and after long-lasting pain relief, we demonstrate a novel research paradigm that could be useful in more precisely elucidating the neuropathology underlying diseases with an immune component.

Chapter II.

Materials and methods

Adapted from Saleem *et al. Acta Neuropathologica Communications volume 7, Article number: 108 (2019) and Janjic et al. Journal of Neuroimmunology. Volume 318, Pages 72-79. (2018.*

Ethics approval and consent to participate

This study was carried out in accordance with the recommendations in the Guide for the Care and Use of Laboratory Animals of the National Institutes of Health. The Institutional Animal Care and Use Committee (IACUC) at Duquesne University approved the protocol (# 1501-01 for Janjic et al publication [23] and # 1109-10 for Saleem et al publication [87]). Male Sprague-Dawley rats weighing approximately 220 g were used in this study (Hilltop Lab Animals, Inc., Scottdale, PA). Rats were maintained on a 12:12 hour light-dark cycle and were given unrestricted access to purified chow (D10012G, Research Diets, Inc., New Brunswick, NJ) and water. All efforts were made to minimize animal suffering and to reduce the number of animals used.

Blinded experiments

Aspects of these studies were carried out under “blinded condition”. For example, the NIR fluorescence image analysis was performed by an analyzer who was blinded to the CCI, sham or naive conditions. Similarly, the histological data was collected in a blind fashion as well. The tissue samples collected during dissection were coded and the confocal microscopy and image analysis were performed as per the codes which were later matched with any given rat condition.

DF-NE and CXB-NE treatment conditions were blinded from the investigator. During behavioral data collection, it was not possible to stay blind to the surgical condition, because the signs of a CCI surgery were very robust and the rat conditions were easily discernible from the sham or naive rats.

Chronic constriction injury

The CCI [22] animal model was used to induce neuropathic pain in rats as previously described [23]. Briefly, animals were divided into three groups; CCI rats administered with nanomedicine containing no drug (DF-NE), CCI rats administered with nanomedicine containing drug (CXB-NE) and sham surgery rats. Under isoflurane anesthesia, the surgical site was sterilized with ethanol and iodine, the skin was incised and the biceps femoris muscles separated to expose the sciatic nerve. Chromic gut suture was used to tie four ligatures approximately 1

mm apart around the common sciatic nerve. Care was taken to ensure the ligatures were neither tight nor loose. The biceps femoris muscles were closed using chromic gut suture followed by skin closure using stainless steel wound clips. An identical surgery was performed on animals in the sham CCI group, without ligatures being tied to the sciatic nerve.

Pain-like behavior testing

To assess mechanical allodynia - indicative of pain-like hypersensitivity - von Frey filaments were applied to the plantar surface of the hind-paw. These are hand-held instruments with an attached filament that is elastic, and will bend at a specific force, determined by the thickness of this filament. The threshold force at which rats withdrew their paws 50% of the time was determined using the up-down method [89]. Testing was performed at the same time of day during their light cycle. Rats were acclimated for 15 minutes in the testing apparatus: Perspex chambers with a wire mesh floor that allows access to the paws. Baseline testing was carried out for two consecutive days before surgery. The rats were rested for one day following surgery, after which behavioral testing resumed a day later, and on consecutive days, ceasing on the day 12 or day 18 following surgery (summarized in Fig. 4A). The 50% paw withdrawal threshold was calculated, and treatment groups were analyzed by two-way ANOVA with Tukey's post hoc test for multiple comparisons of group means. The confidence interval was 95% and data were presented as mean ± SD. The statistical software used was GraphPad Prism 6.

In vitro cell culture studies – cellular uptake

Concentration dependent uptake of nanoemulsions was determined in macrophages as reported previously using NIRF imaging [44] by the laboratory of Dr. Jelena Janjic.

In vitro cell culture studies – cellular viability

The effect of nanoemulsions on the viability of RAW 264.7 macrophages was evaluated after a 24 h incubation at 37 °C with different concentrations of nanoemulsion dispersed in whole media. This was performed by the laboratory of Dr. Jelena Janjic. Control cells were not exposed to any treatments. Cells were plated at 5000 cells/100 μL/well in 96 well plates and incubated overnight for adhesion, followed by 24 h incubation with treatments. After incubation, cell media was replaced by fresh warm full cell culture media 100 μL. CellTiter-Glo® analyte was added (40 μL/well) to induce cell lysis by shaking in the dark for 20 min at RT. The obtained cell lysates (90 μL) were transferred to a white opaque plate and luminescence recorded on microplate reader Victor 2 (Perkin Elmer, Waltham, MA).

PGE2 ELISA Assay

The pharmacological effect of the nanoemulsion in vitro (RAW 264.7) was evaluated after a 24 h incubation at 37 °C with different concentrations of nanoemulsion dispersed in cell culture media. This was performed by the laboratory of Dr. Jelena Janjic. Cells were plated at 300,000 cells/2 mL/well in 6-well plates and incubated overnight for adhesion, followed by 24 h incubation with nanoemulsion treatments. After treatment, the nanoemulsion media was replaced with LPS treated (0.5 μg/mL) and LPS free media for 3 h. This final media was recovered for the PGE2 ELISA assay.

Rat Tail-Vein Injection of Nanoemulsion

Adapted from: A new Best Practice for Validating Tail Vein Injections in Rat with Near-infrared labeled Agents

Muzamil Saleem*, Andrea M Stevens*, Lu Liu, Jelena Janjic, John A Pollock

*Co-first authors

Reprinted from Saleem, M., Stevens, A. M., Deal, B., Liu, L., Janjic, J., Pollock, J. A. A New Best Practice for Validating Tail Vein Injections in Rat with Near-infrared-Labeled Agents. *J. Vis. Exp.* (146), e59295, doi:10.3791/59295 (2019).

Contribution statement

- M.S. performed all experiments, produced figures and wrote the manuscript under the guidance of J.A.P.
- J.A.P, A.S, L.L and J.M.J contributed to editing the manuscript.
- Animal care, surgery, tail vein injections, and NIRF imaging were carried out jointly by M.S. and A.S. under the guidance of J.A.P.
- B.D. performed tail vein injection during the filming of this video protocol
- NIRF image quantification and statistical analysis was performed by M.S. under the guidance of J.A.P.
- J.M.J. produced the nanoemulsion and designed the overall approach for targeting the COX-2 enzyme in macrophages in the context of neuropathic pain. The nanoemulsion was further fabricated by L.L. and S.P. under the guidance of J.M.J.
- Stability of nanoemulsion was assessed by J.M.J, L.L. and S.P.

The nanomedicine--celecoxib-loaded (CXB-NE) and drug-free (DF-NE)—was injected intravenously via the lateral tail vein of rats on day-8 post-surgery (Fig. 3A) as previously described [23,90]. Injection of 300 µL of CXB-NE or DF-NE was performed with an intravenous catheter with a blood-flow indicator (Terumo, Tokyo, Japan). The single dose of celecoxib in the CXB-NE group was ~0.24 mg/kg. The successful injection was confirmed by both the blood indicator on the catheter as well as using a pre and post-injection NIRF image to make a quality assessment [90].

In our recent published paper [90] and demonstration video (https://www.jove.com/video/59295/a-new-best-practice-for-validating-tail-vein-injections-rat-

with-near) we presented a method to validate tail vein injections in rats by utilizing near-infrared fluorescence imaging data from dyes incorporated into agents or biological probes. The tail is imaged before and after the injection, the fluorescent signal is quantified, and an assessment of the injection quality is made.

The motivation for the development of this procedure is that intravenous (IV) administration of agents into the tail vein of rats can be both difficult and inconsistent. Optimizing tail vein injections is a key part of many experimental procedures where reagents need to be introduced directly into the bloodstream. Unwittingly, the injection can be subcutaneous, possibly altering the scientific outcomes. Utilizing a nanoemulsion-based biological probe with an incorporated near-infrared fluorescent (NIRF) dye, this method offers the capability of imaging a successful tail vein injection *in vivo.* With the use of a NIRF imager, images are taken before and after the injection of the agent. An acceptable IV injection is then qualitatively or quantitatively determined based on the intensity of the NIRF signal at the site of injection.

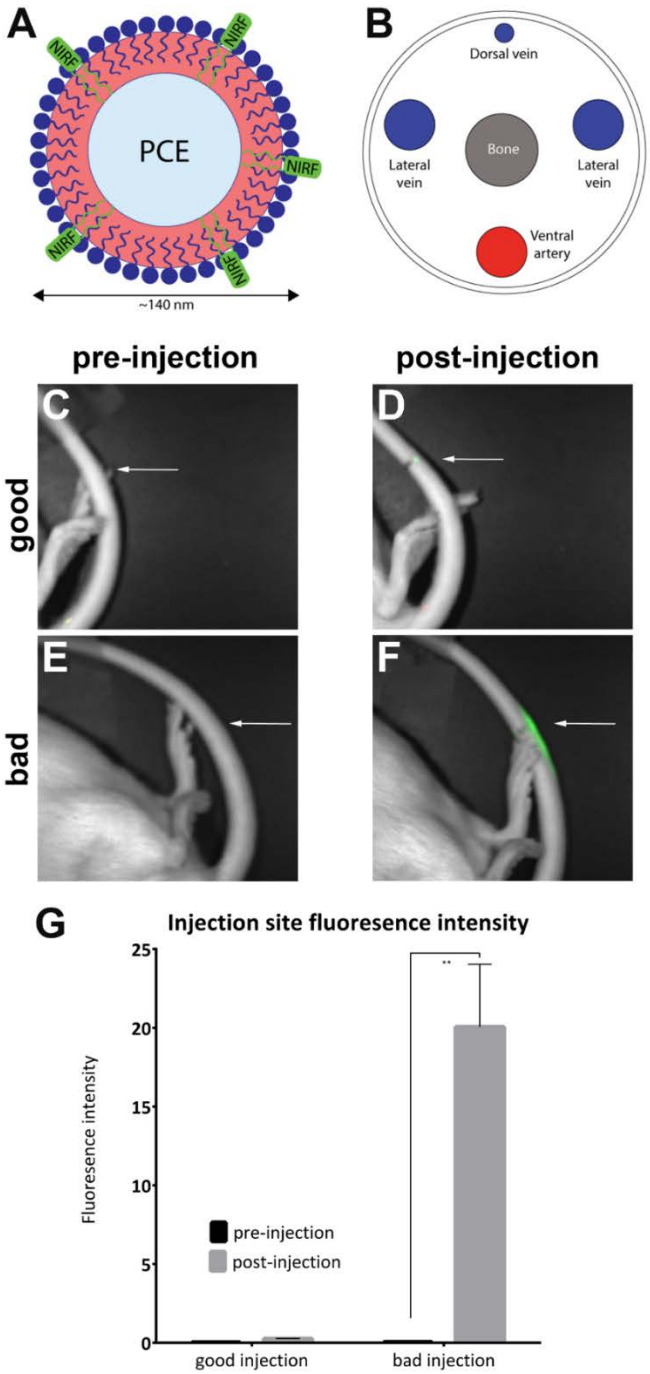

Figure 2. NIRF based nanoemulsion and images of tail vein.

A nanoemulsion-based biological probe containing NIRF dye was injected into (B) the lateral tail vein and imaged in a NIRF imager. (C and D) Pre- and post-injection images of a good injection. (E and F) Pre- and post-injection images of a bad injection. White arrows indicate the point of injection. It is possible to qualitatively assess the success of a good injection compared to a bad injection by assessing the extent of the NIRF signal at the site of injection. Unacceptable injections display fluorescence throughout the length of the tail and were removed from the

analysis (Figure 2). (G) The images can also be analyzed to reveal a quantitative measure of fluorescence intensity, with thresholds for injection quality assigned by the investigator. The error bars on the graph reflect the SEM. For the 'good injection' group, n = 7. For the 'bad injection' group, n = 4. There is a statistical difference in fluorescence intensity in the 'bad injection' group when comparing pre- and post-injection images (unpaired t-test; p = 0.0024). This figure is reproduced from Saleem et al. J. Vis. Exp. (146), e59295, doi:10.3791/59295 (2019). Muzamil Saleem performed related experiments and produced the figure.

In this method, a NIRF dye containing a biological probe—in this case, a nanoemulsion (Fig. 2A) [37,44,45,57]—is injected into the lateral tail vein of rats. This particular NIRF-containing nanoemulsion has been used previously to image and track neuroinflammation in vivo and ex vivo [42,43] in a rat model [22] of neuropathic pain [23–25,37,44,57]. Imaging is conducted before and after the injection with a preclinical NIR fluorescence imager. This serves as a tool to validate the quality of the agent administration. Imaging prior to the tail vein injection serves as a basis for obtaining a baseline image.

Typically, a heat lamp or warm water is used to warm the tail, which causes dilation of the vein, permitting its visualization prior to injection. While this ensures easier entry into the vein, there is not a quantitative way to discern whether the compound has entered the bloodstream in its entirety [91–94]. This becomes more difficult still in strains of animals where the vein contrasts faintly with the skin, such as in black mice. Typically, the investigator can gauge a failed injection by experiencing resistance during the injection and, in some cases, visualizing a bulge on the tail, indicating a subcutaneous leakage of the agent [95,96].

Simultaneous image acquisition of white light and 800 nm fluorescence is captured using the NIRF imager and associated software. The relative fluorescence intensity is measured on the tail at the pre-injection and post-injection states. The fluorescence intensity for the region of interest (ROI) at the site of injection is recorded and divided by the area of the ROI. Qualitative assessments can be made on which injections are acceptable. Optionally, further quantitative

analysis can be performed by setting thresholds for acceptable injections and assigning ROI measurements into groups, at which point statistical significance can be calculated.

By utilizing this validation strategy following tail vein injections, the standard of a research study improves due to increased consistency of agent administration.

Animal Protocol

All protocols were performed in accordance with the guidelines in the Guide for the Care and Use of Laboratory Animals of the National Institutes of Health and Institutional Animal Care and Use Committee (IACUC) at Duquesne University protocol #1501-01 and #1803-02.

Preparation and anesthesia

NOTE: Aseptic techniques were used for the entirety of the procedure. Only new sterile materials and autoclaved sterile instruments were used. Personal protective equipment (sterile gloves, hair bonnet, surgical mask, scrubs) was worn to avoid contamination.

We used adult male Sprague-Dawley rats weighing 250–300 g. Rats were acclimated to standard living conditions, a 12 h light/12 h dark cycle, and provide food and water ad libitum. Animals were socially housed, on paper bedding, and provide a controlled diet (D10012G Research Diets, Inc. New Brunswick, NJ to avoid autofluorescence during imaging.

With the use of a properly placed heating pad, we anesthetized the animal under an initial 5% isoflurane in 20% oxygen, followed by a maintenance level of not less than 1.5% isoflurane and not more than 3%, unless the animal wakes up or retains feeling.

We confirmed proper anesthesia via a lack of response to tail pinches. Monitor the blood flow as well via vital signs throughout the procedure.

Pre-injection imaging

We imaged the animal in a preclinical NIR fluorescence imager by positioning the animal laterally to expose the injection site on the lateral tail to establish a baseline of fluorescence in the tail (Fig. 2C, E).

Following imaging, animals were moved back to the surgical table, and placed under anesthesia for the tail vein injection.

NOTE: Rat's vital signs were continually monitored, and proper anesthetization rechecked via tail pinch.

Method of Tail vein injection

With the animal in the prone position, orient the tail with the dorsal side facing up. Dilate the tail vasculature in warm water for a minimum of 1 min. Orient the tail vein so the lateral side (either right or left) is turned 30° (clockwise or counterclockwise) to expose the right or left tail vein (Fig. 2B).

Once a lateral tail vein has been located (which appears dark-colored upon dilation), sterilize the entire tail with alcohol pads, repeating 2x.

At an appropriate dosage based on the study design, begin injections in the distal coccygeal vertebrae region of the tail and moving more proximal if proper needle placement fails.

Insert a 25–27 G sterile needle, bevel up, into the lateral tail vein, with the tail at a 180° angle, inserting the needle parallel to the lifted tail. Observe blood flashback in the rim of the needle to ensure correct placement. If no flashback is apparent, slowly move the needle tip (without removing it from the tail) to find vein insertion. If placed subcutaneously, no blood flashback will occur.

Insert the syringe with the injectable materials into the rim of the needle. When proper placement is achieved, the injectable fluid will not incur resistance upon injection. The injection will advance smoothly and easily. Once injected, remove the needle and the syringe, apply pressure with sterile gauze for at least 1 min to ensure clotting, and mark the spot of injection with a pen on the tail, ensuring it is visible on the white light image. NOTE: No hematoma or lesion will be visible at the site of injection.

If the needle tip moves during the syringe insertion, remove the needle and retry the needle entry procedure more proximal on the ipsilateral tail vein. Do not reuse the same needle if a different reentry point is tried. NOTE: Alternatively, the injection can be performed with an IV catheter (SURFLO IV Catheter, 24 gauge, by TERUMO). This has the benefit of visual confirmation of the catheter during venipuncture. Insert the catheter, bevel side up, at the angle previously described. Observe prompt flashback in the entire length of the needle and the catheter to ensure correct placement. Slight back pressure can be used to pull blood into the syringe to confirm proper placement in the vessel before injecting. Again, no resistance will be felt.

Post-injection imaging

Perform quality assessment after the tail vein injection in a preclinical NIR fluorescence imager in the same orientation as the pre-injection image. Increase the isoflurane anesthesia to 3% for several minutes and move the animal to the imager. Ensure the animal is still properly anesthetized.

Quickly, orient the animal on its lateral side to expose the injection site (as marked) on the lateral tail. Check to see if a NIRF signal is present only at the site of injection as this is the most optimal injection, indicating a successful tail vein injection (Fig. 2D).

NOTE: If the signal is sparse but still within the proximal vicinity of the tail vein injection, the injection is acceptable and can be considered as a successful tail vein injection. If the signal is dispersed throughout the entire tail, it is considered to be subcutaneous and, thus, unsuccessful (Fig. 2F). Fig. 3 shows additional examples of failed injections.

Image quantification

Image quantification can be performed in the imaging software that accompanies the NIR imager, as this is a function of the software. Alternatively, other commercially available imaging software may be used [97]. In the post-injection image, draw an ROI around the area of fluorescence at the injection site and clone it in all animals in order to compare [23,45]. Perform a simultaneous image acquisition of white light (body view) and 785 nm excitation for 820 nm emission using the NIRF imager and associated software, with linked lookup tables (LUT).

Perform a one-way analysis of variance (ANOVA) as a statistical analysis for the entire set of conditions revealing a treatment effect with a statistically significant *p*-value of 0.0024.

Measure the area and relative fluorescence intensity and record the measurement of the area/intensity.

NOTE: The researcher can decide on thresholds that discriminate good from bad injections or assign a percentage of quality to the injection.

Results

Rats were injected with NIRF-containing nanoemulsion into the lateral tail vein, and pre- and post-injection images were taken with the small-animal imager (Pearl Trilogy by Li_COR Biosciences) as described in the protocol. Post-injection images are qualitatively assessed for injection quality and placed into 'good injection' ($n = 7$) and 'bad injection' ($n = 4$) groups. Qualitative assessment was carried out by observing the post-injection area fluorescence intensity. In an optimal injection, the NIRF signal is confined to the site of injection. No signal will be seen if the injection is successful because the agent has been fully displaced into the bloodstream. A bad-quality injection displays a NIRF signal that is dispersed along the length of the tail.

Images were analyzed with the accompanying NIRF imager software. ROIs were drawn at the site of pre-injection images (Fig. 2C, E) and around the area of fluorescence in post-injection images (Fig. 2D, F). Images where fluorescence was visible throughout the length of the tail were deemed unacceptable and removed from the analysis (Fig. 3A, B, C). Measurements of the area and fluorescence intensity were recorded. Values for area/fluorescence intensity were

calculated and plotted (Fig. 2G). A significant difference in fluorescence intensity between pre- and post-injection images was observed in the 'bad injection' group (Fig. 2G) (p = 0.0024).

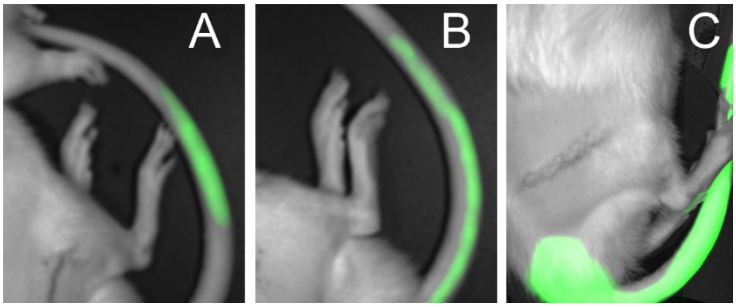

Figure 3. Examples of bad injections.

Fluorescent signal seen in part of the tail. (B) Fluorescent signal seen over the full length of the tail. (C) Fluorescent signal dispersed heavily in the entire tail and caudal area of the animal's body. This figure is reproduced from Saleem et al. J. Vis. Exp. (146), e59295, doi:10.3791/59295 (2019). Muzamil Saleem performed related experiments and produced the figure.

NIRF Imaging in Live Animals

The right and left thigh of anesthetized rats were imaged with a preclinical fluorescence imager (LiCOR® Pearl Impulse from LI-COR Biosciences, Lincoln, NE) on day-11 and day-17 post-surgery, in day 12 and day 18 testing groups respectively. The NIR dye in the nanomedicine that has accumulated in labeled monocytes/ tissue macrophages fluoresces in the scanner. Images in the fluorescent channel (785 nm excitation for 820 nm emission) and a white light channel (to capture an image of the body of the rat) are acquired and merged in the LiCOR Pearl Impulse Software (version 2.0) with linked look-up-tables (LUT) [24]. In order to avoid non-specific

fluorescence in the abdominal and thoracic region, animals were given a controlled research diet throughout the procedure (D10012G Research Diets, Inc. New Brunswick, NJ). NIRF images were analyzed using Image Studio Lite Software (LI-COR Biosciences, Lincoln, NE) as previously described [23,24]. Briefly, a region of interest (ROI) was selected over the sciatic nerve. Relative fluorescence of ROI was calculated by dividing the total fluorescence in the ROI by the area. Relative fluorescence of the testing groups is analyzed by one-way ANOVA, with a Tukey's post hoc test to test multiple comparisons of group means. The confidence interval is set at 95%. Data are presented as mean ± SEM. The statistical software used is GraphPad Prism 6.

Euthanasia

Rats were euthanized under anesthesia with a 2 ml intraperitoneal injection of Euthasol (pentobarbital sodium and phenytoin sodium solution, Virbac AH, Inc., Fort Worth, TX). The animals were immediately perfused with 180 mL of cold 1X PBS followed by 180 mL of 4% paraformaldehyde 1X PBS solution, administered into the left ventricle of the heart, resulting in whole body fixation.

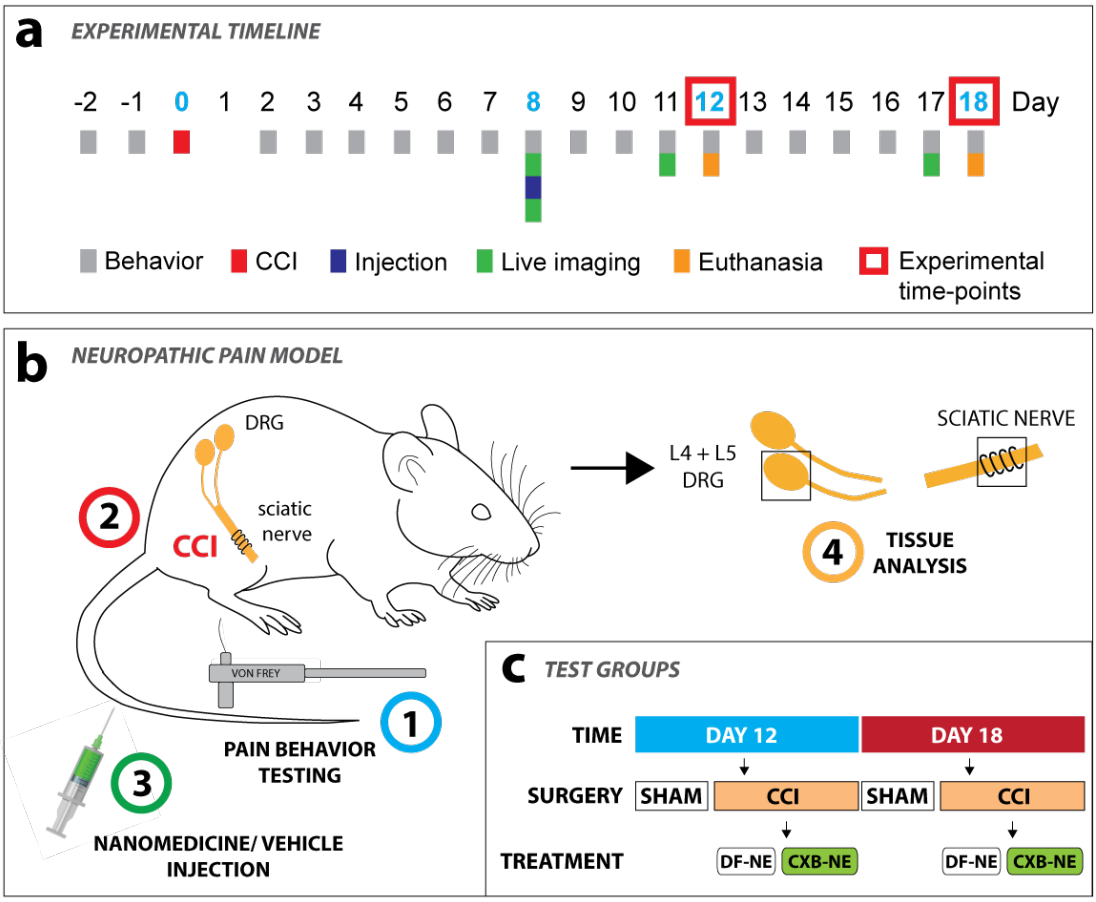

Figure 4. Summary of the experimental timeline, neuropathic pain model and testing groups.

*Summary of the experimental timeline, neuropathic pain model and testing groups. (**a**) A daily timeline indicates the procedures that a rat undergoes for both the 12-day test group and the 18-day test group. Mechanical stimulus-evoked pain-like hypersensitivity testing (**b1**), surgery (**b2**), tail vein injection of treatment (**b3**), live-animal NIRF imaging, and recovery of tissue for analysis (**b4**). Sciatic nerve and DRG (RL4 and RL5) tissue is collected from the animal following euthanasia and perfusion-fixation on day 12 and day 18 (**a**, **b4**). Test groups are split into time-points of day 12 and day 18, each with groups of CCI and sham surgery rats (**c**). The surgery groups are further divided into rats that are treated with drug-free nanomedicine (DF-NE) and those treated with celecoxib nanomedicine (CXB-NE) (**C**). This figure is reproduced from Saleem et al. Acta Neuropathologica Communications. Volume 7,*
Article number: 108 (2019). Muzamil Saleem performed related experiments and produced the figure.

Tissue Processing

Sciatic nerve--and separately, L4 and L5 DRG--was dissected on day 12 or day 18 post-surgery. Tissue was post-fixed in 4% PFA (pH 7.4) in 1X PBS for 24 hours at 4 °C and then transferred to 30% sucrose in 1X PBS and stored at 4 °C until further processing. Tissue was prepared for sectioning by transferring to OCT solution (Sakura, Torrance, CA) and frozen in a bath of isopentane maintained at a temperature of ~-55 to -60 °C surrounded by dry ice. Frozen tissue was sectioned at a thickness of 20 µm and mounted on gelatin-coated slides (SouthernBiotech, Birmingham, AL). The slides were stored at -20 °C until further processing.

Immunofluorescence and Nanoemulsion Detection

Protocol used in Saleem *et al. Acta Neuropathologica Communications volume 7, Article number: 108 (2019)*

Slides were processed using the primary antibodies listed in Supplementary Table 1 at the stated dilutions from manufacturer stock solutions. Double-staining was performed with two primary antibodies in each experiment. Appropriate secondary antibodies raised in different hosts were selected to target the host of the primary antibody in order to prevent nonspecific binding. Sections stored at -20 °C were warmed on a slide warmer at 37 °C for 30 minutes. Sections were post-fixed in 4% paraformaldehyde in 1X PBS solution for 15 minutes and permeabilized for 10 minutes in 0.3% Triton X-100 detergent in 1X PBS. Tissue blocking of

nonspecific staining was performed by incubating with BlockAid™ Blocking Solution (B10710, Thermo Fisher Scientific) for 1 hour at room temperature. This solution was also used to prepare all working antibody solutions. The sections were incubated overnight at 4 °C with primary antibody prepared at the appropriate working dilution (Supplementary Table 1). The following day, sections were washed in 0.3% Triton X-100 detergent in 1X PBS and incubated in secondary antibody solution for 2 hours at room temperature. Following washing in 0.3% Triton X-100 detergent in 1X PBS, sections were mounted using Prolong Diamond antifade reagent with DAPI (P36965, Thermo Fisher Scientific). The nanomedicine contains DiR so that a 'double-stain' experiment actually has four dyes in the tissue; DAPI (nuclei), two secondary-antibody conjugated fluorophores (Supplementary Table 2), and DiR (nanomedicine).

Antibody	Source	Type	Manufacturer	Cat #	Dilution	Target
anti-CD68	Mouse anti-Rat	Monoclonal	BIO-RAD	MCA341R	1/100	Monocyte/ macrophage marker
anti-CD68	Rabbit anti-Rat	Polyclonal	abcam	ab125212	1/100	Monocyte/ macrophage marker
anti-COX2	Rabbit anti-Rat	Polyclonal	abcam	ab15191	1/100	COX-2 enzyme
anti-PGE2	Rabbit anti-Rat	Polyclonal	Bioss	bs-2639R	1/100	PGE2
anti-CD40	Armenian Hamster anti-Rat	Monoclonal	Thermo Fisher Scientific	14-0402-82	1/500	CD40 (M1 macrophages)
anti-TFRC	Mouse anti-Rat	Monoclonal	Thermo Fisher Scientific	13-6800	1/250	Transferrin receptor (M2 macrophages)
anti-Mcpt1	Goat anti-Rat	Polyclonal	Santa Cruz	sc-17041	1/100	Mast Cell Protease 1 (C-15)

Table 1. Primary antibodies used for immunofluorescence.

Protocol used in Janjic et al. Journal of Neuroimmunology. Volume 318, Pages 72-79. (2018).

The recovered control, sham and CCI sciatic nerves were prepared for immunohistochemical examination using mouse anti rat CD68 antibody (MCA341R, AbD Serotech, Raleigh, NC) and Alexa fluor 488 donkey anti-mouse secondary antibody (A-21202, Invitrogen, Carlsbad, CA) to assess the presence of macrophages that infiltrate the nerve. The double immunofluorescence studies were also performed to reveal the expression of COX-2 and

PGE2 in relationship to the CD68 positive infiltrating macrophages using, rabbit anti-COX-2, 1:100 (ab15191, AbD Serotech) and rabbit anti-prostaglandin E2 antibody, 1:100 (ab2318, AbD Serotech) along with mouse CD68, 1:100 (MCA341R, AbD Serotech) in treated and untreated rat groups. The secondary antibodies used were Alexa fluor 488 donkey anti-mouse, 1:200 (A-21202, Invitrogen), Alexa fluor 546 donkey anti-goat, 1:200 (A-11056, Invitrogen) and Alexa fluor 647 donkey anti-rabbit, 1:200 (A-31573, Invitrogen). All the antibody dilutions were prepared using 1:20 normal donkey serum in 1× PBS, pH 7.4. Antigen retrieval was performed during double immunofluorescence with COX-2 and CD68 primary antibodies, using sodium citrate buffer (10 mM sodium citrate, 0.1% Tween 20, pH 8.5). Antigen retrieval was not required during double immunofluorescence with PGE2 and CD68 primary antibodies.

Confocal Microscopy and Image Analysis

Protocol used in Saleem *et al. Acta Neuropathologica Communications volume 7, Article number: 108 (2019)*

All stained sections were scanned by the Nikon A1 confocal microscope equipped with six excitation solid-state diode lasers (405nm, 440nm, 488nm, 514nm, 561nm, and 640nm) and acquired with the Nikon NIS-Elements software. Confocal images for a comparative set were acquired with the same instrument settings (laser power, gain, etc.). Image analysis was performed with the FIJI distribution of ImageJ (version 1.52i) software.

For cell analysis, images were acquired in multiple channels to capture a marker for the cell, an additional protein-of-interest, as well as the NIRF signal emitted from the nanomedicine. Regions-of-interest were drawn around individual cells in an image and fluorescence intensity (mean fluorescence/ area) in each channel was measured. For each experiment, a threshold of mean intensity/ area was allocated in relevant confocal imaging channels (e.g. protein of interest and nanomedicine NIRF) by sampling multiple images to discriminate cells positive for a protein-of-interest, from those that were negative for the protein-of-interest. Subsequently, the total cell count, those cells positive for a protein of interest, and those positive for nanomedicine were recorded. Next, it was determined which cells were both positive for the protein-of-interest and the nanomedicine NIRF signal. Particle analysis for Mcpt1 and extracellular PGE2 was performed by first applying a threshold to the image to select stained particles and cells. Next, a size discrimination threshold was applied to exclude cells—to leave behind particles--and a particle count was performed for each image. Cell and particle count between test groups was analyzed by one-way ANOVA with Tukey's post hoc test to test multiple comparisons of group means. A confidence interval of 95% was set. Data are presented as mean ± SEM. The statistical software used to calculate one-way ANOVA is GraphPad Prism 6. In order to compare the differences between percentages of proteins-of-interest colocalized with macrophages between test groups, Pearson Chi-Square, and Fisher's exact tests were utilized and performed on IBM SPSS Statistics 25 software. A confidence interval of 95% was set, and a Fisher's exact test p-value is computed.

Protocol used in Janjic et al. Journal of Neuroimmunology. Volume 318, Pages 72-79. (2018).

Confocal microscopy was performed on a Leica SP2 spectral Laser Scanning Confocal microscope and corresponding image analysis with Leica LSC Confocal microscope software. The quantification analysis was performed for the double immunofluorescence slides stained with either COX-2 or PGE2 and CD68 antibodies, in three treated CBX-NE and three untreated DF-NE CCI rats. Confocal images for a comparative set were acquired with the same instrument settings (laser power, PMT voltage, pin hole, etc.). To determine any changes in the relative number of macrophages in the treated and untreated conditions, six regions of interest (ROIs) were chosen in each captured field-of-view of the ipsilateral sciatic nerve sections stained for CD68 positive cells for the CCI treated and untreated groups. At least two to three field of views were used for each of the rat nerve section to obtain 12–18 ROIs for each of the rats for a total of 48–54 ROIs per condition (i.e. CCI treated or untreated). Mean fluorescence intensity of CD68 stained sections was averaged from all the ROIs for the CCI drug ($n = 54$) and the CCI no drug ($n = 48$) conditions. No significant variation in the mean fluorescence intensity was found among individually identified macrophages in the treated or untreated groups. Therefore, the differences in the average mean fluorescence intensity per unit area among treated and untreated groups indicates differences in the relative number of macrophages between the two groups. The relative expression of COX-2 and PGE2 in the macrophages was determined by finding the ratios of the mean fluorescence intensity of COX-2 to the mean fluorescence intensity of CD68 in the same macrophage, and separately the ratios of the mean fluorescence intensity PGE2 in a given macrophage in both cases in drug and no drug conditions. The CD68 fluorescence intensity in the macrophages did not change in the drug or no drug condition and hence was used as a

reference for the ratio of the COX-2 or PGE2 fluorescence intensity in the treated or untreated CCI conditions. To analyze the COX-2 and PGE2 expression differences, a mean fluorescence intensity for either COX-2 or PGE2 was recorded in the individual CD68 positive cells. The changes in COX-2: macrophage or PGE2: macrophage mean fluorescence intensity ratio in treated or untreated group was indicative of relative changes in the COX-2 or PGE2 expression in the macrophages.

Chapter III.

Results: Low-dose NSAIDs reduce pain via macrophage targeted nanoemulsion delivery to neuroinflammation of the sciatic nerve in rat

Jelena M. Janjic, Kiran Vasudeva, Muzamil Saleem, Andrea Stevens, Lu Liu,

Sravan Patel, John A. Pollock

Reprinted from: Journal of Neuroimmunology, Volume 318, Pages 72–79. 2018. Requirement of permission waived for authors.

Contribution statement

Contributions by Muzamil Saleem

- M.S. contributed to writing and editing of manuscript.
- Animal care, surgery, tail vein injections, and NIRF imaging were carried out jointly by K.V., M.S. and A.S. under the guidance of J.A.P.
- M.S. produced graphic layout of Figures 5 and 6.
- Confocal microscopy of infiltrated macrophages in the sciatic nerve with nanoemulsion shown in Figure 5 performed by M.S.
- Behavioral testing and statistical analysis shown in Figure 6 performed by M.S.

- NIRF image quantification and statistical analysis in Figure 6 was performed by M.S. under the guidance of J.A.P.

Contributions by co-authors

- J.M.J. produced the nanoemulsion and designed the overall approach for targeting the COX-2 enzyme in macrophages in the context of neuropathic pain. The nanoemulsion was further fabricated by L.L. and S.P. under the guidance of J.M.J.
- Stability of nanoemulsion was assessed by J.M.J, L.L. and S.P.
- Confocal microscopy of macrophage (RAW 264.7 cells) was performed by J.M.J. and L.L.
- Macrophage (RAW 264.7 cells) viability and PGE2 release inhibition was performed by L.L.
- Statistical analysis in Figure 5 was performed by L.L. under the guidance of J.M.J.
- The immunohistochemistry and confocal microscopy and statistical analysis in Figure 7 were carried out by K.V. with J.A.P.

Highlights

- Nanoemulsion with near IR dye and NSAID deliver drug to site of inflammation.
- Drug delivery reduces inflammation visualized in live animals by near IR.
- Drug delivery reduces macrophage infiltration at site of injury, and COX-2, PGE2.
- Drug delivery provides relief from behavioral hypersensitivity.
- A single dose is 2000–3000-fold less drug than normal twice daily oral dosing.

Abstract

Neuroinflammation involving macrophages elevates Prostaglandin E2, associated with neuropathic pain. Treatment with non-steroidal anti-inflammatory drugs (NSAIDs) inhibits cyclooxygenase, reducing PGE2. However, NSAIDs cause physiological complications. We developed nanoemulsions incorporating celecoxib and near infrared dye. Intravenous injected nanoemulsion is incorporated into monocytes that accumulate at the injury; revealed in live animals by fluorescence. A single dose (celecoxib 0.24 mg/kg) provides targeted delivery in chronic constriction injury rats, resulting in significant reduction in the visualized inflammation, infiltration of macrophages, COX-2 and PGE2. Animals exhibit relief from hypersensitivity persisting at least four-days. The total body burden of drug is reduced by >2000 fold over oral drug delivery.

2. Materials and methods

Please refer to chapter 2 for comprehensive materials and methods.

3. Results

3.1. Nanoemulsion development and quality control

We have chosen nanoemulsions as our formulation platform because they can increase drug solubility and bioavailability [98–102] and can be produced on an industrial scale [98,103,104]. The triphasic nanoemulsions presented here are composed of three immiscible liquids: perfluoro-15-crown-5 as the perfluorocarbon oil, hydrocarbon oil (Miglyol 812N), and water (aqueous phase) where the hydrocarbon oil serves as the carrier for the drug and the NIRF dye, substances that have limited solubility in water (Figure 5A).

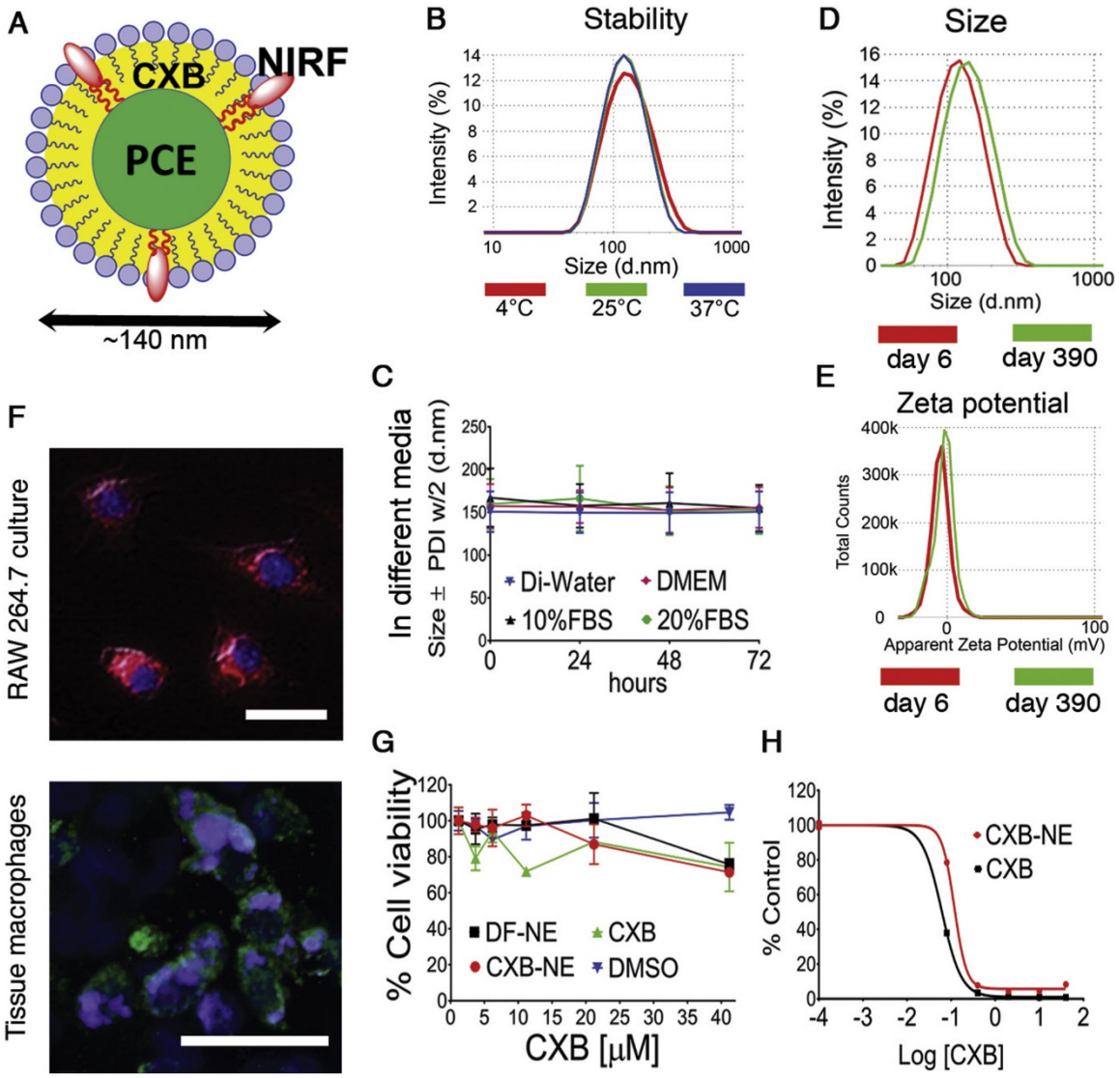

Figure 5. Nanoemulsion stability and pharmacological response.

(A) Tri-phasic nanoemulsion (perfluorocarbon, hydrocarbon, oil in water) loaded with celecoxib (CXB) and near infrared dye (NIRF); (B) CXB-NE (nanoemulsion with celecoxib) particle size distribution at 4 °C, 25 °C and 37 °C for three days; (C) CXB-NE stability in different biological media Di-water, DMEM, 10%FBS and 20% FBS measured by dynamic light scattering (DLS). Points represent means with error bars the SD from 3 independent measurements; (D) CXB-NE size distribution at day 6 and day 390; (E) CXB-NE zeta potential distribution at day 6 and day 390; (F) Fluorescent microscopy for NIR and DAPI for CXB-NE up-take by RAW 264.7 cell line (upper), CXB-NE up-take by tissue macrophages (lower). Scale bars are 20 µm; (G) Nanoemulsion pharmacological effect on RAW 264.7. % Cell viability in culture shown for CXB-NE, DF-NE (nanoemulsion without celecoxib), free drug CXB and DMSO. Points represent means with error bars the SD from 3 independent cultures; (H) a dose curve shows PGE2 release inhibition from LPS activated macrophages exposed to CXB-NE and free drug CXB. Points represent means with error bars the SD from 3 aliquots cultures. This figure is

reproduced from Janjic et al. Journal of Neuroimmunology. Volume 318, Pages 72-79. (2018). Muzamil Saleem produced the figure and contributed panel F. Members of the Dr. Janjic laboratory contributed the remaining panels.

Fig. 5B–E shows that the celecoxib loaded nanoemulsion (CXB-NE) exhibits very good stability under different storage conditions. The particle size distributions after three days of storage at 4°C, 25°C, and 37°C overlay each other, showing that there is no change in size (Fig. 5B). Colloidal stability was then assessed by serum stress test (Fig. 5C) showing that the nanoemulsion (CXB-NE) was stabile in all four types of biological media (Di-water, DMEM, 10% FBS in DMEM, and 20% FBS in DMEM) at elevated temperature 37°C for 3 days. The Z-Ave and zeta potential tests were performed upon storage on day 6 and again on day 390 reveling no change (Fig. 5D, E and Supplementary Fig. S1 found at https://doi.org/10.1016/j.jneuroim.2018.02.010). CXB-NE drug content analysis was conducted on 3 different batches manufactured by different personnel over time. There are no significant drug loading changes between the same formulations that are produced at different times (Supplementary Fig. S2 found at https://doi.org/10.1016/j.jneuroim.2018.02.010). Drug free nanoemulsion (DF-NE) were taken up by RAW 264.7 macrophage cells through phagocytosis over 3 h exposure (Fig. 5F and Supplementary Fig. S3 found at https://doi.org/10.1016/j.jneuroim.2018.02.010) and the nanoemulsion is also evident in macrophages that have infiltrated the injured rat sciatic nerve (Fig. 5F). We also evaluated the cytotoxicity effect and pharmacological effect of nanoemulsions in vitro on RAW 264.7 cells. With up to 40 μM (CXB containing CXB-NE and free CXB) there is no significant drop of cell generated ATP tested by CellTiter-Glo® luminescent cell viability assay, which indicates that there is good cell viability at 40 μM concentration. Furthermore, no significant change of cell viability was detected after RAW 264.7 cells were exposed to DF-NE and free drug solution

(Fig. 5G). Finally, we tested the effects of nanoemulsions on COX-2 enzyme activity in RAW 264.7 macrophages at different doses of celecoxib concentrations. When exposed to LPS, macrophages upregulate the COX-2 enzyme, which leads to increased production of PGE2. The inhibition of PGE2 release from LPS activated macrophages correlates with the concentration of the celecoxib in CXB-NE and free drug CXB (Fig. 5H and Supplementary Fig. S4 found at https://doi.org/10.1016/j.jneuroim.2018.02.010).

3.2. Live animal pain assessment

Chronic constriction injury (CCI) of the rat sciatic nerve leads to partial damage to the nerve and a neuroinflammatory response associated with hyper sensitivity, simulating common neuropathic conditions resulting from nerve lesion or disease in humans [24]. Resident macrophages get activated, along with recruitment of circulating hematogenous monocytes (precursors of macrophages) to the site of the injury where they differentiate into tissue infiltrated macrophages. The accumulation of active immune cells helps to remove any degenerating distal axons while at the same time producing inflammatory mediators that enhance an inflammatory cascade [25,105]. This, in turn, sensitizes the peripheral nerves leading to a change in the expression of ion channels and neurotransmitters. Sensitization is evident in behavior associated with increased hypersensitivity revealed with Von Frey filament stimulation of the affected paw, indicative of mechanical allodynia (Fig. 6A). Here we show that CCI animals are found to exhibit hypersensitivity by the sixth day after CCI surgery as compared to sham surgical animals.

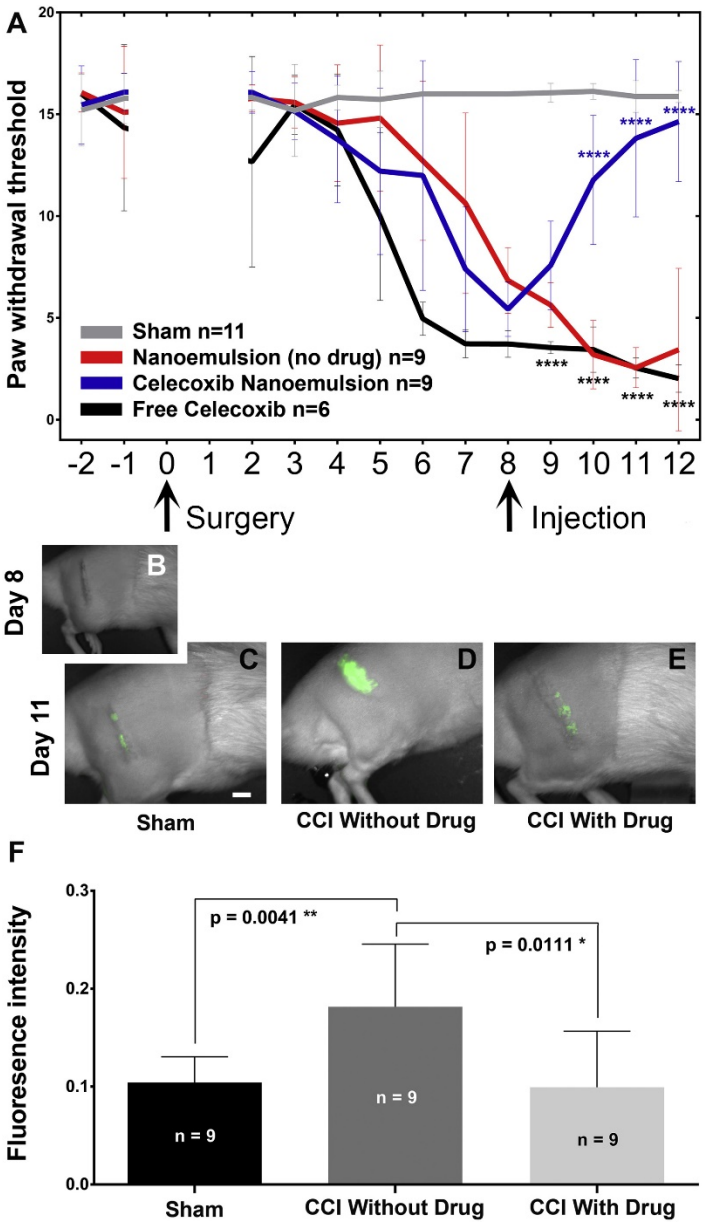

Figure 6. Celecoxib theranostic nanoemulsion provides relief from hypersensitivity associated with pain and reduces inflammation.

*(A) Mechanical allodynia is evident in CCI animals beginning on Day 6 post-surgery. The comparison of CCI without celecoxib to animals with drug $p < 0.0001$ for day 10, 11, 12 (Blue ****) while a comparison of CCI with celecoxib to animals with free celecoxib at the same concentration as that incorporated into nanoemulsion $p < .0001$ for day 9, 10, 11, 12 (Black ****). Analysis used repeated measures 2-WAY ANOVA with Bonferroni's multiple comparisons test. (B) On Day 8, prior to the injection of nanoemulsion, the live animals do not exhibit near infrared fluorescence (NIRF). Day 8 celecoxib-nanoemulsion injection via the tail vein provides pain relief (A, blue line). (C–E) shows the day 11 DiR*

NIRF signal that corresponds to the level of inflammation. (D) CCI with drug-loaded nanoemulsion exhibits a reduced NIRF signal as compared to (E) CCI without drug. (F) Analysis of the relative fluorescence intensity of the NIRF signal reveals that the CCI animals that receive nanoemulsion without drug exhibit elevated macrophage recruitment while celecoxib loaded nanoemulsion significantly reduces the relative fluorescence as compared to the signal in CCI animals without drug. This figure is reproduced from Janjic et al. Journal of Neuroimmunology. Volume 318, Pages 72-79. (2018). Muzamil Saleem produced the figure and contributed all panels.

By day 8 after CCI surgery, the paw withdrawal threshold reaches a level where there is marked pain-like bheavior[22,24] (Fig. 6A), at which point the animals receive a tail-vein injection of the corresponding nanoemulsion; either without drug (DF-NE), with celecoxib incorporated into the nanoemulsion (CXB-NE) or with a free form of celecoxib at the same dose (a concentration of 0.24 mg/kg celecoxib which amounts to 0.06 mg celecoxib for a rat that weighs approximately 250 g at this point in the experiment) – independent of nanoemulsion (free CXB + NE). By the very next day, animals injected with CXB-NE begin to exhibit a reversal in hypersensitivity, behavior that is markedly distinct from animals that received DF-NE or nanoemulsion with free-drug. On day 11, after behavioral assessment and light anesthesia, the animals were imaged for DiR NIRF, revealing a concentrated signal over the region of the affected sciatic nerve (Fig. 6C–E and Supplementary Fig. S5 found at https://doi.org/10.1016/j.jneuroim.2018.02.010). A clear difference is evident between the DiR NIRF signals for the animals receiving the celecoxib-loaded nanoemulsion CXB-NE (Fig. 6D) as compared to the CCI no-drug animals DF-NE (Fig. 6E). For the animals that received the low-dose celecoxib nanoemulsion, there is both a statistically significant difference (Fig. 6F, $p < 0.0037$) between the level of inflammation as reported by the NIRF and the level of hypersensitivity associated with the behavioral assessment of mechanical allodynia (Fig. 6A, $p < 0.0001$).

3.3. Histological evaluation of drug loaded nanoemulsion in injured sciatic nerve

The CCI affected sciatic nerve is infiltrated with macrophages [24,25]. Using confocal microscopy, we explore the density of macrophage infiltration as well as the expression of COX-2 and PGE2 when the celecoxib-loaded nanoemulsion- CXB-NE is introduced (Fig. 7). We find that in the CCI sciatic nerve, there is a high density of infiltrating macrophages (positive for CD68) associated with the nanoemulsion treatment that lacks celecoxib DF-NE (Fig. 7A). A drug-loaded nanoemulsion, CXB-NE, treatment is associated with a significant reduction in the number of CD68 positive macrophages (Fig. 7B, P; t-test, $p < 0.0001$). The contralateral, unaffected sciatic nerve from the left leg, as well as the sham animal's right sciatic nerve and the naïve animal's right sciatic nerve do not show any infiltrating macrophages (Fig. 7C–E). The affected (right) sciatic nerve treated with DF-NE exhibits COX-2 expression (Fig. 7F) whereas the affected sciatic nerve with CXB-NE exhibits a significant reduction in COX-2 (Fig. 7G, Q; t-test, $p < 0.0001$). The controls, which include the contralateral sciatic nerve as well as the sham and naïve nerves, do not exhibit detectable COX-2 expression (Fig. 7H–J). The assessment of PGE2 expression shows a signal in the CCI right sciatic nerve (Fig. 7K), which is significantly reduced in the CCI sciatic nerves where CXB-NE is present (Fig. 7L, R; t-test, $p < 0.0001$). To summarize, our analysis of the relative fluorescence levels for anti-CD68 as well as for anti-COX-2 and anti-PGE2 reveal statistically significant reduction of the number of infiltrating macrophages when CXB-NE is used. Similarly, there is a reduction in COX-2 and PGE2 expression. These changes are associated with the CBX-NE treated animal's reversal in pain associated hypersensitivity.

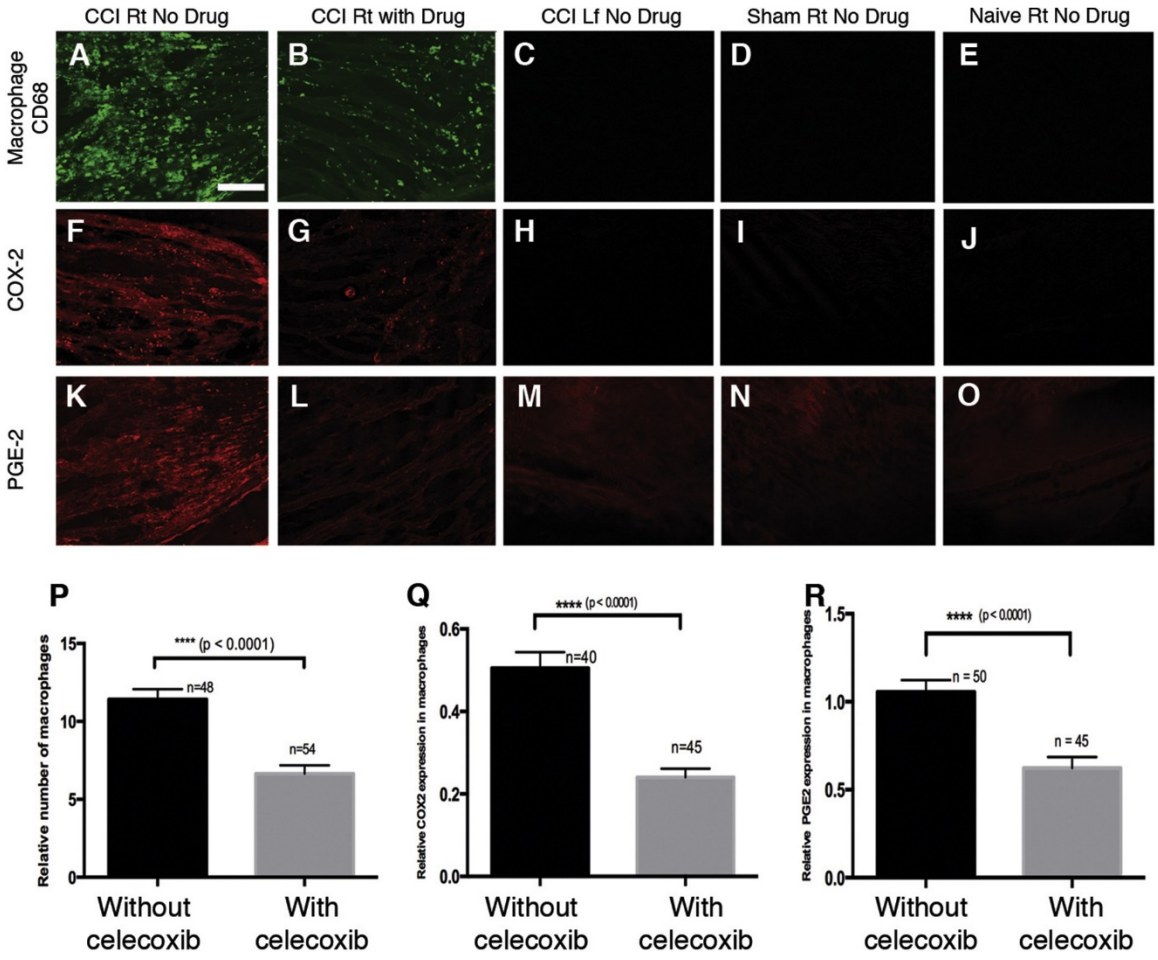

Figure 7. Celecoxib theranostic nanoemulsion reduces the number of infiltrating CD68 positive macrophages in the sciatic nerve, and reduces the expression of COX-2 and PGE2 detected by quantification of relative immunofluorescence.

There is infiltration of CD68 positive macrophages along with COX-2 and PGE2 expression in the ipsilateral sciatic nerve sections of the CCI group injected with the vehicle nanoemulsion (A, F, K) and the CCI group injected with the theranostic nanoemulsion containing the drug celecoxib (B, G, L). An apparent reduction in the expression of CD68, COX-2 and PGE2 is revealed in the CCI group injected with the theranostic nanoemulsion (B, G, L). Quantification of the relative fluorescence revealed significant reduction in mean fluorescence intensity per unit area for CD68 macrophages (P), COX-2 expression in macrophages (Q) and PGE-2 expression in macrophages (R in the CCI group treated with celecoxib-containing nanoemulsion (t-test, $p < 0.0001$). Ipsilateral sciatic nerve sections from the sham (D, I, N) and naïve control rats (E, J, O) injected with the vehicle nanoemulsion and contralateral sciatic nerve sections from the CCI rats injected with the vehicle nanoemulsion (C, H, M) do not exhibit CD68, COX-2 and PGE-2 expression. Bar = 150 μm. n = total number of regions of interest (ROIs) in (P) and number of macrophages chosen in (Q, R) from a total of three rats in either of the CCI groups. Bars represent Mean ± SEM. This figure is reproduced from Janjic et al. Journal of

Neuroimmunology. Volume 318, Pages 72-79. (2018). Kiran Vasudeva produced the figure and contributed all panels.

Chapter IV.

Results: Nanomedicine-driven neuropathic pain relief in rat model is associated with macrophage polarity and mast cell activation

Muzamil Saleem, Brooke Deal, Emily Nehl, Jelena M. Janjic, John A. Pollock

Results section reprinted from Saleem *et al. Acta Neuropathologica Communications volume 7, Article number: 108 (2019)*

Contribution statement

Contributions by Muzamil Saleem

- M.S. conceived the study, performed all experiments and wrote the manuscript under the guidance of J.A.P.

Contributions by co-authors

- J.M.J. produced the nanoemulsion and designed the overall approach for targeting the COX-2 enzyme in macrophages in the context of neuropathic pain. The nanoemulsion was further fabricated by Lu Liu under the guidance of J.M.J.
- J.A.P contributed to writing and editing the manuscript. B.D. contributed to editing the manuscript.
- A portion of the tissue used in this study was sectioned by B.D.

- E.N assisted in optimizing immunofluorescence staining procedures.

Results

Nanomedicine treatment relieves pain-like hypersensitivity for ~6 days

Manual von Frey mechanical allodynia testing was performed to measure pain-like hypersensitivity in rats modeled with neuropathic pain. A paw withdrawal threshold is calculated; a lower value infers a higher level of pain-like hypersensitivity. Baseline paw withdrawal thresholds were measured on two consecutive days preceding CCI and sham CCI surgery—where no statistical difference is seen between testing groups (Fig. 8a, b). The animals were given 1 day of rest following surgery, before resuming von Frey testing on consecutive days until they were euthanized on day 12 or day 18, depending on the testing group. Nanomedicine (CXB-NE) or vehicle (DF-NE) is injected on day-8 following surgery due to a significant increase ($p < 0.0001$) in pain-like hypersensitivity at this time-point in CCI compared to sham rats (Fig. 8a, b line 1). Following injection at day 8, nanomedicine treated rats (CXB-NE) show similar pain-like hypersensitivity to vehicle-treated rats (DF-NE), which is significantly higher ($p < 0.0001$) compared to sham rats (Fig. 8a, b line 2). At day 12 following surgery, CCI animals treated with nanomedicine (CXB-NE) showed a significant ($p < 0.0001$) reversal in pain-like hypersensitivity (Fig. 8a, b lines 4, 5); and the group that received vehicle

treatment showed significantly increased ($p < 0.0001$) pain-like hypersensitivity (Fig. 8a, b line 3). At day 18 following surgery, the nanomedicine treatment group returned to levels of pain-like hypersensitivity resembling that of the vehicle group; a significant difference ($p < 0.0001$) from the pain-relief state seen at day 12 (Fig. 8a, b line 6).

NIRF signal accumulation at the inflamed sciatic nerve of live animals is lowered after nanomedicine treatment

NIRF signal in live animals is imaged in a preclinical fluorescence imager under anesthesia before and after injection of nanomedicine (CXB-NE) or vehicle (DF-NE) on day-8 after surgery, and then on day 11 in one group, and day 17 in another. We have previously shown that nanoemulsion is phagocytosed by macrophages [44,72], before infiltrating the sciatic nerve of CCI rats—and that a measurable NIRF signal is detected above the ipsilateral sciatic nerve in live animals at day 11 post-surgery [23,24]. In the present study, we show that at pre-injection (day 8), there is no NIRF signal above the ipsilateral sciatic nerve of CCI animals (Fig. 8d). By day 11 we see a strong signal in the vehicle-treated CCI animals (Fig. 8e) and a significantly ($p = 0.0173$) reduced NIRF signal in nanomedicine treated animals (CXB-NE) (Fig. 8c, f). At day 17 post-surgery there is no significant difference between the level of NIRF signal in the DF-NE condition (Fig. 8g) compared to the CXB-NE (Fig 8. H) group. The NIRF signal in the day 17 vehicle-treated group (Fig. 8c, g) is significantly lower ($p = 0.0040$) than the day 11 vehicle group (Fig. 8c, e).

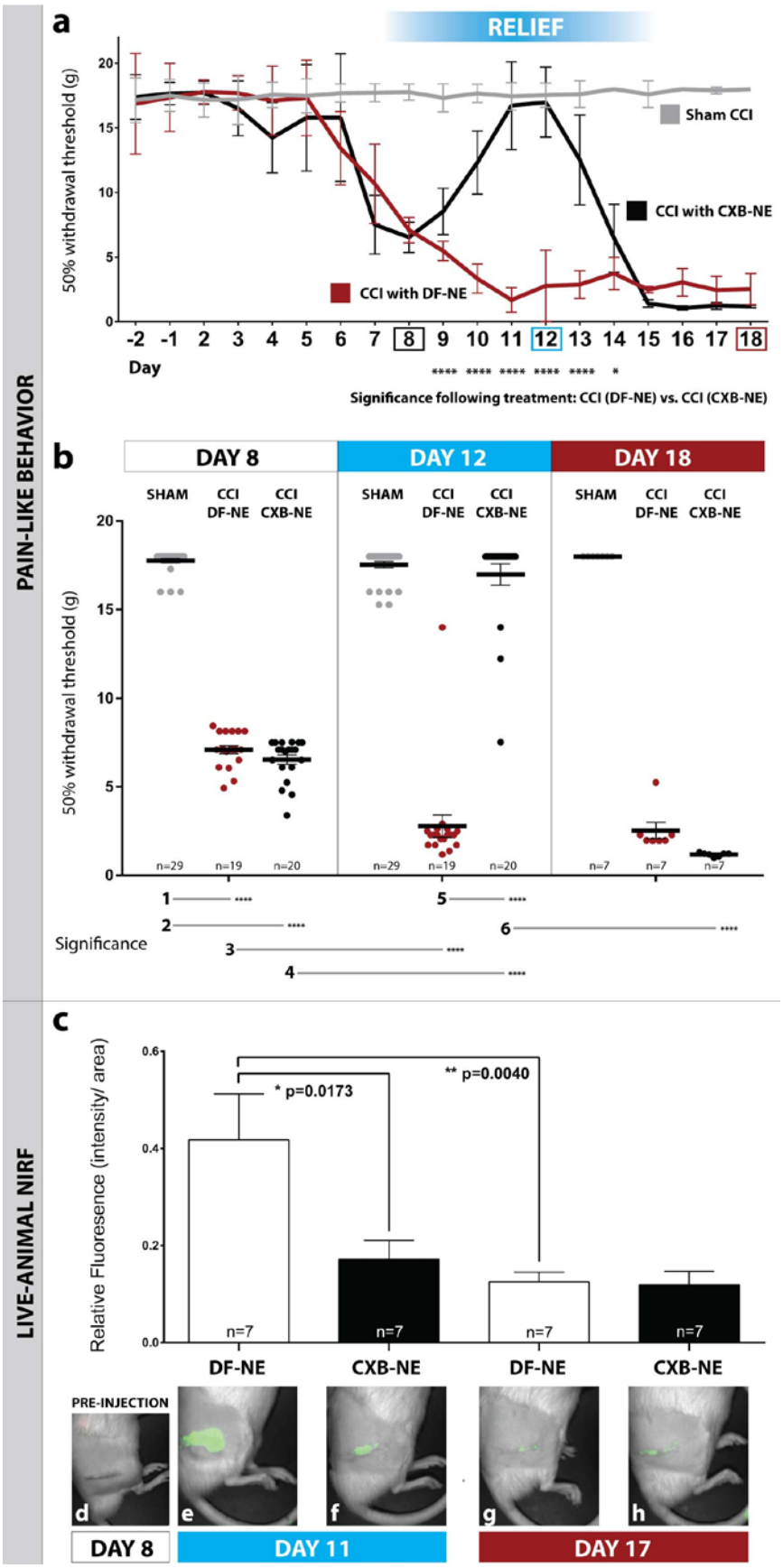
PAIN-LIKE BEHAVIOR
a
RELIEF
50% withdrawal threshold (g)
Sham CCI
CCI with CXB-NE
CCI with DF-NE
Day
Significance following treatment: CCI (DF-NE) vs. CCI (CXB-NE)
b
DAY 8
DAY 12
DAY 18
SHAM
CCI DF-NE
CCI CXB-NE
50% withdrawal threshold (g)
n=29
n=19
n=20
n=7
Significance
LIVE-ANIMAL NIRF
c
Relative Fluorescence (intensity/ area)
* p=0.0173
** p=0.0040
DF-NE
CXB-NE
PRE-INJECTION
DAY 8
DAY 11
DAY 17

Figure 8. Mechanical stimulus-evoked pain-like hypersensitivity testing and live animal NIRF imaging.

*The manual up-down von Frey test is performed on the days outlined in Fig. 3a to evaluate mechanical allodynia. Panel **a** shows results from daily testing, and panel **b** summarizes 50% withdrawal thresholds at day-8, day 12, and day 18. At day 8, both CCI animal groups are significantly more hypersensitive than sham CCI animals (**a** and **b**). Nanomedicine is injected after behavioral testing is completed on day 8. The CCI animals given CXB-NE show a significant reversal in withdrawal thresholds at day 12, a level similar to the sham CCI group (**a** and **b**). The reversal in pain-like hypersensitivity lasts for approximately 6 days (shown in **a**, day 9 to 14; ****p < 0.0001, *p = 0.0257, two-way ANOVA with Tukey's posthoc test) and by day 18 the withdrawal threshold lowers back to a level indicative of a chronic pain state (**a** and **b**). All associated data analysis can be found here [57]: https://doi.org/10.6084/m9.figshare.8287823.v1. Whole-body live-animal NIRF imaging is performed on day 11 and day 17, the evening before day 12 and day 18 animals respectively are euthanized, and perfusion fixed. In the live animals at day-11, there is a significant decrease in NIRF signal in CCI animals given CXB-NE (**c** and **f**) compared to animals administered with DF-NE (**c** and **e**). The animals show no fluorescence at day 8, prior to injection (**d**). At day 17, NIRF signal at the site of the ipsilateral sciatic nerve is significantly decreased in the CCI group given DF-NE (**g**). A similar level of NIRF signal is observed at day 17 in the CCI group given CXB-NE (**h**). Pain behavior data is represented as mean ± SD (n = 7–29 animals; *p < 0.05, ****p < 0.0001, one-way ANOVA with Tukey's posthoc test). In vivo imaging data is represented as mean ± SEM (n = 7 animals; *p < 0.05, **p < 0.01, one-way ANOVA with Tukey's post hoc test). This figure is reproduced from Saleem et al. Acta Neuropathologica Communications. Volume 7, Article number: 108 (2019). Link: https://actaneurocomms.biomedcentral.com/articles/10.1186/s40478-019-0762-y/figures/2. Muzamil Saleem performed related experiments and produced the figure.*

Ex vivo tissue analysis of macrophage infiltration at the affected sciatic nerve confirms a reduction in inflammation

Macrophage infiltration at the ipsilateral sciatic nerve of CCI rats was assessed by anti-CD68 immunofluorescence staining. A significant reduction ($p < 0.0001$) in infiltration is

revealed at day 12 in nanomedicine (CXB-NE) treated rats (Fig. 9b, e). At day 18, there is no effect of CXB-NE treatment (Fig. 9c, d, e), and significantly reduced ($p < 0.0001$) macrophage infiltration in the vehicle group (DF-NE) compared to day 12 (Fig. 9a, c, e). Infiltration in the day 18 nanomedicine treatment group resembles levels seen in the day 12 CXB-NE and day 18 DF-NE groups (Fig. 9b, c, d). The percentage of infiltrating macrophages that are positive for nanomedicine NIRF signal was analyzed, and in both conditions at the injured sciatic nerve, constitutes approximately 60% of macrophages (Fig. 9. e).

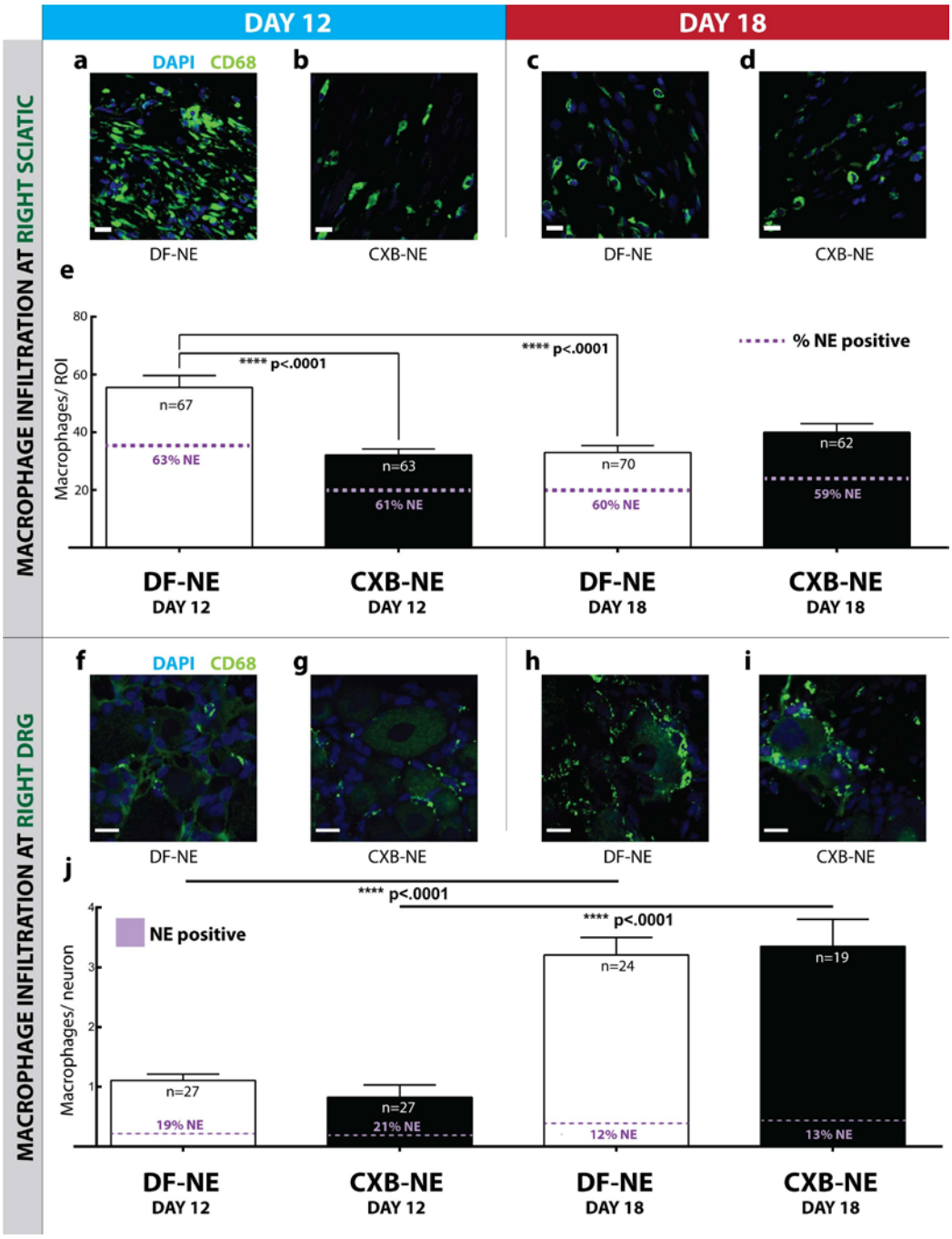

Figure 9. Macrophage infiltration at the ipsilateral sciatic nerve and associated DRG.

*At day 12, macrophage infiltration to the ipsilateral sciatic nerve is significantly reduced in the CXB-NE group (**b** and **e**), compared to the DF-NE group (**a** and **e**) ($p < 0.0001$). There is no significant difference between DF-NE and CXB-NE groups at day 18 (**c**, **d** and **e**). At both day 12 and day 18, the percentage of sciatic nerve infiltrating macrophages that are positive for nanomedicine ranges from 59 to 63% (**e**). A measure of macrophage infiltration per DRG cell body is calculated. These percentages are lower at the DRG: 19% in the day 12 DF-NE condition, 21% in the day 12 CXB-NE condition, 12% in the day 18 DF-NE condition and 13%*

*in the day 18 CXB-NE condition (**j**). Seen here in this animation are nanoemulsion droplets inside macrophages [58]: https://doi.org/10.6084/m9.figshare.8142962. In the DRG, there is no significant difference between the DF-NE and CXB-NE groups at both day 12 and day 18. Macrophage infiltration at the ipsilateral L4 and L5 DRG is significantly higher at day 18 in both the DF-NE ($p < 0.0001$) and CXB-NE ($p < 0.0001$) groups (**h**, **i** and **j**) compared to respective groups at day 12 (**f** and **g**). All scale bars are 15 μm. Data is represented as mean ± SEM (n = 3 animals, 19–42 ROI; ****$p < 0.0001$, one-way ANOVA with Tukey's post hoc test). This figure is reproduced from Saleem et al. Acta Neuropathologica Communications. Volume 7, Article number: 108 (2019). Link: https://actaneurocomms.biomedcentral.com/articles/10.1186/s40478-019-0762-y/figures/3. Muzamil Saleem performed related experiments and produced the figure.*

Nanomedicine treatment does not reduce macrophage infiltration at the L4 and L5 DRG associated with the inflamed sciatic nerve

The L4 and L5 DRG are associated with the sciatic nerve—approximately 98-99% of all sciatic nerve DRG cell bodies are located here [106]. Macrophage infiltration at the DRG was quantified by calculating the average number of macrophages per cell body. CD68 analysis of DRG neurons revealed a significant increase of macrophage infiltration at day 18 compared to day 12 in both the vehicle ($p < 0.0001$) and nanomedicine ($p < 0.0001$) treated groups (Fig. 9f-j). Nanomedicine treatment did not significantly reduce macrophage infiltration to the ipsilateral DRG of CCI rats in either the day 12 or day 18 groups. Approximately 20% of macrophages infiltrating the DRG at day 12 are positive for nanomedicine. This percentage approximately halves at day 18, indicating clearance of macrophages, and infiltration of new monocytes.

COX-2 positive macrophages in the ipsilateral sciatic nerve are significantly reduced following nanomedicine treatment

Tissue sections from the ipsilateral sciatic nerve were multi-stained with anti-CD68 (macrophage marker) and an antibody against the COX-2 enzyme (Additional file 1: Table S1. Link: https://static-content.springer.com/esm/art%3A10.1186%2Fs40478-019-0762-y/MediaObjects/40478_2019_762_MOESM1_ESM.pdf) as well as the nuclear stain DAPI. The fluorescence intensity from these stains, as well as the NIRF signal emitted from the nanomedicine, was captured with four laser imaging channels using confocal microscopy. By counting individually labeled macrophages during image analysis, in addition to a measurement of macrophage infiltration, it was possible to calculate the percentage of these infiltrating macrophages that were positive for COX-2 expression and the presence of nanomedicine. The dose of nanomedicine is not saturating; not every macrophage is expected to have accumulated nanomedicine. At day 12, a remarkable 56.5% reduction (Fisher's exact test, $p < 0.0001$) in COX-2 positive macrophages was observed in rats that were treated with nanomedicine (CXB-NE) (Fig. 10a, b, e, f). Levels of COX-2 positive macrophages in the CXB-NE group at day 18 were similar to those seen in the vehicle-treated day 12 group (Fig. 4a10a, c, d, e, g, h). Of the COX-2 positive macrophages, the highest extent of nanomedicine colocalization was seen in the day 12 nanomedicine treatment group (Fig. 10f)—significantly higher than all other groups ($p < 0.0001$). The attenuation of COX-2 by CXB-NE is believed to halt further induction of the enzyme. Protein staining for COX-2 is not indicative of whether the protein has been inactivated by celecoxib—although it is expected that it has been in the day 12 CXB-NE condition due to the reduction in PGE2.

Extracellular PGE2 at the ipsilateral sciatic nerve is significantly reduced following nanomedicine treatment

The expression of extracellular PGE2 was measured as a particle count at the ipsilateral sciatic nerve of CCI rats. A significant reduction ($p < 0.0001$) of extracellular PGE2 was observed at day 12 in nanomedicine treated rats (Fig. 10i, j, k). This coincides with the observed reduction of macrophage-expressed COX-2 enzyme (Fig. 10b, f), from which PGE2 is synthesized. At day 18, extracellular PGE2 is significantly reduced: approximately 4-fold ($p < 0.0001$) in both the DF-NE group and CXB-NE group, compared to their respective groups at day 12.

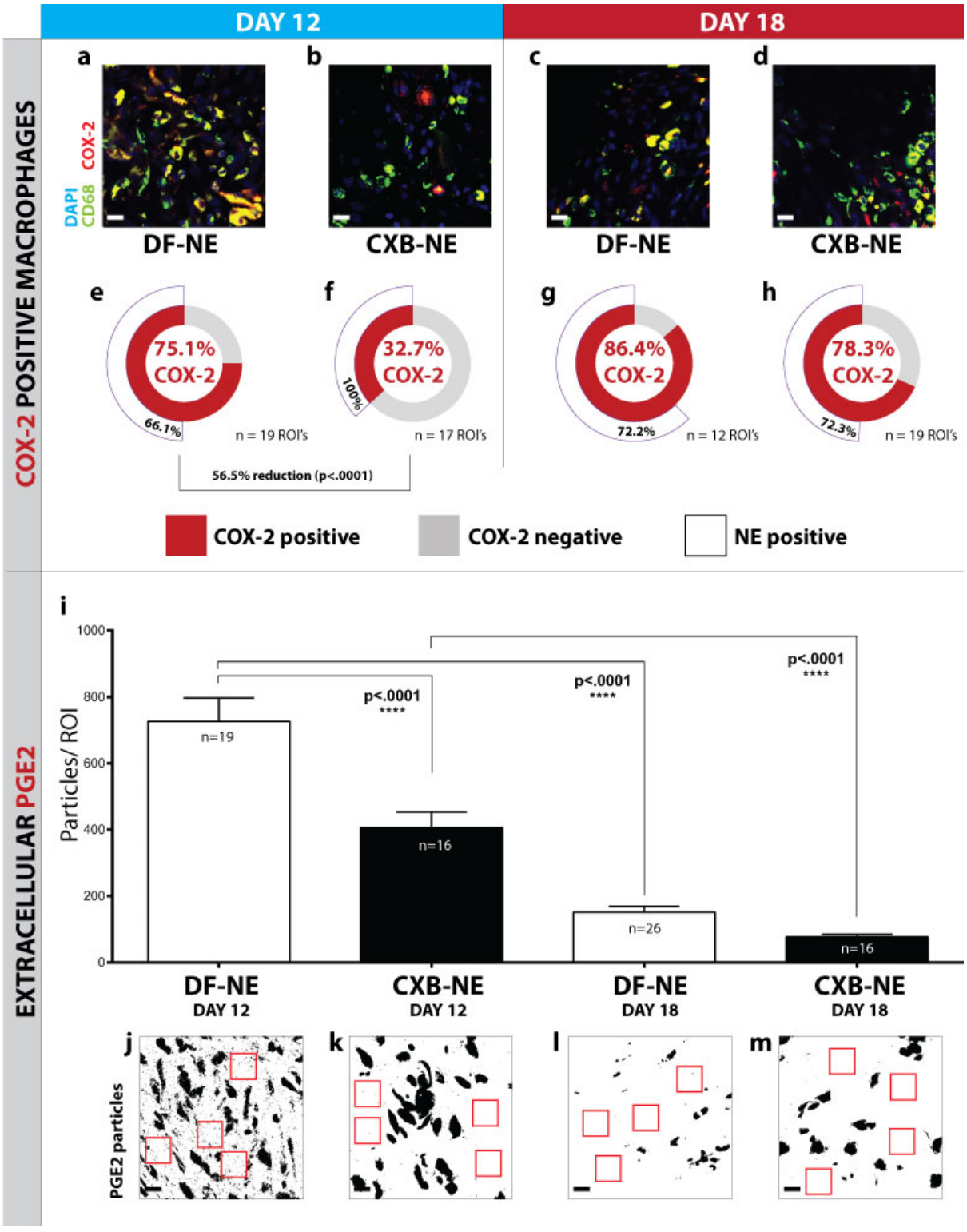

Figure 10. Macrophage COX-2 and extracellular PGE2 expression is reduced following CXB-NE treatment.

*Macrophage expression of COX-2 enzyme and extracellular expression of its synthesized cytokine, PGE2, is measured at the ipsilateral sciatic nerve. There is a significant 56.5% reduction (Fisher's exact test, $p < 0.0001$) of COX-2 positive macrophages at day 12 in the CXB-NE group (**b** and **f**), compared to the DF-NE group (**a** and **e**). Extracellular PGE2 levels are also significantly reduced ($p < 0.0001$) (**i** and **k**) in the day 12 CXB-NE group (**k**) compared to the day 12 DF-NE group (**j**). The representative images--**j**, **k**, **l** and **m**—have been converted to binary images to more clearly reveal the extracellular PGE2, which is counted by applying a size threshold during analysis. The larger particles denote COX-2 stained macrophages, and the smaller particles represent extracellular PGE2, examples of which are represented within the red boxes. At day 18, the proportion of COX-2 positive macrophages in the DF-NE (**c** and **g**) and CXB-NE (**d** and **h**) groups rises to levels comparable to the day 12 DF-NE group (**e**). Extracellular PGE2 is significantly reduced at day 18 in both the DF-NE (**i** and **l**) ($p < 0.0001$) and CXB-NE (**i** and **m**) ($p < 0.0001$) groups. Macrophages positive for COX-2 were analyzed to report on their colocalization with nanomedicine NIRF signal (white segment in **e-f**). A significantly higher co-localization of nanomedicine with COX-2 positive macrophages was observed in the day 12 CXB-NE condition ($p < 0.0001$). All scale bars are 15 μm. The significance of COX-2 positive macrophage percent difference between conditions is represented as a Fisher's exact test p-value; 95% confidence interval. Extracellular PGE2 data are represented as mean ± SEM (n = 3 animals, 16–26 ROI; ****$p < 0.0001$, one-way ANOVA with Tukey's post hoc test). This figure is reproduced from Saleem et al. Acta Neuropathologica Communications. Volume 7, Article number: 108 (2019). Link: https://actaneurocomms.biomedcentral.com/articles/10.1186/s40478-019-0762-y/figures/4. Muzamil Saleem performed related experiments and produced the figure.*

Nanomedicine treatment significantly reduces the number of M1 pro-inflammatory macrophages while increasing the number of M2 anti-inflammatory macrophages in the sciatic nerve

Tissue sections from the ipsilateral sciatic nerve were stained with CD68 (macrophage marker), nuclear stain DAPI and an antibody against the CD40, a marker for M1 pro-inflammatory macrophages (Additional file 1: Table S1. Link: https://static-content.springer.com/esm/art%3A10.1186%2Fs40478-019-0762-

y/MediaObjects/40478_2019_762_MOESM1_ESM.pdf). In a separate experiment, anti-TFRC (Additional file 1: Table S1. Link: https://static-content.springer.com/esm/art%3A10.1186%2Fs40478-019-0762-y/MediaObjects/40478_2019_762_MOESM1_ESM.pdf), a marker for M2 anti-inflammatory macrophages was co-stained alongside CD68-positive macrophages and DAPI. The fluorescence signal from these stains, as well as the NIRF signal emitted from the nanomedicine, was captured in multiple imaging channels using confocal microscopy. The percentage of macrophages positive for either M1 or M2 markers was calculated, in addition to counting the proportion of these cells positive for nanomedicine. A 27.5% reduction (Fisher's exact test, $p < 0.0001$) of M1 macrophages was measured in ipsilateral sciatic nerve tissue of nanomedicine treated (CXB-NE) CCI rats (Fig. 11b, f) compared to the day 12 vehicle treatment group (Fig. 11a, e). At day 18, the percentage of M1-positive macrophages in the nanomedicine (CXB-NE) group increased by 56.7% (Fisher's exact test, $p < 0.0001$), compared to day 12. There is a remarkably significant 69.0% increase (Fisher's exact test, $p < 0.0001$) in the number of M2 anti-inflammatory macrophages found in nanomedicine treated rats at day 12, compared to the vehicle group Fig. 11i, j, m, n). The proportion of M2-positive macrophages shows a decrease of 41.8% (Fisher's exact test, $p < 0.0001$) at day 18 compared to day 12 in nanomedicine treatment groups (Fig. 11j, n, l, p). Nanomedicine NIRF colocalization with M2 macrophages is significantly lower in both the DF-NE (Fisher's exact test, $p < 0.0001$) and CXB-NE (Fisher's exact test, $p < 0.0001$) groups at day 18 compared to day 12 (Fig. 11m-p), suggesting that there is a population of M2 macrophages that have fused to form MGCs. At day 18, nanomedicine NIRF colocalization with M2 macrophages is significantly lower (Fisher's exact test, $p = 0.000376$) in

the CXB-NE condition compared to the DF-NE condition, likely indicating that a greater proportion of M2 macrophages have fused to form MGCs.

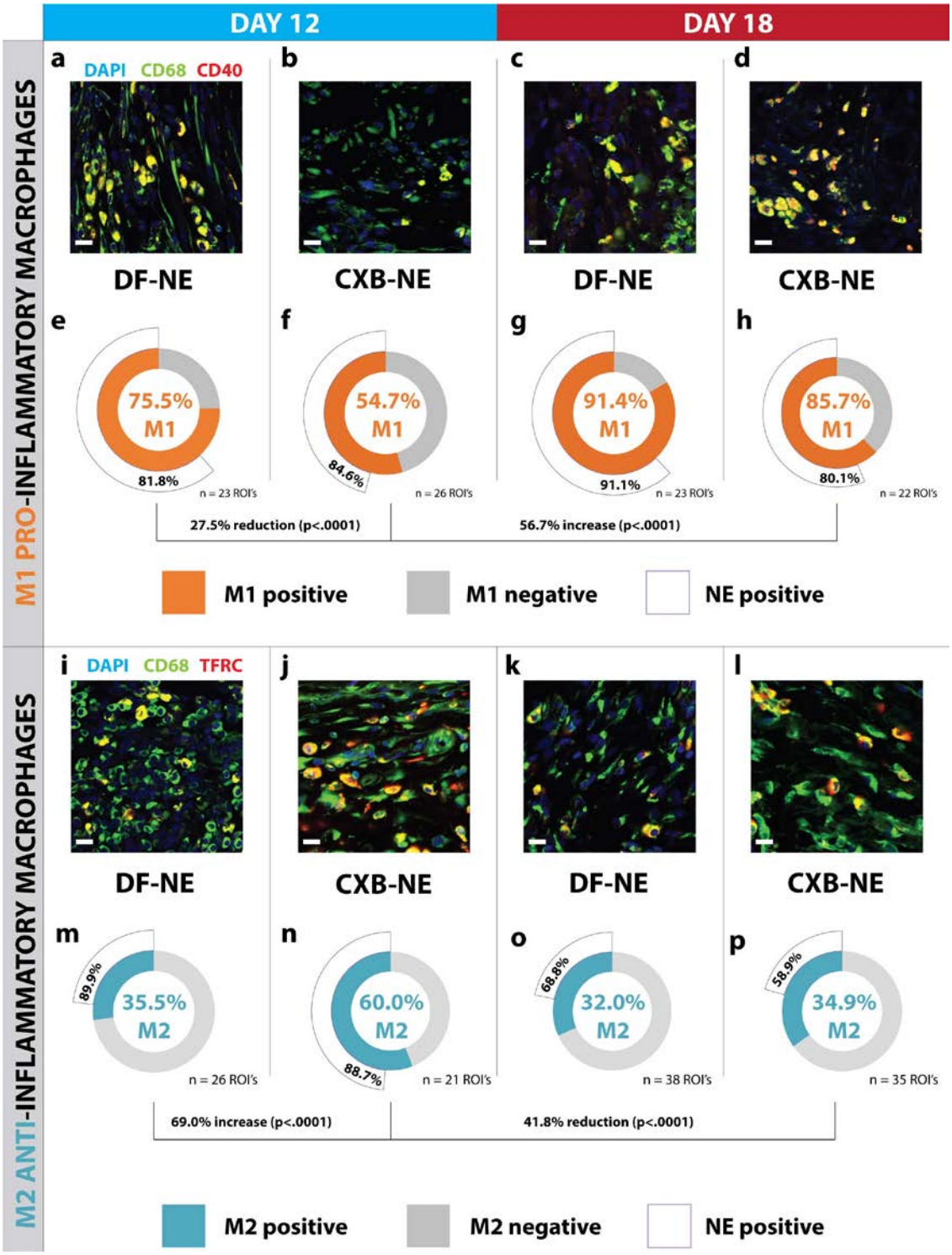

Figure 11. Macrophage polarity shifts from pro-inflammatory M1 to anti-inflammatory M2 phenotype in the day 12 CXB-NE group.

*There is a 27.5% reduction ($p < 0.0001$) in M1 pro-inflammatory macrophages in the day 12 CXB-NE group (**b** and **f**) compared to the day 12 DF-NE group (**a** and **e**). At day 18 the percentage of M1 macrophages increases by 56.7 to 85.7% in the nanomedicine treated (CXB-NE) rats, compared to day 12 (**d** and **h**). At day 18, levels of M1-positive macrophages rise to 91.4% per ROI in the DF-NE group (**c** and **g**). There are no significant differences in nanomedicine co-localization with M1 macrophages. The percentage of anti-inflammatory M2 macrophages increases significantly ($p < 0.0001$) by 69.0% in the day 12 CXB-NE group (**j** and **n**) compared to the DF-NE animals (**i** and **m**). At day 18, the proportion of M2 macrophages in the CXB-NE group (**l** and **p**) drops significantly ($p < 0.0001$) by 41.8%, whilst there is no significant difference in the DF-NE group at day 18 (**k** and **o**), compared to day 12 (**i** and **m**). M2 macrophages in the day 18 conditions show a significantly lower nanomedicine NIRF colocalization compared to both the DF-NE (Fisher's exact test, $p < 0.0001$) and CXB-NE (Fisher's exact test, $p < 0.0001$) day 12 groups. At day 18, the percentage of M2 macrophages that are positive for nanomedicine NIRF signal is significantly lower in the CXB-NE group (Fisher's exact test, $p = 0.000376$) compared to the DF-NE group. All scale bars are 15 μm. The significance of M1 and M2 positive macrophage percent difference between conditions is represented as a Fisher's exact test p-value; 95% confidence interval. n = 3 animals, 21–33 ROI. This figure is reproduced from Saleem et al. Acta Neuropathologica Communications. Volume 7, Article number: 108 (2019). Link: https://actaneurocomms.biomedcentral.com/articles/10.1186/s40478-019-0762-y/figures/5. Muzamil Saleem performed related experiments and produced the figure.*

CD68-positive multinucleated giant cells (MGCs) in the ipsilateral sciatic nerve appear prominently by day 18 following surgery, and at significantly higher counts following nanomedicine treatment

During an inflammatory reaction, monocytes and macrophages can fuse to form multinucleated giant cells (Fig. 12a, b). Composed of several fused cells, MGCs were observed to be approximately 20 – 30 μm at their greatest diameter (Fig. 12a, b; white arrows), and

internalized NIRF signal from the nanomedicine was observed (Fig. 12a, b; green arrows). Positively stained with anti-CD68, virtually no MGCs were seen at day 12 in either the nanomedicine or vehicle treatment groups (Fig. 12c). However, MGCs were observed in greater quantities at day 18, with significantly higher counts ($p < 0.0001$) in the nanomedicine treatment group (Fig. 12c).

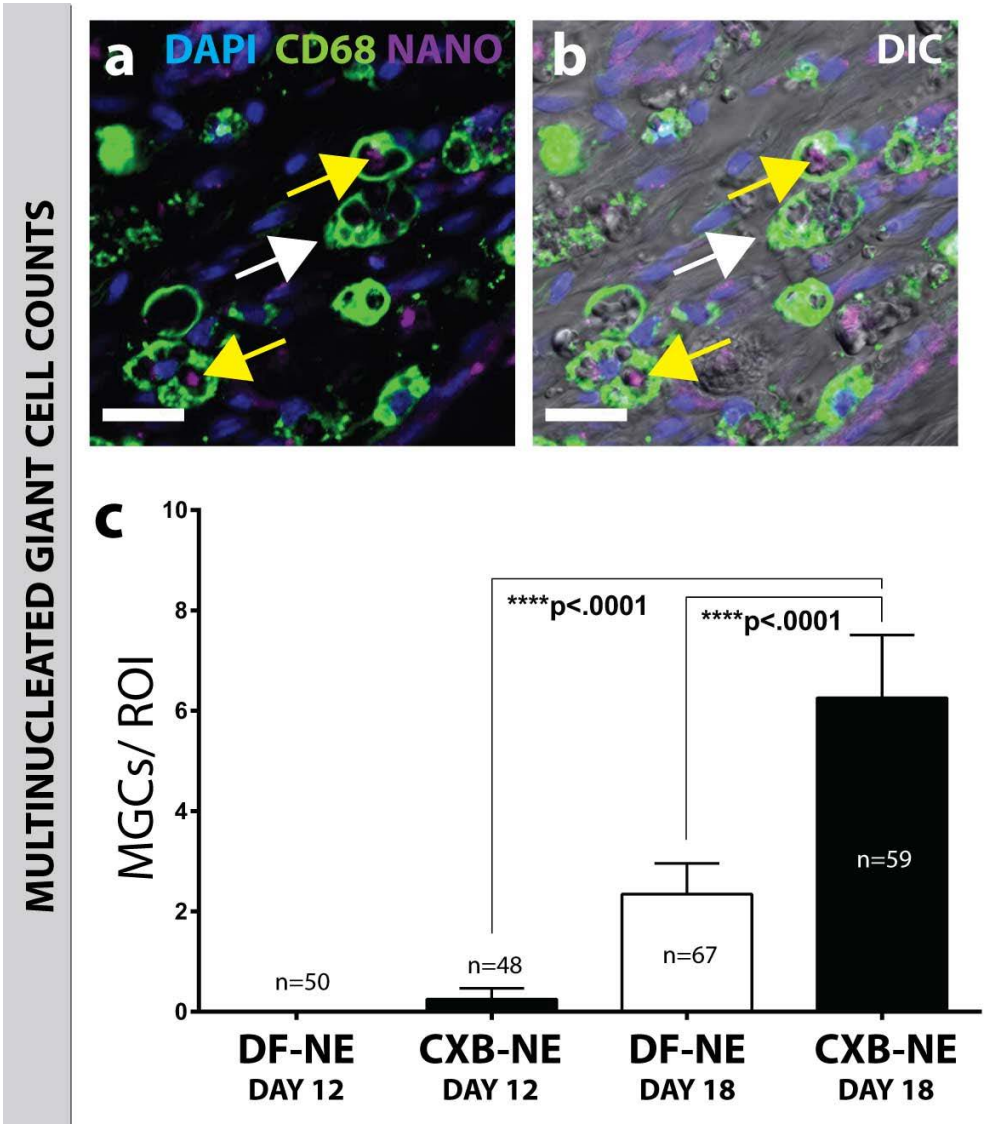

Figure 12. Macrophage fuse to form multinucleated giant cells at day 18.

*Macrophages can fuse to form multinucleated giant cells (a, b). MGCs were observed at higher numbers at day 18, in both the CXB-NE and DF-NE conditions (c). The day 18 CXB-NE group had significantly more MGCs compared to the day 18 DF-NE ($p < .0001$) and the day 12 CXB-NE ($p < .0001$) groups (c). White arrows point to CD68 staining showing macrophages fused into MGCs. Yellow arrows indicate a nanomedicine signal inside MGCs. Seen here in this animation are M2 macrophages fused to form a multinucleated giant cell [59]: https://doi.org/10.6084/m9.figshare.8142950. DAPI stained nuclei are blue, CD68 stained MGCs composed of macrophages are green, and the NIRF from nanomedicine (NANO) is purple. Panel a is a merge of DAPI, CD68 and nanomedicine channels (NANO); and panel b is a merge that additionally includes a DIC channel in order to visualize nerve tissue morphology. All scale bars are 20 μm. Data are represented as mean ± SEM (n = 3 animals, 48–59 ROI; ****$p < 0.0001$, one-way ANOVA with Tukey's post hoc test). This figure is reproduced from Saleem et al. Acta Neuropathologica Communications. Volume 7, Article number: 108 (2019). Link: https://actaneurocomms.biomedcentral.com/articles/10.1186/s40478-019-0762-y/figures/6. Muzamil Saleem performed related experiments and produced the figure.*

Number of infiltrating mast cells in the ipsilateral sciatic nerve is significantly reduced following nanomedicine treatment and not in the ipsilateral DRG

Mast cells are a key component of the inflammatory response and are integral in the potentiation of chronic pain [82]. In addition to resident populations in most tissues, there is a circulation of mast cell progenitors in the blood, which can infiltrate sites of inflammation [107]. Given the crosstalk between mast cells, other immune cells – such as macrophages – and the nervous system, we investigate mast cell expression at the ipsilateral sciatic nerve and associated L4 and L5 DRG. The number of mast cells – indicated by positive staining for Mcpt1 – were counted for each region of interest from sciatic nerve tissue and DRG sections. The number of mast cells per ROI was significantly reduced ($p = 0.0014$) in the CXB-NE nanomedicine treated rats (Fig. 13c) at day 12 compared to the DF-NE vehicle-treated group (Fig. 13b). There was a

reduction in mast cell numbers in both treatment groups at day 18 (Fig. 13d, e). There were significantly less ($p = 0.0303$) mast cells per ROI at day 18 in the vehicle treatment group (Fig. 13d) as compared to day 12 (Fig. 13b). In the location of the ipsilateral DRG cell bodies, there are no significant differences between mast cell numbers among treatment groups, suggesting that the cells are resident in this location, and have not infiltrated.

Mast cell degranulation is significantly reduced following nanomedicine treatment

The diverse effector functions of mast cells are mediated by the secretion of a wide variety of biologically active products that are contained in secretory granules. Extracellular staining of Mcpt1 was indicative of a major component of mast cell granules, and particle counts were interpreted as the extent of mast cell degranulation. The number of Mcpt1 particles per ROI was significantly reduced ($p < 0.0001$) in the ipsilateral sciatic nerve milieu in the CXB-NE nanomedicine treated rats at day 12 (Fig. 13f, h) compared to the day 12 vehicle-treated group (Fig. 13f, g). It was observed that the granule number per ROI remains at similar levels in the day 18 vehicle group (Fig. 13f, i) and is measured at similar levels again in the day 18 nanomedicine treated group (Fig. 13f, j), a significant increase ($p < 0.0001$) compared to the day 12 nanomedicine treated rats (Fig. 13f, h). In the ipsilateral DRG, there is no treatment effect influencing extracellular Mcpt1 particles (Fig. 13k), however, there is a significant increase (Fig. 13p, s, t) in both treatment conditions at day 18 compared to day 12 ($p < 0.0001$).

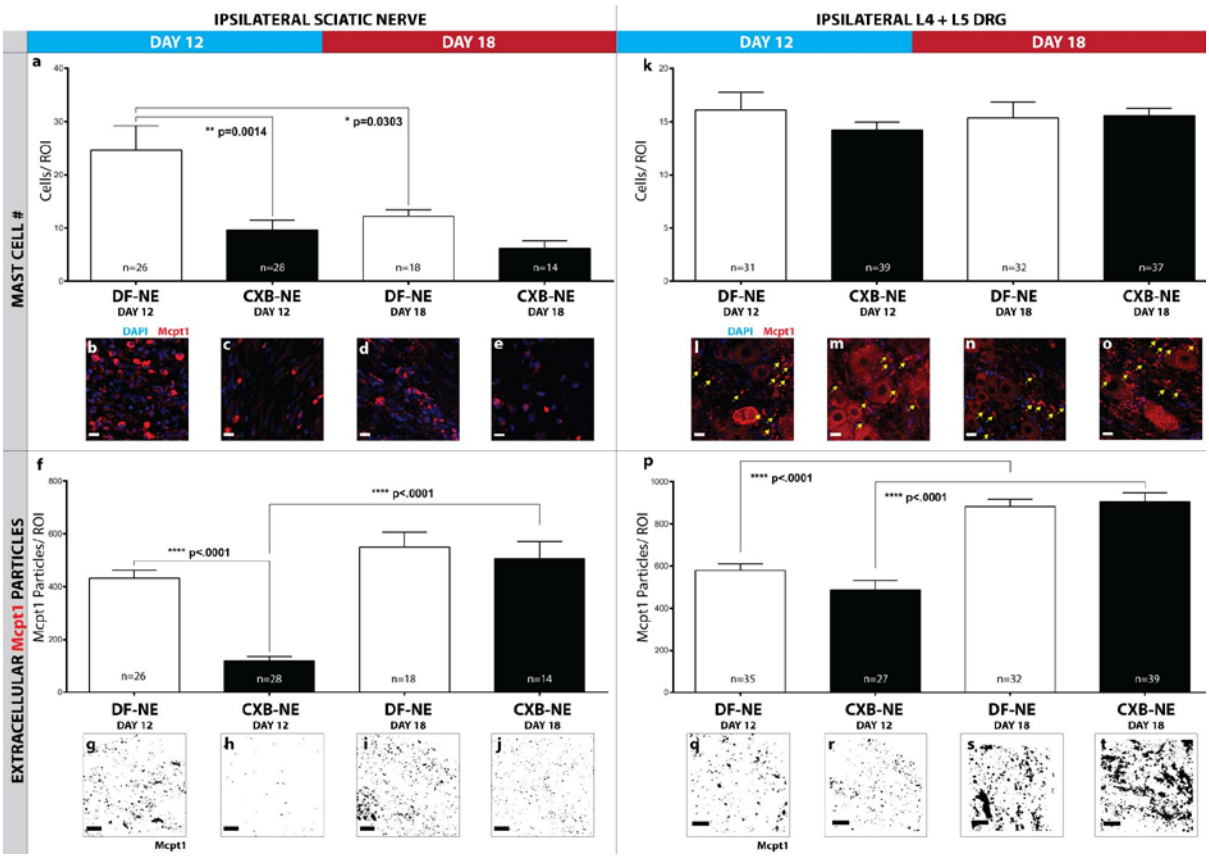

Figure. 13. Mast cell number and extracellular Mcpt1 particles are lowered in ipsilateral sciatic nerve following CXB-NE treatment.

*The number of mast cells and extracellular Mcpt1 particles, both stained with anti-Mcpt1 antibody, are counted for each region of interest on tissue sections at the ipsilateral sciatic nerve of CCI animals at both day 12 and day 18. The mast cell number per ROI decreases significantly (**a**) in the CXB-NE condition (**c**) at day 12 ($p = 0.0014$) compared to the DF-NE condition (**b**). At day 18, both the CXB-NE (**e**) and DF-NE (**d**) conditions have significantly fewer mast cells per ROI compared to the DF-NE condition at day 12. Also notable is that there are significantly less ($p = 0.0303$) mast cells per ROI at day 18 (**d**) in the DF-NE condition compared to day 12 (**b**). There are no significant differences in mast cell counts among treatment groups in the DRG. The representative images--**g**, **h**, **i** and **j**—have been converted to binary images to better show Mcpt1 particles, which are counted by applying a size threshold during analysis. Mcpt1 particles per ROI are significantly reduced ($p < 0.0001$) at the ipsilateral sciatic nerve milieu in the day 12 CXB-NE condition (**h**) compared to the day 12 DF-NE group (**g**). Interestingly, the particle number per ROI remains at similar levels in the day 18 DF-NE group (**i**) and is observed at similar levels again in the day 18 CXB-NE group (**j**), a significant increase ($p < 0.0001$) compared to the day 12 CXB-NE group (**h**). In the DRG, there is no significant difference between treatment conditions in either the day 12 or day 18 groups, however both conditions show a significant increase in Mcpt1 particles at day 18 ($p < 0.0001$). All scale bars are 15 µm. Data is represented as mean ± SEM (n = 3 animals, 14-26 ROI; *p<.05, **p<.01, ****p<.0001,*

one-way ANOVA with Tukey's post hoc test). This figure is reproduced from Saleem et al. Acta Neuropathologica Communications. Volume 7, Article number: 108 (2019). Link: https://actaneurocomms.biomedcentral.com/articles/10.1186/s40478-019-0762-y/figures/7. Muzamil Saleem performed related experiments and produced the figure.

Supplementary figures

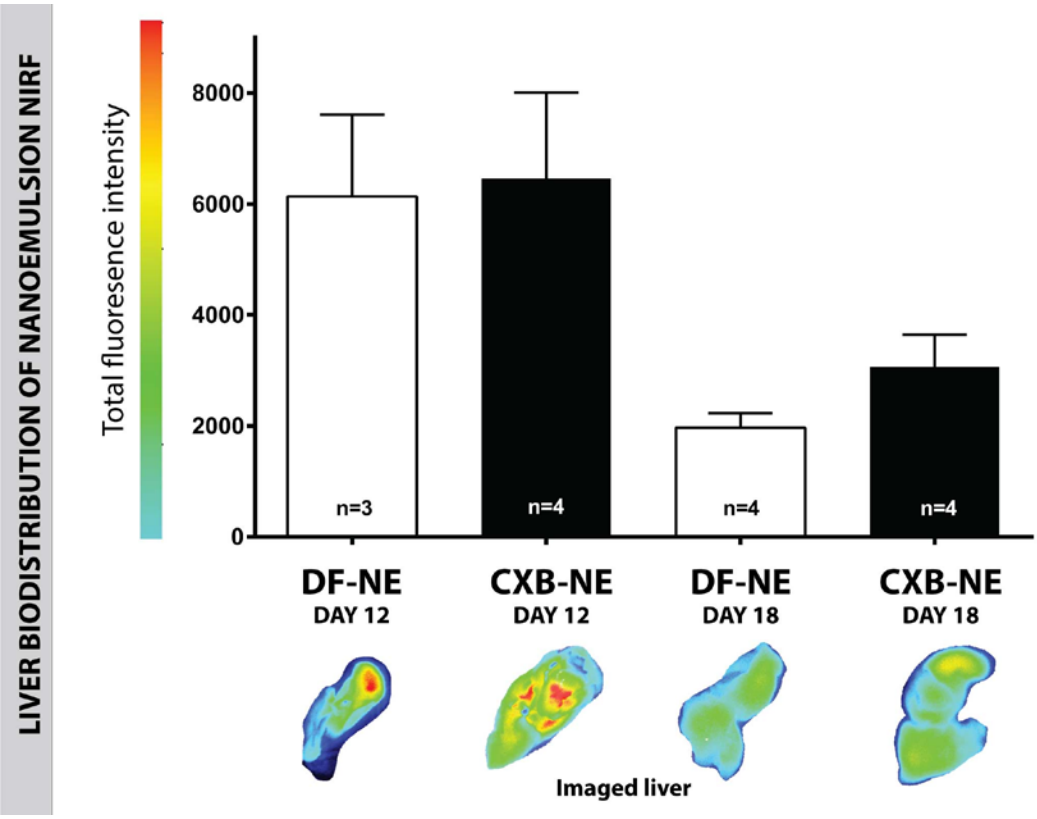

Figure 14. Clearance of NIRF signal from the liver.

Supplementary figure from published paper [87] *(https://static-content.springer.com/esm/art%3A10.1186%2Fs40478-019-0762-y/MediaObjects/40478_2019_762_MOESM1_ESM.pdf).*

Chapter V. Discussion and conclusions

Discussion and conclusion of results presented in chapter III

With the intravenous injection of drug loaded nanoemulsion the animal experiences a significant reduction in mechanical allodynia that persists for at least four days. This single low dose (0.24 mg/kg of celecoxib) represents a reduction of three orders of magnitude in drug needed to achieve relief as compared to a traditionally effective dose of up to 30 mg/kg delivered twice daily for 10 days or more [108,109]. The change in behavior associated with nanoemulsion therapy coincides with a significant reduction in inflammation at the site of injury. This is revealed by the non-invasive in vivo visualization of near infrared fluorescence associated with infiltrating macrophages that carry the nanoemulsion. Post-mortem histological examination of the affected sciatic nerves reveals macrophages infiltration that is reduced with the treatment using drug-loaded nanoemulsion. Furthermore, histological examination reveals a reduction in the relative expression of COX-2 and PGE2 that is evident at the site of injury when the drug-loaded nanoemulsion is present. These data show that low-dose celecoxib incorporated in nanoemulsion and its uptake into activated macrophages responding to chronic constriction injury leads to sustained pain relief. By comparison, nerve blocks that are used extensively for anesthesia and pain relief can involve the local delivery of NSAID solutions via catheter, with varied analgesic duration and efficacy [110,111]. Though rare, nerve blocks can lead to serious complications including nerve injuries and local anesthetic systemic toxicity [112]. Unlike nerve block procedures that deliver drug non-selectively to all cells/tissues at the site of injury, or systemic treatments that deliver drugs throughout the entire body, monocyte targeted nanoemulsions loaded with

COX-2 inhibitors, when administered intravenously, deliver the drug directly to those cells modulating their infiltration patterns and the pro-inflammatory action, which leads to decrease in hypersensitivity and pain-like behavior in rats. Furthermore, the results presented exhibit the therapeutic potential of selective COX-2 inhibitors injected as theranostic nanoemulsion, which may provide an important avenue for targeted delivery of highly insoluble drugs and therapies that may provide an alternative to post-surgical opioids.

Conclusion

The majority of current pain therapies utilize drugs that are broadcast throughout the entire body, but that have a specific effect on discrete areas of either the central nervous system or the peripheral nervous system. To get the medicine at a sufficient concentration where it is needed requires doses that can endanger other tissues and organs where the drug is not needed. We demonstrate that a single low-dose of celecoxib can treat chronic pain for about a week when delivered to macrophages by nanoemulsion. As compared to traditional oral dosing given twice a day every day, the nanoemulsion therapy represents a reduction of the body burden of drug of >2000-fold; a dramatic increase of drug efficacy.

Discussion and conclusion of results presented in chapter IV

Adapted from Saleem et al. *Acta Neuropathologica Communications volume 7, Article number: 108 (2019)*

The studies constituting this thesis [23,87] report that a single low dose of celecoxib delivered to macrophages via nanomedicine leads to a reduction in hypersensitive pain-like behavior, persisting for approximately 6 days. During this state of pain relief, our data reveals that the number of infiltrating macrophages at the site of chronic constriction injury is reduced in the drug-treated condition. We also show a significant reduction in both COX-2 positive macrophages and extracellular PGE2 in the milieu of the nerve injury, when the drug is present. Furthermore, the drug influences a shift in the population of macrophages to the M2 anti-inflammatory state. Finally, we observe that the presence of the drug reduces mast cell activation at the site of injury, indicated by a lower number of mast cells and extracellular Mcpt1—indicative of secreted granules. Our study was designed to investigate the inflammatory neuropathology framed around two time-points—the first, when CXB-NE rats experienced peak relief of neuropathic pain (day 12) and the second, when pain-like behavior had returned to levels similar to DF-NE vehicle-treated rats (day 18).

Theranostic nanomedicine offers multi-day neuropathic pain relief, effectively diagnoses inflammation in-vivo and sheds light on the underlying mechanisms of immune cell pathology

Administering a single low dose of celecoxib (~0.24 mg/kg) to CCI rats via intravenous nanomedicine delivery is effective in reversing pain-like hypersensitivity as reported here and previously [23]. It is well known that NSAIDs like celecoxib have poor efficacy in treating neuropathic pain [113], however this is in the context of non-targeted approaches whereby drugs are delivered either orally or parenterally, and consequently made systemically available. Intrathecal injections also do not meet our design criteria as presented here. In our earlier work and in this study, we demonstrated a dramatic improvement in the efficacy of celecoxib once it is included into a nanoemulsion preparation. The key is that in this paradigm, the COX-2 inhibitor, celecoxib, is directly delivered to the target—the COX-2 enzyme in the monocyte, rather than other cell types and tissues. The nanoemulsion droplets provide an intracellular depo for the drug to successfully inhibit the COX-2 enzyme in these cells. Dr. Janjic has designed this approach as a means of dramatically enhancing the efficacy of COX-2 inhibition in inflammatory diseases such as neuropathic pain. In earlier studies we have demonstrated that targeted COX-2 inhibition by nanoemulsions can produce marked pain relief in a rat model of neuropathic pain [23,57]. This, in our view, promises to be both a safer and more effective strategy than CNS-targeted treatments such as opioids, which are rife for potential abuse and have the potential to result in significant toxicity. Opiate drugs bind to opioid receptors in neurons, and mimic the effects of endogenous opioid ligands [114]—they produce an analgesic effect by inhibiting neurotransmitter release in nociceptive pathways. Whilst originally thought of as acting on opioid receptors on the

plasma membrane of neurons, it has recently been discovered that opioid drugs also act on the membrane of endosomes and structures such as the Golgi apparatus [115], hence distorting the length of receptor activation and signaling. This could potentially explain the undesired effects of opioid drugs. Considering this, it becomes even more prudent to focus pain medication on the underlying cause.

This study demonstrates a peak relief from pain on the third and fourth day after nanomedicine treatment and persists for up to 6 days after the injection (Fig. 8a, b). In addition to the therapeutic utility of the nanomedicine, it exhibits a diagnostic function—able to report on the amount of macrophage infiltration—an indication of the extent of underlying inflammation. The NIRF signal emitted by the nanomedicine is predictably reduced in nanomedicine-treated rats when their right thighs are imaged at day-11 after surgery (Fig. 8c, f). However, when imaged the night before being euthanized at day 18 post-surgery, the NIRF signal is reduced in both the nanomedicine and vehicle-treated groups (Fig. 8c, g, h). This may be due to the turnover of macrophages and the relative clearance of the nanomedicine over time from the body of the rats. Additionally, it is also feasible that the process of wound healing at the surgical incision site has rendered a reduced number of pro-inflammatory macrophages. Also, we show in a biodistribution study that the relative NIRF signal emitted from the liver in both nanomedicine and vehicle-treated rats is reduced at day 18 as compared to day 12 after surgery (Fig. 14), which is suggestive of macrophage clearance from the body. A study investigating the organ-specific fate of macrophage recruitment and refilling found that inflammatory monocytes repopulate the spleen and liver, and not the lung [116]. Biodistribution analysis in the spleen did not show any significant differences of NIRF signal among testing groups or between time-points. This is likely due to the autofluorescence often observed in this organ as a result of it being blood dense.

Interesting to note is that a significantly large population of undifferentiated monocytes—outnumbering the population in the circulation—are stored in the spleen [117], from where they can be quickly deployed to injured tissue.

Macrophage infiltration is reduced in the inflamed sciatic nerve and not the associated L4 and L5 DRG following nanomedicine treatment

An inflammatory response that is localized to the nervous system is termed neuroinflammatory and can be caused by infection, autoimmunity and tissue injury. These insults provide cues that are followed by the initiation of inflammation, which causes plasma extravasation and infiltration of immune cells such as neutrophils, T cells, and monocytes, as well as mobilizing resident macrophages and mast cells [28]. Monocytes and neutrophils are circulating phagocytes that can be signaled during an immune response. Monocytes are especially dynamic because they can be signaled from the blood circulation to infiltrate sites of inflammation and differentiate into macrophages. They are also the most abundant infiltrating immune cell arriving at injured nerve tissue [118]. This blood to tissue migration of the monocyte—as well as its phagocytosis of foreign materials—underpins the design of nanomedicine targeting the inflammation that gives rise to chronic pain. The hypothesis: attenuation of COX-2 activity in these monocytes fated to infiltrate the CCI sciatic nerve using nanomedicine loaded with celecoxib will reduce pain-like hypersensitivity. Reducing COX-2, in turn, reduces the recruitment of additional immune cells and, hence reduces inflammation.

We have previously shown that fewer macrophages infiltrate the injured sciatic nerve at day 12 following nanomedicine treatment [23]. This study sought to report on the extent of infiltration at day 18—a time when pain relief has diminished. Additionally, we aimed to investigate the infiltration of monocytes into the associated L4 and L5 DRG of the sciatic nerve.

We confirm our previous finding that nanomedicine (CXB-NE) treated rats show a reduction in macrophage infiltration at the injured sciatic nerve tissue isolated at day 12 (Fig. 3). There is no effect of treatment at day 18, and additionally, there is no increase in infiltration at day 18; in fact, there is a significant reduction ($p < 0.0001$) in the vehicle-treated group (Fig. 3). It is anticipated that macrophage infiltration does not proceed at a constant rate throughout the inflammatory response and that by day 18, has shifted to a lower turnover rate—a point at which the macrophage population is contributing to both Wallerian degeneration and axonal regeneration [119].

The ipsilateral L4 and L5 DRG neurons associated with the injured sciatic nerve show no reduction in macrophage infiltration following nanomedicine treatment. As reported in a previous study [120], we show that macrophages accumulate over time in the chronic pain-affected DRG—with a significant increase in infiltration evident at day 18 compared to day 12.

The rationale for focusing the present study on monocyte phagocytosis of nanomedicine and migration to the injured sciatic nerve is due to this cell type being the most abundant [118] at sites of tissue injury. Neutrophils are another type of phagocyte that are abundant early at the site of injury or infection [121], however our earlier reports confirm specificity for monocyte uptake of the designed nanomedicine, and the selective inhibition of COX-2 intracellularly using this approach [57]. Numerous studies have also shown preference of nanoemulsion uptake into monocytes compared to other cell types [122–124]. Interestingly, it has recently been shown that

neutrophils are not a phenotypically homogenous population as originally believed, and that like macrophages, possess a phenotypic versatility based on function [125]. It would hence be prudent in the future to design new nanoemulsions specifically targeted to neutrophils in order to study their phagocytic and transport potential in the context of neuroinflammation and pain pathology in the PNS.

Nanomedicine treatment significantly reduces the proportion of COX-2 positive macrophages and extracellular PGE2 at day 12 but not day 18

In the day 12 nanomedicine treatment group, we demonstrate a significant reduction ($p < 0.0001$) in the percentage of COX-2 positive macrophages (Fig. 4), and the quantity ($p = 0.0029$) of extracellular PGE2 (Fig. 4) at the injured sciatic nerve. The percentage of COX-2 positive macrophages at day 18 reverts to a level resembling that in the day 12 vehicle-treated group, whilst extracellular PGE2 levels fall significantly ($p < 0.0001$) in both treatment groups at day 18 (Fig. 4). We focus here on macrophages either being positive or negative for COX-2 and subsequently reporting a percentage that is positive. In terms of PGE2, we shift the focus on extracellular expression; the rationale being that a release of PGE2 from macrophages is a more conclusive measure of a pro-inflammatory state. Additionally, cells that are positive for both COX-2 and nanomedicine are revealed; there is a higher percentage of nanomedicine-positive macrophages (also positive for COX-2) in the day 12 nanomedicine treated group, compared to all other groups. The celecoxib treatment attenuates COX-2 by blocking the protein's activity [107], not destroying COX-2.

Nanomedicine treatment drives macrophages to switch polarity to an anti-inflammatory phenotype

The macrophage is a pleiotropic cell type, that not only promotes inflammation but is also involved in its resolution, as well as tissue repair and remodeling [126–128]. A heterogeneous population of macrophages can switch phenotype to serve these diverse functions; they can acquire pro-inflammatory (termed M1), and anti-inflammatory (termed M2) phenotypes. It was a goal of this study to determine the pro-inflammatory and anti-inflammatory phenotypes of infiltrating macrophages to the site of sciatic nerve injury, and subsequently, determine if the composition of M1 and M2 macrophages changes in response to nanomedicine treatment. A recent proteomic study [5] that proposed cell membrane markers to precisely discriminate M1 and M2 macrophages was consulted in order to co-stain macrophages with an M1 or an M2 marker. The antibody against TNF receptor superfamily member 5 (anti-CD40) is a marker for M1 macrophages, and the antibody against the transferrin receptor (anti-TFRC) is a marker for M2 macrophages [86].

At day 12, there is a significant decrease ($p < .0001$) in the percentage of macrophages positive for the M1 marker following CXB-NE nanomedicine treatment (Fig. 5). Remarkably, the reduction in M1 macrophage percentage persists at day 18 in the nanomedicine group (Fig. 5). In an experiment investigating M2 macrophages at the injured sciatic nerve, nanomedicine treatment resulted in a significantly higher ($p < 0.0001$) percentage of the M2 phenotype at day 12 compared to the vehicle group (Fig. 5). At day 18, the percentage of M2 macrophages in the nanomedicine treatment group decreases significantly ($p < 0.0001$), compared to day 12 (Fig. 5). The increase in M2 macrophages appears to be lower than the

reduction in M1 macrophages and could be explained by the fact that the M2 phenotype is the default state of resident macrophages [84], hence why the differences in the M2 phenotype proportion are not as pronounced as M1.

This result indicates an important shift in macrophage polarity from M1 to M2 in the pool of macrophages at the injured sciatic nerve following nanomedicine treatment. Taken with our findings regarding macrophage COX-2 and external PGE2 expression, the polarity shift indicates that the nanomedicine is attenuating COX-2 activity inside the macrophage, leading to a reduction in extracellular PGE2 and by doing so is switching the macrophage to an anti-inflammatory M2 phenotype. This M2 phenotype is consequently equipped to promote axonal regeneration [119].

Multinucleated giant cells form from M2 macrophages and are observed at day 18, predominantly in the nanomedicine treatment group

We noted the presence of significantly more multinucleated giant cells in the nanomedicine treated rats at day 18. These are formed from the fusion of their M2 polarized macrophage precursors [84,88], and function to more effectively phagocytose relatively large debris from tissues. Significantly more MGCs are observed in the nanomedicine treated group at day 18. Building on the finding that there is a polarity shift towards the M2 phenotype, it can be hypothesized that M2 macrophages have fused into MGCs in order to perform their tissue healing functions in a more efficient manner. This is further evidenced by comparing the nanomedicine NIRF colocalization with M2 macrophages between day 12 and day 18 groups.

There is a significant decrease in nanomedicine-positive M2 macrophages at day 18 in both the DF-NE (Fisher's exact test, $p < 0.0001$) and CXB-NE (Fisher's exact test, $p < 0.0001$) groups. Additionally, the increase in MGCs in the CXB-NE condition at day 18 coincides with a decrease in nanomedicine NIRF positive M2 macrophages (Fisher's exact test, $p = 0.000376$); this suggests that more M2 macrophages have fused to form MGCs in this condition.

The shift in macrophage polarity is associated with a reduction in mast cell activation

Mast cells mature from recruited progenitors released from the bone marrow into the blood circulation [107] and are a key effector cell of the innate immune system. They are involved in the first response to an insult to organs or tissues [129] and influence subsequent inflammatory events—for example, by activating macrophages [130,131]. Factors released when mast cells degranulate can also sensitize nociceptors and lead to increased pain pathogenesis [132]. These can include TNAα [133], IL-1β [134], and tryptase—which interacts with protease-activated receptor 2 (PAR2) on nociceptors [135,136]. This response manifests as the initiation, amplification, and prolonging of inflammation. We report here that the number of mast cells is significantly decreased ($p = 0.0014$) at day 12 in nanomedicine treated rats (Fig. 7). The mast cell number per ROI is not affected by drug treatment at day 18 (10 days after the single injection of nanomedicine). However, the vehicle-treated group reveals significantly fewer ($p = 0.0303$) mast cells at the injured sciatic nerve at day18 compared to day 12 (Fig. 7). Mast cell degranulation in the injured sciatic nerve is significantly lowered at day 12 in the CXB-NE nanomedicine treated rats, indicated by a reduction in extracellular Mcpt1 particles. By day 18, levels of Mcpt1

particles in the nanomedicine treated rats revert to levels resembling the vehicle treatment group at day 12, increasing significantly ($p < 0.00001$). In the DRG, there is no treatment effect either at day 12, or day 18, which could suggest that the mast cells in this location are resident and have not infiltrated from blood-borne progenitors. There is, however, a significant increase ($p < 0.0001$) in mast cell degranulation in ipsilateral DRG in both treatment conditions at day 18, compared to day 12. Much like the increase in macrophage infiltration to the DRG observed at day 18, it is proposed that the increased mast cell degranulation is a result of ongoing neurogenic inflammation conducted from the injured sciatic nerve (Fig. 8).

Based on our data, we have proposed mechanisms for the immune-cell neuropathology underlying the neuropathic pain state, a state where there is pain relief and a final state where there is a return to pain-like behavior (Fig. 8). Taken together, our results suggest a link between the predominant pool of M1 macrophages at the injured sciatic nerve of rats administered with DF-NE vehicle nanomedicine, along with a higher percentage of COX-2 positive macrophages and a higher expression of extracellular PGE2. This inflammatory macrophage phenotype functions as an immune effector system, signaling to other cells—such as resident mast cells—to perpetuate inflammation via their activation, and subsequent degranulation (Fig. 8a). The majority of M1 macrophages are fated to die, terminated by their nitrous oxide production [84], whilst M2 macrophages are involved in resident tissue functions such as repair and regeneration, which conceivably requires them to be alive for longer.

We propose that in the ‘pain relief’ state driven by CXB-NE nanomedicine, the inactivation of COX-2 and reduction in the production and release of PGE2 causes a shift towards an anti-inflammatory M2 macrophage phenotype (Fig. 8b). There is hence a reduction in macrophage crosstalk with mast cells—i.e. they are not activated—resulting in reduced local

inflammation at the ipsilateral sciatic nerve. An effect of reduced inflammation is a lower potential for macrophage and mast cell infiltration, a result which we observe.

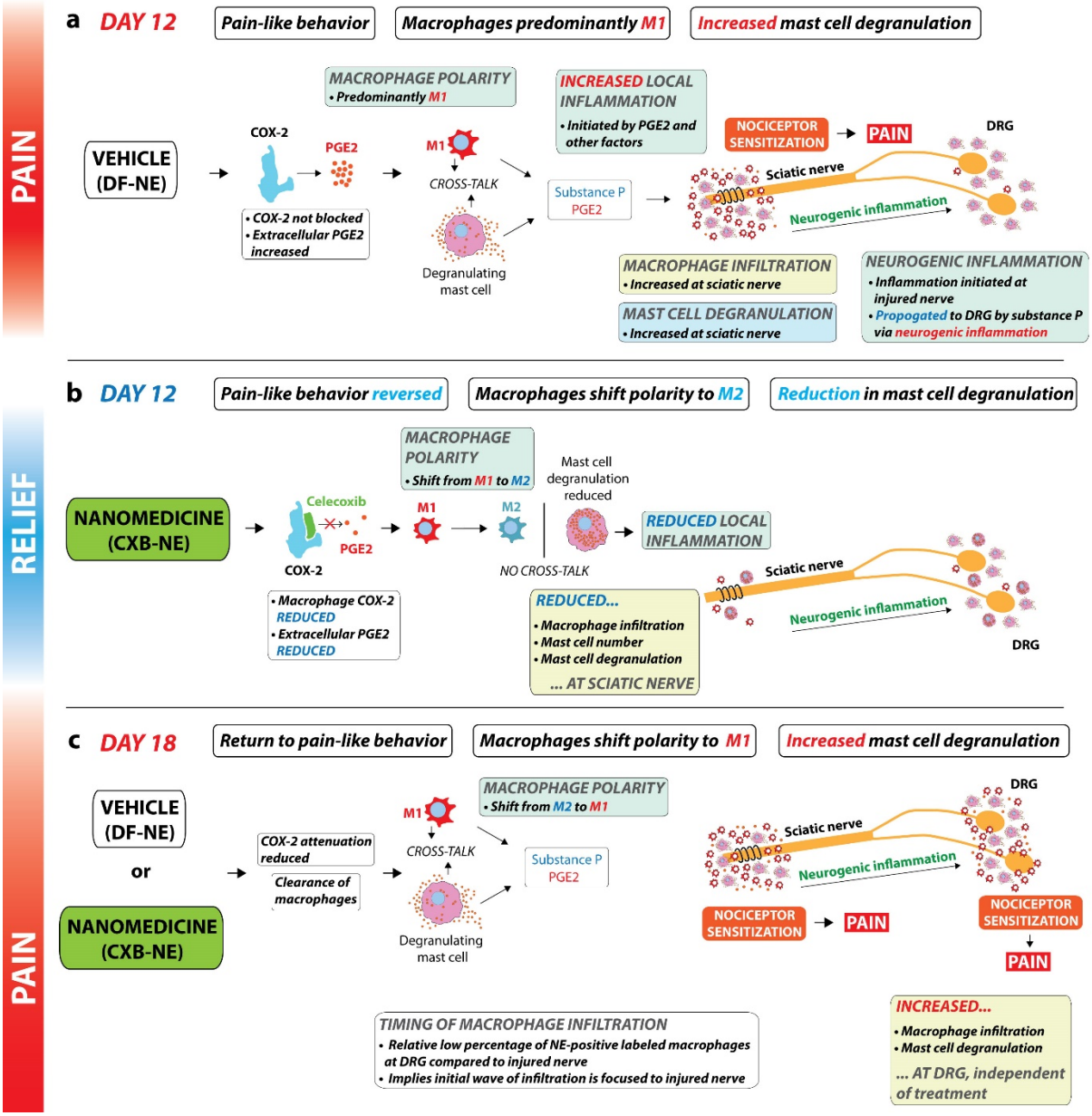

Figure 15. Proposed mechanisms underlying reversal of pain-like behavior at day 12 and diminished relief at day 18.

*In a neuropathic pain state, CCI rats administered with DF-NE vehicle nanomedicine exhibit pain-like behavior (**a**). This is proposed to be centrally driven by the expression of functional COX-2 in circulating monocytes and increased release of PGE2. The polarity of macrophages at the injured sciatic nerve is predominantly the M1 pro-inflammatory phenotype. This influences*

*crosstalk with mast cells, and their subsequent activation. With both immune effector cell types in an activated state, local inflammation is increased, resulting in a subsequent increase in macrophage infiltration. Inflammation at the ipsilateral DRG is transmitted through the afferent nociceptors from the injured sciatic nerve via neurogenic inflammation. In nanomedicine treated rats in the day 12 group (**b**), there is a reduction in COX-2 positive macrophages and extracellular PGE2 via the action of nanomedicine-delivered celecoxib. There is both a reduction in macrophage infiltration to the injured sciatic nerve and a shift of macrophage phenotype from pro-inflammatory (M1) to anti-inflammatory (M2). There is no nanomedicine treatment effect of macrophage infiltration to the DRG at day 12. M2 macrophages function to repair and regenerate the injured tissue and do not crosstalk with resident mast cells. There is a return to pain-like behavior at day 18 (**c**) in both nanomedicine and vehicle-treated groups. Macrophage infiltration to the injured sciatic nerve at day 18 is relatively low in both treatment groups—similar to levels observed in the day 12 nanomedicine-treated group. Macrophage infiltration to the DRG is increased at day 18, compared to day 12 and there are no significant differences between treatment groups. It is proposed that inflammation is initiated at the injured nerve and propagated to the associated L4 and L5 DRG via neurogenic inflammation. This drives recruitment of macrophages—as well as influencing further mast cell degranulation—and together provides the inflammatory input to sensitize nociceptors, resulting in an increase in pain-like behavior. The relatively low percentage of nanomedicine -positive macrophages at the DRG compared to the injured nerve suggests that the initial wave of macrophage infiltration is focused to the injured nerve. This figure is reproduced from Saleem et al. Acta Neuropathologica Communications. Volume 7, Article number: 108 (2019). Link: https://actaneurocomms.biomedcentral.com/articles/10.1186/s40478-019-0762-y/figures/8. Muzamil Saleem performed related experiments and produced the figure.*

The proposed mechanism underlying the return to pain-like behavior at day 18

Our data indicate that the increase in macrophage infiltration to the L4 and L5 DRG associated with the injured nerve of CCI animals, as well as the increase in mast cell degranulation, may be driving the return to pain-like behavior observed at day 18 (Fig. 8c). It has been demonstrated that the tactile allodynia underpinning pain-like behavior is dependent on peripheral macrophages [137]. In addition to the immune cell infiltration to the site of nerve injury,

it has been shown that macrophages are also abundant at the DRG [138,139], and are observed to circle the cell bodies of injured A-fiber sensory neurons [140]. By observing the NIRF labeling of macrophages with nanomedicine, our data give us clues as to the relative timing of macrophage infiltration to the injured sciatic nerve and its associated DRG. It was observed that a lower percentage of macrophages infiltrating the DRG were nanomedicine positive—in both treatment groups—compared to the sciatic nerve, which suggests that the initial wave of infiltration is focused to the site of CCI surgery. It is thought that this initial wave of immune cell migration is initiating inflammation at the sciatic nerve and sensitizing its nociceptors. It is possible that the neuroinflammatory state at the DRG—characterized by the increase in macrophage infiltration—is propagated from this sciatic nerve sensitization via a process of neurogenic inflammation [141]—a process whereby afferent neurons release inflammatory mediators such as Substance P and Calcitonin Gene-related Peptide (CGRP). Substance P, a neuropeptide that perpetuates the conduction of neurogenic inflammation, is also released by both macrophages and mast cells and acts on peripheral nociceptors [82] to further drive inflammation in the afferent direction. Inflammation is consequently perpetuated to the DRG from the peripheral nerve. Additionally, we have previously shown an elevated DRG expression of the TRPV1 receptor central in pain transmission that is also labelled with a retrograde dye applied to the footpad [24], confirming the path of neurogenic inflammation.

Conclusions

Our results suggest that the central driver of nanomedicine chronic pain relief is a shift towards an M2 macrophage phenotype, via attenuation of intracellular macrophage COX-2. M2 macrophages at the injured sciatic nerve fuse to form MGCs, and then tackle the phagocytosis of large debris; namely dead distal nerve fibers via Wallerian degeneration. This population of anti-inflammatory macrophages is also contributing to axonal nerve regeneration. The shift towards an anti-inflammatory milieu at the injured nerve is thought to result in less M1 macrophage recruitment—reducing inflammation, and subsequent neuropathic pain. In the absence of the CXB-NE COX-2 targeted nanomedicine, it is posited that the resulting pro-inflammatory environment at the injured nerve consists in part of M1 macrophages signaling the upregulation and activation of mast cells—further perpetuating neuroinflammation, which contributes to a neurophysiological signal propagated towards the CNS, via neurogenic inflammation. Thus, this inflammation is interpreted as hypersensitivity as evident in pain-like behavior. Our data also points to a possible mechanism underlying the return to pain-like behavior--it becomes clear that the locale of the associated DRG is not influenced significantly by the day-8 macrophage-targeted treatment. This suggests that in the absence of therapeutic influence, the neuroinflammatory milieu of increasing macrophage infiltration in to the DRG, and increased mast cell degranulation is sensitizing nociceptors, causing a return to neuropathic pain. Taken together, this report suggests for the first time that a pain nanomedicine phagocytosed by circulating monocytes that infiltrate the site of injury shifts their polarity via COX-2 attenuation, reduced PGE2 synthesis, and in turn, influence a reduction in mast cell activation—resulting in multi-day neuropathic pain relief.

Moreover, our investigation suggests that while immune neuropathological events at the site of the injured nerve can be successfully reversed with targeted immune-cell therapy, the spatial signature of neuroinflammation towards the CNS must also be concurrently addressed. Specifically, while the immune cell milieu at the injured nerve is resolving inflammation via nanomedicine targeted macrophages, the initial waves of neurogenic inflammation initiated and propagated in the afferent direction are unresolved. Hence, this results in the latent inflammation we reveal at day 18. Further, the utility of a nanomedicine targeted to immune cell pathology offers a new research paradigm that can yield dynamic investigation and tracking of temporal patterns of cell infiltration, phenotypic change, and alterations in gene expression.

The utility of imaging inflammation using nanoemulsion ultimately revealed that while there was a favorable reversal of inflammation at the injured sciatic nerve, there was a rising inflammatory milieu at the DRG associated with the sciatic nerve. This highlights the need to address multiple points of the pain circuit: the initial site of injury or dysfunction, and also the affected neuronal cells bodies in the DRG to bias their activity before hypersensitivity signals enter the CNS.

Future directions

The scope of future studies progressing from this thesis is an exciting prospect. Having elucidated some aspects of the immune pathology of macrophages and mast cells in a pain vs.

non-pain state following nanomedicine treatment, there are further experiments that would be prudent.

Repeat studies in female rats

The foremost study that ought to follow is a replication of the experiments described in this thesis, utilizing female rats. It is becoming increasingly clear in the pain research field that there are fundamental sex differences in both the underlying biological mechanisms [142,143]— particularly with respect to immune cells [144,145] and hormones [146,147]--, as well as the cognitive processing of pain by females. Additionally, a recent transcriptome analysis of the DRG in a neuropathic pain state reveals sex differences in the expression of genes related to the immune response and neuronal plasticity [148]. Replicating this work in female rats would elucidate not only possible differences in the pain-like behavior resulting from CCI, but also differences in pain-relief, as well as the underlying neuroinflammatory mechanisms.

Further validation of CD40 and TFRC

The CD40 and TFRC antibodies utilized to discriminate M1 and M2 macrophages respectively were chosen based on a rigorous proteomic study carried out on cultured monocytes, activated to become M1 or M2 macrophages by interferon-gamma/ lipopolysaccharide (LPS) or IL-4 respectively [149]. Additionally, it would be useful as a future experiment to first replicate this in cell culture, and validate further by both IHC and western blotting, with the addition of purified CD40 and TFRC protein as a positive control.

Further DRG studies

The DRG associated with the sciatic nerve were revealed to have a pain neuropathology distinct from the site of injury. It would be interesting to explore all of the DRG in the vertebral column—namely those not associated with the sciatic nerve, in order to see if inflammation is signaled in a ventrorostral manner. In addition, it would be useful to understand the status of inflammation along the whole length of the afferent sciatic nerve; and also, to understand the temporal nature of neurogenic inflammation (via substance P and CGRP analysis). The DRG are housed by a vast glial network of satellite glial cells. An exploration of these satellite cells would be useful in a further study. In particular, to find out if and when satellite cells are being activated, whether there is crosstalk with immune cells, and whether the satellite cell activity (if there is any) precludes that of the surrounding, infiltrating immune cells.

Characterizing the CCI model in further detail

The CCI animals administered with DF-NE—the control treatment—developed pain-like behavior that was measurable using the manual von Frey up-down method from approximately day 6 following surgery (Fig. 8a). The 50% paw withdrawal threshold lowers progressively and reaches a maximum at approximately day 11 following surgery, at which point pain-like behavior plateaus at a maximum until the animals are sacrificed on day 18. It would be prudent to firstly extend the experiment to investigate exactly how long this maximum level of pain-like behavior persists. This would elucidate the extent of the pain-like behavior in more detail on a temporal level. Secondly, the investigation would be developed to obtain a snapshot of the inflammatory milieu at each day (or each day that behavior is performed). Specifically, the IHC

experiments performed on the sciatic nerve and DRG would be repeated on each day. Together, this would resolve the pain in terms of being acute, chronic—and further—if there is a point at which pain might transition from acute to chronic, informed by the underlying neuropathology.

Characterizing the involvement of other immune cells

As a follow-up to this characterization of the CCI model, it would be interesting to characterize the involvement of other infiltrating immune cells, particularly other phagocytes such as neutrophils and dendritic cells. We would seek to explore not only in how their abundance changes in the conditions investigated in this thesis, but also in terms of whether they are phagocytosing nanomedicine. This tissue analysis at daily time-points would provide a resolution of the temporal immune cascade in neuropathic pain, and how it is affected by targeted nanomedicine therapy.

Investigating additional treatment regimens

Further, nanomedicine treatment at a varying time-points (engineered with different fluorescent markers to differentiate each treatment) would elucidate precisely what effect the timing—as well as varying drug content—is having on the immune neuropathology and pain-like behavior.

As revealed by this work, a future therapeutic challenge will be to personalize nanomedicine treatment to target not only the site of injury, but the associated DRG. The mode

in which this is achieved is unclear. It may be that modulation of the DRG is performed with the use of a locally administered topical—or intrathecal hydrogel.

Investigating the effect of nanoemulsion on normal immune health

It will be useful to investigate the effect of nanoemulsion treatment on normal immune health. Specifically, asking the question of whether attenuating COX-2 in macrophages could compromise the immune system and make it susceptible to infectious disease. In its simplest form, this could be accomplished by performing a measure of macrophage number in tissue and plasma—comparing nanoemulsion treated animals to untreated animals. Additional measures of immune health could also be measured in blood, such as complement levels, immunoglobulin levels, T cell counts and white blood cell counts.

Utilizing single-cell approaches

Furthermore, new technologies to analyze individual immune cell receptor profiles are being developed, such as an approach that combines flow cytometry with mass spectrometry, using metal-conjugated antibodies [150]. Termed ‘CyTOF, it is possible to assay approximately 50 markers at once. This type of single cell technology, in addition to sequencing methodologies that provide snapshots of the transcriptome, would be a very powerful approach in characterizing the cellular fate of discreet populations of immune cells at the affected area and the associated DRG. In addition, there is a potential to use the NIRF labelling of cells in a flow cytometry

paradigm, to sort monocytes with and without the dye at the site of injury, followed by RNAseq to elucidate the specific cellular transcriptome underlying macrophage polarity.

Appendix 1:

Supplementary data

Biodistribution of nanoemulsion

The biodistribution of nanoemulsion was detected by measuring the NIRF signal accumulated at the right sciatic, left sciatic, right L4 and L5 DRG, left L4 and L5 DRG, liver and spleen of CCI rats administered with DF-NE, CXB-NE—and sham rats administered with DF-NE. Nanoemulsion was injected on day-8 post-surgery and tissue was harvested on day 12 following surgery as described in chapter 2: materials and methods. Two types of NIR scanner were utilized. The LicOR Odyssey imager (Supplementary Fig. 1) was used to measure fluorescence in sciatic nerve and DRG tissue, with the rationale being that DRG tissue was small and may be better suited to imaging on a flatbed scanner. The fluorescence intensity was normalized to the weight of the tissue. The results from data accumulated from the LicOR odyssey scanner consist of a small sample size, and therefore are not suitable to infer significant findings—however, there is a trend of lower fluorescence in all conditions in the left sciatic compared to the right sciatic (supplementary Fig. 1a, b). Both the right and left L4 and L5 DRG appear to show similar levels of fluorescence across all conditions (supplementary Fig. 1c, d).

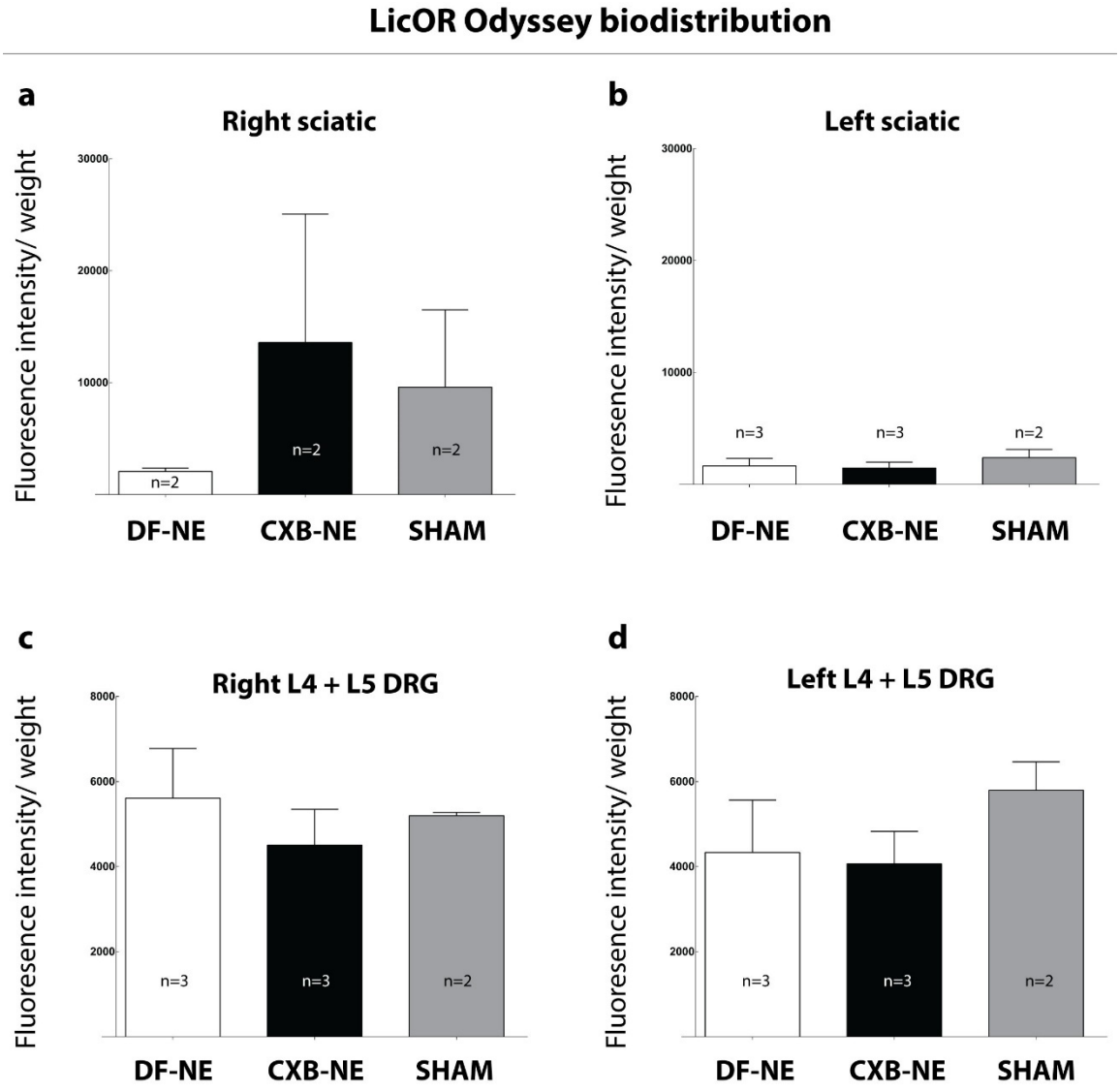

Supplementary Figure 1. Biodistribution of nanoemulsion measured using LicOR Odyssey NIR scanner.

The NIRF signal emanating from accumulated nanoemulsion at the right sciatic, left sciatic, right L4 and L5 DRG, and left L4 and L5 DRG was measured in a LicOR Odyssey flatbed NIR scanner. Significant results cannot be inferred due to a relatively small sample size, however there is an observed trend of lower fluorescence intensity/ tissue weight in the left sciatic nerve compared to the right sciatic nerve. There does not appear to be any differences in fluorescence intensity/ tissue weight among all conditions in the right and left L4 and L5 DRG.

The LicOR Pearl NIR scanner was utilized to measure biodistribution of nanoemulsion *in-vivo* as previously described in this thesis. The manufacturers also recommend this instrument for the use of *ex-vivo* organ biodistribution studies. The fluorescence intensity/ area of nanoemulsion NIRF signal was measured for the right sciatic, left sciatic, liver and spleen of CCI animals administered with DF-NE and CXB-NE and sham animals administered with DF-NE. In this study, biodistribution data was generated from day 12 and day 18 tissue. Similar to the biodistribution data generated from the LicOR Odyssey NIR scanner, the data from the LiCOR Pearl imager showed lower levels of NIRF signal in the left sciatic nerve compared to the right. At the right sciatic nerve, the fluorescence intensity/ area trended at higher levels compared to the sham animals administered with DF-NE. There was no significant difference in NIRF levels between CCI animals treated with DF-NE and those treated with CXB-NE. There was also no significant difference observed between day 12 and day 18 groups, however there was a trend of higher NIRF levels in day 18 sciatic nerve tissue. In liver tissue, NIRF levels were not significantly different between conditions, however there was a trend of lower levels in day 18 tissue—and significantly lower levels in CCI animals administered with CXB-NE ($p=.0200$, one-way ANOVA) and sham animals administered with DF-NE ($p=.0428$, one-way ANOVA). In the spleen tissue, there were no significant differences in NIRF levels between treatment or time conditions.

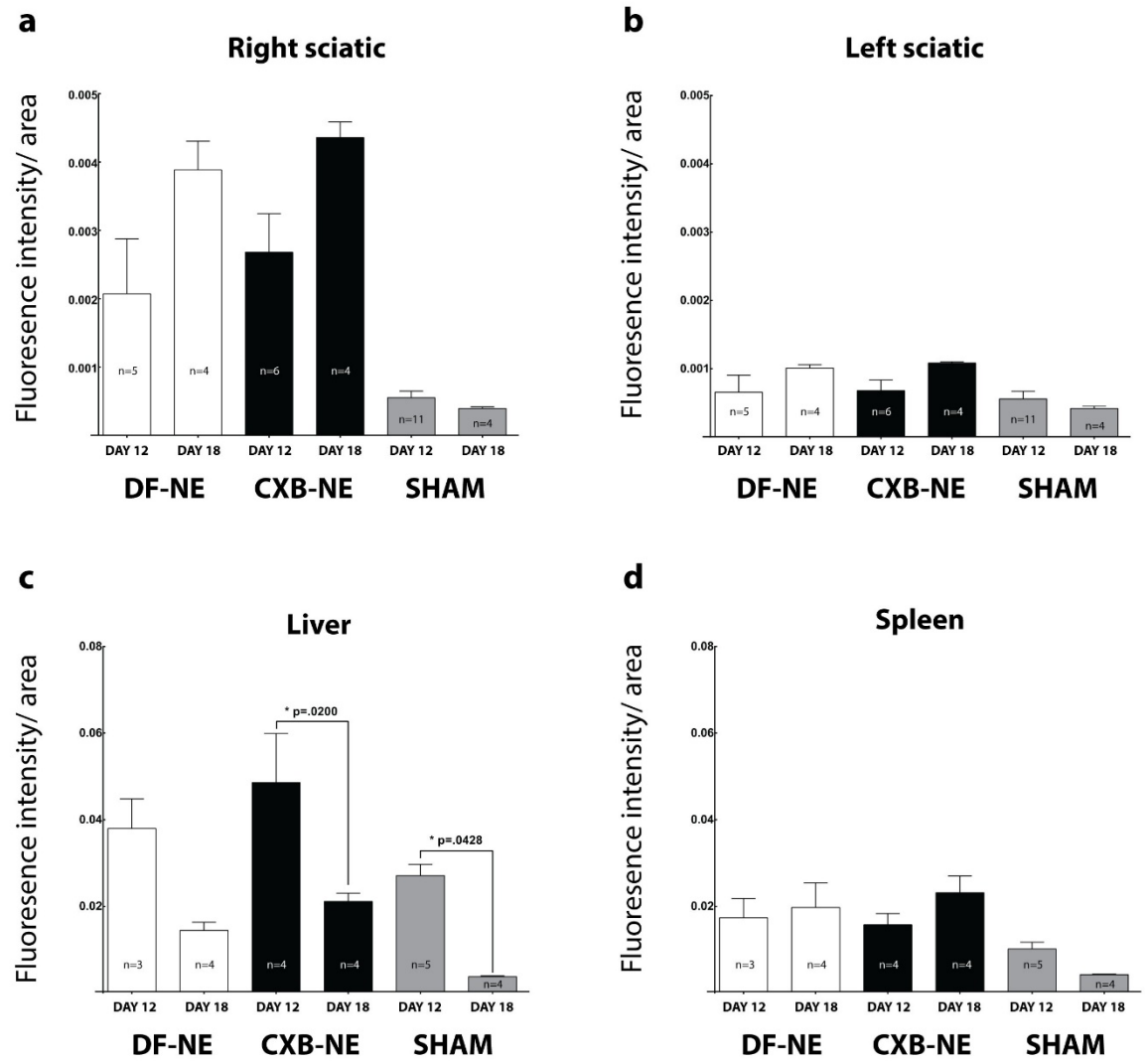

Supplementary Figure 2. Biodistribution of nanoemulsion measured using LicOR Pearl NIR scanner.

NIRF levels were measured in right sciatic nerve, left sciatic nerve, liver and spleen tissue of CCI animals administered with DF-NE, CCI animals administered with CXB-NE and sham animals administered with DF-NE. NIRF levels were lower in the left sciatic nerve compared to the right—however there was no significant difference in NIRF signal observed in day 12 tissue compared to day 18. In liver tissue, there was no significant difference in NIRF signal between treatment groups, however a significantly lower NIRF signal was observed at day 18 compared to day 12 tissue in the CCI animals administered with CXB-NE (p = 0.0200, one-way ANOVA with Tukey's multiple comparisons test) and sham animals administered with DF-NE (p = 0.0428, one-way ANOVA with Tukey's multiple comparisons test). There was a similar—albeit not significant—trend observed in CCI animals administered with DF-NE. In spleen tissue, there

was no significant differences in NIRF signal observed between treatment conditions, or time points.

Macrophage Caspase-1

Caspase-1 is central in the NLR family, pyrin domain-containing 3 (NLRP3) inflammasome—a multi-protein complex-- found inside immune cells such as macrophages. The NLRP3 inflammasome triggers the activation of caspase-1 [151], which promotes the release of the IL-1β and Il-18 cytokines—the latter being a central mediator of neuropathic pain [25]. Additionally, and in the context of this thesis, there is evidence that COX-2 is involved in the regulation of the NLRP3 inflammasome, and that celecoxib treatment was able to attenuate levels of IL-1β and caspase-1 [152]. A pilot study was performed investigating the macrophage expression of caspase-1 in CCI animals administered with DF-NE and CXB-NE. Following sacrifice at day 12, tissue was processed as described in chapter 2. It was observed that macrophage expressed caspase-1 is significantly reduced (supplementary Fig. 3) in CCI animals treated with CXB-NE ($p < 0.0001$, t-test).

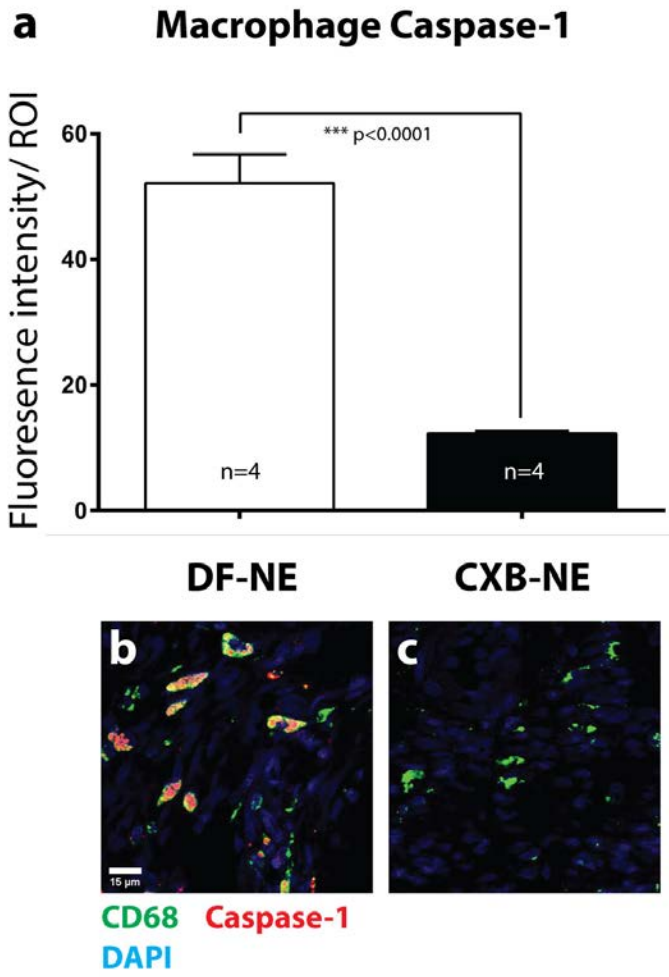

Supplementary Figure 3. Macrophage-expressed caspase-1 is reduced following CXB-NE treatment.

Levels of macrophage caspase-1 are reduced significantly ($p < 0.0001$, t-test) in CCI animals treated with CXB-NE compared to CCI animals treated with DF-NE.

Autofluorescence in DRG cells

Throughout the investigations comprising this thesis, there was a fluorescent signal observed in the 640 nm excitation channel inside the cell bodies of the DRG. It was hypothesized that this could be nanoemulsion droplets, however there were no characteristic black spots observed in the DIC channel, that would indicate nanoparticles. Moreover, the intensity of the signal was measured between groups, and no significant differences were observed. It was hence hypothesized that this was an auto-fluorescent signal emanating from lipofuscin pigment, commonly observed in nerve cells [152]. In an effort to rule out the possibility of this fluorescence arising from nanoparticles, DRG tissue from naïve animals--that had not been treated or had surgery performed on them—was analyzed. An auto-fluorescent signal was observed in the 640 nm channel, confirming that this was not due to nanoparticle NIRF signal (supplementary figure 4).

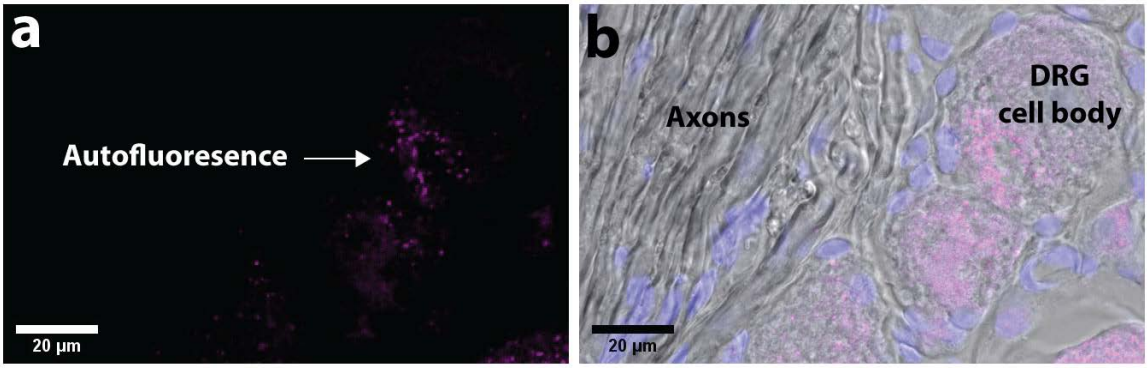

Supplementary Figure 4. Autufluoresence observed in DRG cell bodies.

Shown here is autofluorescence in the DRG of naïve rats that did not receive nanomedicine treatment, nor CCI or sham surgery. 640 nm excitation channel.

Video 1: M2 macrophages fused into a multinucleated giant cell

DOI link to video: https://doi.org/10.6084/m9.figshare.8142950.v1

Video 2: Nanoemulsion droplets inside macrophages

DOI link to video: https://doi.org/10.6084/m9.figshare.8142962.v1

Appendix 2:

Associated datasets and detailed statistical outputs

The datasets generated and/or analyzed during the current study are available in the Figshare repository, [https://figshare.com/projects/Nanomedicine-driven_neuropathic_pain_relief_in_a_rat_model_is_associated_with_macrophage_polarity_and_mast_cell_activation/63785]. The datasets also contain full, detailed outputs of all statistical tests performed.

References

1. National Institue of Health. NIH Fact Sheets - Pain Management. U.S Department of Health & Human Services. https://report.nih.gov/nihfactsheets/viewfactsheet.aspx?csid=57. Published 2018. Accessed October 16, 2019.

2. Gaskin DJ, Richard P. The Economic Costs of Pain in the United States. *J Pain*. 2012;13(8):715-724. doi:http://dx.doi.org/10.1016/j.jpain.2012.03.009

3. Han X, Shotwell M, McQueen K, Stabile V, Thomas S, Jackson T. A Systematic Review and Meta-Analysis of the Global Burden of Chronic Pain Without Clear Etiology in Low- and Middle-Income Countries. *Anesth Analg*. 2016;123(3):739-748. doi:10.1213/ane.0000000000001389

4. Price TJ, Gold MS. From Mechanism to Cure: Renewing the Goal to Eliminate the Disease of Pain. *Pain Med*. 2017;19(8):1525-1549. doi:10.1093/pm/pnx108

5. GBD 2017 Disease and Injury Incidence and Prevalence Collaborators SL, Abate D, Abate KH, et al. Global, regional, and national incidence, prevalence, and years lived with disability for 354 diseases and injuries for 195 countries and territories, 1990-2017: a systematic analysis for the Global Burden of Disease Study 2017. *Lancet (London, England)*. 2018;392(10159):1789-1858. doi:10.1016/S0140-6736(18)32279-7

6. Coull JAM, Beggs S, Boudreau D, et al. BDNF from microglia causes the shift in neuronal anion gradient underlying neuropathic pain. *Nature*. 2005;438(7070):1017-1021. doi:10.1038/nature04223

7. Basbaum AI, Bautista DM, Scherrer G, Julius D. Cellular and Molecular Mechanisms of Pain. *Cell*. 2009;139(2):267-284. doi:10.1016/J.CELL.2009.09.028

8. Gold MS, Gebhart GF. Nociceptor sensitization in pain pathogenesis. *Nat Med*. 2010;16(11):1248-1257. doi:10.1038/nm.2235

9. Reichling DB, Levine JD. Critical role of nociceptor plasticity in chronic pain. *Trends Neurosci*. 2009;32(12):611-618. doi:10.1016/j.tins.2009.07.007

10. Woolf CJ, Salter MW. Neuronal plasticity: Increasing the gain in pain. *Science (80-).* 2000;288(5472):1765-1768. doi:10.1126/science.288.5472.1765

11. Ji R-R, Xu Z-Z, Gao Y-J. Emerging targets in neuroinflammation-driven chronic pain. *Nat Rev Drug Discov*. 2014;13(7):533-548. doi:10.1038/nrd4334

12. Vane JR. Inhibition of prostaglandin synthesis as a mechanism of action for aspirin-like drugs. *Nat New Biol*. 1971;231:232-235. doi:10.1038/newbio231232a0

13. Kujubu DA, Fletcher BS, Varnum BC, Lim RW, Herschman HR. TIS10, a phorbol ester tumor promoter-inducible mRNA from Swiss 3T3 cells, encodes a novel prostaglandin synthase/cyclooxygenase homologue. *J Biol Chem*. 1991;266(20):12866-12872. http://www.ncbi.nlm.nih.gov/pubmed/1712772. Accessed March 1, 2019.

14. Fu JY, Masferrer JL, Seibert K, Raz A, Needleman P. The induction and suppression of prostaglandin H2 synthase (cyclooxygenase) in human monocytes. *J Biol Chem*. 1990;265(28):16737-16740. http://www.ncbi.nlm.nih.gov/pubmed/2120205. Accessed March 1, 2019.

15. FitzGerald GA, Patrono C. The Coxibs, Selective Inhibitors of Cyclooxygenase-2. Wood AJJ, ed. *N Engl J Med*. 2002;345(6):433-442. doi:10.1056/nejm200108093450607

16. Nandakishore R, Yalavarthi P, Kiran Y, Rajapranathi M. Selective Cyclooxygenase Inhibitors: Current Status. *Curr Drug Discov Technol*. 2014;11(2):127-132. doi:10.2174/15701638111666140127123717

17. Ghanem CI, Pérez MJ, Manautou JE, Mottino AD. Acetaminophen from liver to brain: New insights into drug pharmacological action and toxicity. *Pharmacol Res*. 2016;109:119-131. doi:10.1016/j.phrs.2016.02.020

18. Ghanem CI, Rudraiah S, Bataille AM, Vigo MB, Goedken MJ, Manautou JE. Role of nuclear factor-erythroid 2-related factor 2 (Nrf2) in the transcriptional regulation of brain ABC transporters during acute acetaminophen (APAP) intoxication in mice. *Biochem Pharmacol*. 2015;94(3):203-211. doi:10.1016/j.bcp.2015.01.013

19. Roberts E, Nunes VD, Buckner S, et al. Paracetamol: Not as safe as we thought? A systematic literature review of observational studies. *Ann Rheum Dis*. 2016;75(3):552-559. doi:10.1136/annrheumdis-2014-206914

20. Jüni P, Nartey L, Reichenbach S, Sterchi R, Dieppe PA, Egger PM. Risk of cardiovascular events and rofecoxib: Cumulative meta-analysis. *Lancet*. 2004;364(9450):2021-2029. doi:10.1016/S0140-6736(04)17514-4

21. Centers for Disease Control and Prevention. *Understanding the Epidemic | Drug Overdose | CDC Injury Center*.; 2018. https://www.cdc.gov/drugoverdose/epidemic/index.html.

22. Bennett GJ, Xie YK. A peripheral mononeuropathy in rat that produces disorders of pain sensation like those seen in man. *Pain*. 1988;33(1):87-107. doi:10.1016/0304-3959(88)90209-6

23. Janjic JM, Vasudeva K, Saleem M, et al. Low-dose NSAIDs reduce pain via macrophage targeted nanoemulsion delivery to neuroinflammation of the sciatic nerve in rat. *J Neuroimmunol*. 2018;318:72-79. doi:10.1016/j.jneuroim.2018.02.010

24. Vasudeva K, Andersen K, Zeyzus-Johns B, et al. Imaging neuroinflammation in vivo in a neuropathic pain rat model with near-infrared fluorescence and (1)(9)F magnetic resonance. *PLoS One*. 2014;9(2):e90589. doi:10.1371/journal.pone.0090589

25. Vasudeva K, Vodovotz Y, Azhar N, Barclay D, Janjic JM, Pollock JA. In vivo and systems biology studies implicate IL-18 as a central mediator in chronic pain. *J Neuroimmunol*. 2015;283:43-49. doi:10.1016/j.jneuroim.2015.04.012

26. Gold MS, Gebhart GF. Nociceptor sensitization in pain pathogenesis. *Nat Med*. 2010;16(11):1248-1257. doi:10.1038/nm.2235

27. Murray PJ, Wynn TA. Protective and pathogenic functions of macrophage subsets. *Nat Rev Immunol*. 2011;11(11):723-737. doi:10.1038/nri3073

28. Ji RR, Xu ZZ, Gao YJ. Emerging targets in neuroinflammation-driven chronic pain. *Nat Rev Drug Discov*. 2014;13(7):533-548. doi:10.1038/nrd4334

29. Waters H. New $10 million X Prize launched for tricorder-style medical device. *Nat Med*. 2011;17(7):754-754. doi:10.1038/nm0711-754a

30. Finch G, Wolfgang M, Youssoufian H, et al. Nanomedicines: From Bench to Bedside and Beyond. *AAPS J*. 2016;18(6):1373-1378. doi:10.1208/s12248-016-9961-7

31. D'Mello SR, Chen M-L, Lee SL, Cruz CN, Tyner KM, Kapoor M. The evolving landscape of drug products containing nanomaterials in the United States. *Nat Nanotechnol*. 2017;12(6):523-529. doi:10.1038/nnano.2017.67

32. Prabhakar U, Maeda H, K. Jain R, et al. Challenges and key considerations of the enhanced permeability and retention effect for nanomedicine drug delivery in oncology. *Cancer Res*. 2013;73(8):2412-2417. doi:10.1158/0008-5472.CAN-12-4561

33. Torchilin V. Tumor delivery of macromolecular drugs based on the EPR effect. *Adv Drug Deliv Rev*. 2011;63(3):131-135. doi:10.1016/j.addr.2010.03.011

34. Barenholz Y. Doxil® - The first FDA-approved nano-drug: Lessons learned. *J Control Release*. 2012;160(2):117-134. doi:10.1016/j.jconrel.2012.03.020

35. Leroueil PR, Hong S, Mecke A, Baker JR, Orr BG, Holl MMB. Nanoparticle interaction with biological membranes: Does nanotechnology present a janus face? *Acc Chem Res*. 2007;40(5):335-342. doi:10.1021/ar600012y

36. Janjic JM, Srinivas M, Kadayakkara DK, Ahrens ET. Self-delivering nanoemulsions for dual fluorine-19 MRI and fluorescence detection. *J Am Chem Soc*. 2008;130(9):2832-2841. doi:10.1021/ja077388j

37. Patel SK, Janjic JM. Macrophage targeted theranostics as personalized nanomedicine strategies for inflammatory diseases. *Theranostics*. 2015;5(2):150-172. doi:10.7150/thno.9476

38. Herneisey M, Williams J, Mirtic J, et al. Development and characterization of resveratrol nanoemulsions carrying dual-imaging agents. *Ther Deliv*. 2016;7(12):795-808. doi:10.4155/tde-2016-0050

39. Wolfram J, Zhu M, Yang Y, et al. Safety of Nanoparticles in Medicine. *Curr Drug Targets*. 2015;16(14):1671-1681. doi:10.2174/1389450115666140804124808

40. Mura S, Couvreur P. Advanced Drug Delivery Comentarios. *Adv Drug Deliv Rev*. 2012;64(13):1394-1416. doi:10.1016/j.addr.2012.06.006

41. Janjic JM, Ahrens ET. Fluorine-containing nanoemulsions for MRI cell tracking. *Wiley Interdiscip Rev Nanomed Nanobiotechnol*. 2009;1(5):492-501. doi:10.1002/wnan.35

42. Patel SK, Patrick MJ, Pollock JA, Janjic JM. Two-color fluorescent (near-infrared and visible) triphasic perfluorocarbon nanoemuslions. *J Biomed Opt*. 2013;18(10):101312. doi:10.1117/1.JBO.18.10.101312

43. O'Hanlon CE, Amede KG, O'Hear MR, Janjic JM. NIR-labeled perfluoropolyether nanoemulsions for drug delivery and imaging. *J Fluor Chem*. 2012;137:27-33. doi:10.1016/j.jfluchem.2012.02.004

44. Patel SK, Zhang Y, Pollock JA, Janjic JM. Cyclooxgenase-2 inhibiting perfluoropoly (ethylene glycol) ether theranostic nanoemulsions-in vitro study. *PLoS One*. 2013;8(2):e55802. doi:10.1371/journal.pone.0055802

45. Liu L, Bagia C, Janjic JM. The First Scale-Up Production of Theranostic Nanoemulsions. *Biores Open Access*. 2015;4(1):218-228. doi:10.1089/biores.2014.0030

46. Janjic JM. Inflammation Targeted Nanomedicine: A perspective on the promise and potential of biomedical technologies for pain diagnosis and management. *Pract Pain Manag*. April 2019:33-35. https://www.practicalpainmanagement.com/treatments/inflammation-targeted-nanomedicine.

47. Allen TM, Cullis PR. Liposomal drug delivery systems: From concept to clinical applications. *Adv Drug Deliv Rev*. 2013;65(1):36-48. doi:10.1016/j.addr.2012.09.037

48. Crucho CIC, Barros MT. Polymeric nanoparticles: A study on the preparation variables and characterization methods. *Mater Sci Eng C*. 2017;80:771-784. doi:10.1016/j.msec.2017.06.004

49. Kabanov A V, Vinogradov S V. Nanogels as pharmaceutical carriers: Finite networks of infinite capabilities. *Angew Chemie - Int Ed*. 2009;48(30):5418-5429. doi:10.1002/anie.200900441

50. Sarim Imam S, Ali A, Gull A, Aqil M, Ahmed S, Zafar A. In vitro and preclinical assessment of factorial design based nanoethosomes transgel formulation of an opioid analgesic. *Artif Cells, Nanomedicine, Biotechnol*. 2015;44(8):1793-1802.

doi:10.3109/21691401.2015.1102742

51. Borrelli DA, Yankson K, Shukla N, Vilanilam G, Ticer T, Wolfram J. Extracellular vesicle therapeutics for liver disease. *J Control Release*. 2018;273:86-98. doi:10.1016/j.jconrel.2018.01.022

52. Zhang T, Cui H, Forrest ML. Metal nanoparticles. In: *NANOPARTICLES FOR BIOTHERAPEUTIC DELIVERY (VOLUME 2)*. ; 2015. doi:10.4155/fseb2013.14.7

53. Corr SA. Metal oxide nanoparticles. In: *SPR Nanoscience: Volume 3*. Royal Society of Chemistry; 2016. doi:10.1039/9781782623717-00031

54. Qian Z, Li L, Gao X, et al. Delivering instilled hydrophobic drug to the bladder by a cationic nanoparticle and thermo-sensitive hydrogel composite system. *Nanoscale*. 2012;4(20):6425. doi:10.1039/c2nr31592k

55. Pelaz B, Alexiou C, Alvarez-Puebla RA, et al. Diverse Applications of Nanomedicine. *ACS Nano*. 2017;11(3):2313-2381. doi:10.1021/acsnano.6b06040

56. Mountain GA, Jelier BJ, Bagia C, Friesen CM, Janjic JM. Design and formulation of nanoemulsions using 2-(poly(hexafluoropropylene oxide)) perfluoropropyl benzene in combination with linear perfluoro(polyethylene glycol dimethyl ether). *J Fluor Chem*. 2014;162:38-44. doi:10.1016/j.jfluchem.2014.03.007

57. Patel SK, Beaino W, Anderson CJ, Janjic JM. Theranostic nanoemulsions for macrophage COX-2 inhibition in a murine inflammation model. *Clin Immunol*. 2015;160(1):59-70. doi:10.1016/j.clim.2015.04.019

58. Puri A, Loomis K, Smith B, et al. Lipid-based nanoparticles as pharmaceutical drug carriers: from concepts to clinic. *Crit Rev Ther Drug Carrier Syst*. 2009;26(6):523-580. http://www.ncbi.nlm.nih.gov/pubmed/20402623. Accessed March 28, 2019.

59. Panahi Y, Farshbaf M, Mohammadhosseini M, et al. Recent advances on liposomal nanoparticles: synthesis, characterization and biomedical applications. *Artif Cells, Nanomedicine Biotechnol*. 2017;45(4):788-799. doi:10.1080/21691401.2017.1282496

60. Mizushima Y. Lipid microspheres (lipid emulsions) as a drug carrier - An overview. *Adv Drug Deliv Rev*. 1996;20(2-3):113-115. doi:10.1016/0169-409X(95)00114-M

61. Bardania H, Tarvirdipour S, Dorkoosh F. Liposome-targeted delivery for highly potent drugs. *Artif Cells, Nanomedicine Biotechnol*. 2017;45(8):1478-1489. doi:10.1080/21691401.2017.1290647

62. Zhou J, Wu W, Caruntu D, et al. Synthesis of porous magnetic hollow silica nanospheres for nanomedicine application. *J Phys Chem C*. 2007;111(47):17473-17477. doi:10.1021/jp074123i

63. Contri R V, Frank LA, Kaiser M, Pohlmann AR, Guterres SS. The use of

nanoencapsulation to decrease human skin irritation caused by capsaicinoids. *Int J Nanomedicine*. 2014;9(1):951-962. doi:10.2147/IJN.S56579

64. Kolker SJ, Quintans JSS, Scotti MT, et al. Nanoemulsion Thermoreversible Pluronic F127-Based Hydrogel Containing Hyptis pectinata (Lamiaceae) Leaf Essential Oil Produced a Lasting Anti-hyperalgesic Effect in Chronic Noninflammatory Widespread Pain in Mice. *Mol Neurobiol*. 2017;55(2):1665-1675. doi:10.1007/s12035-017-0438-1

65. Shen S, Wu Y, Liu Y, Wu D. High drug-loading nanomedicines: Progress, current status, and prospects. *Int J Nanomedicine*. 2017;12:4085-4109. doi:10.2147/IJN.S132780

66. Bordat A, Boissenot T, Nicolas J, Tsapis N. Thermoresponsive polymer nanocarriers for biomedical applications. *Adv Drug Deliv Rev*. 2019;138:167-192. doi:10.1016/j.addr.2018.10.005

67. Benjaminsen R V., Sun H, Henriksen JR, Christensen NM, Almdal K, Andresen TL. Evaluating nanoparticle sensor design for intracellular pH measurements. *ACS Nano*. 2011;5(7):5864-5873. doi:10.1021/nn201643f

68. Suk JS, Xu Q, Kim N, Hanes J, Ensign LM. PEGylation as a strategy for improving nanoparticle-based drug and gene delivery. *Adv Drug Deliv Rev*. 2016;99(Pt A):28-51. doi:10.1016/j.addr.2015.09.012

69. Kwong B, Gai SA, Elkhader J, Wittrup KD, Irvine DJ. Localized immunotherapy via liposome-anchored anti- CD137 + IL-2 prevents lethal toxicity and elicits local and systemic antitumor immunity. *Cancer Res*. 2013;73(5):1547-1558. doi:10.1158/0008-5472.CAN-12-3343

70. Lee K, Conboy M, Park HM, et al. Nanoparticle delivery of Cas9 ribonucleoprotein and donor DNA in vivo induces homology-directed DNA repair. *Nat Biomed Eng*. 2017;1:889-901. doi:10.1038/s41551-017-0137-2

71. Kadayakkara DK, Janjic JM, Pusateri LK, Young WB, Ahrens ET. In vivo observation of intracellular oximetry in perfluorocarbon-labeled glioma cells and chemotherapeutic response in the CNS using fluorine-19 MRI. *Magn Reson Med*. 2010;64(5):1252-1259. doi:10.1002/mrm.22506

72. Janjic JM, Patel SK, Patrick MJ, Pollock JA, DiVito E, Cascio M. Suppressing inflammation from inside out with novel NIR visible perfluorocarbon nanotheranostics. In: *Reporters, Markers, Dyes, Nanoparticles, and Molecular Probes for Biomedical Applications V*. San Francisco, California: SPIE; 2013:85960L. doi:10.1117/12.2004625

73. Feng J, Lepetre-Mouelhi S, Gautier A, et al. A new painkiller nanomedicine to bypass the blood-brain barrier and the use of morphine. *Sci Adv*. 2019;5(2):eaau5148. doi:10.1126/sciadv.aau5148

74. Stern P, Roberts L. The future of pain research. *Science (80-)*. 2016;354(6312):564-565. doi:10.1126/science.354.6312.564

75. Berrocoso E, Rey-Brea R, Fernández-Arévalo M, Micó JA, Martín-Banderas L. Single oral dose of cannabinoid derivate loaded PLGA nanocarriers relieves neuropathic pain for eleven days. *Nanomedicine Nanotechnology, Biol Med*. 2017;13(8):2623-2632. doi:10.1016/j.nano.2017.07.010

76. Liu H, Yuan H, Wu B, et al. Nanoparticle-Encapsulated Curcumin Inhibits Diabetic Neuropathic Pain Involving the P2Y12 Receptor in the Dorsal Root Ganglia. *Front Neurosci*. 2018;11:755. doi:10.3389/fnins.2017.00755

77. Sorge RE, Totsch SK. Sex Differences in Pain. *J Neurosci Res*. 2017;95(6):1271-1281. doi:10.1002/jnr.23841

78. Klein SL, Flanagan KL. Sex differences in immune responses. *Nat Rev Immunol*. 2016;16(10):626-638. doi:10.1038/nri.2016.90

79. Hawkey CJ. COX-1 and COX-2 inhibitors. *Best Pract Res Clin Gastroenterol*. 2001;15(5):801-820. doi:10.1053/bega.2001.0236

80. Holness CL, Simmons DL. Molecular cloning of CD68, a human macrophage marker related to lysosomal glycoproteins. *Blood*. 1993;81(6):1607-1613.

81. Forsythe P, Bienenstock J. The mast cell- nerve functional unit: A key component of physiologic and pathophysiologic responses. *Allergy Nerv Syst*. 2012;98:196-221. doi:10.1159/000336523

82. Chatterjea D, Martinov T. Mast cells: Versatile gatekeepers of pain. *Mol Immunol*. 2015;63(1):38-44. doi:10.1016/j.molimm.2014.03.001

83. Wernersson S, Pejler G. Mast cell secretory granules: Armed for battle. *Nat Rev Immunol*. 2014;14(7):478-494. doi:10.1038/nri3690

84. Italiani P, Boraschi D. From monocytes to M1/M2 macrophages: Phenotypical vs. functional differentiation. *Front Immunol*. 2014;5:514. doi:10.3389/fimmu.2014.00514

85. Najafi M, Hashemi Goradel N, Farhood B, et al. Macrophage polarity in cancer: A review. *J Cell Biochem*. 2019;120(3):2756-2765. doi:10.1002/jcb.27646

86. Becker L, Liu NC, Averill MM, et al. Unique proteomic signatures distinguish macrophages and dendritic cells. *PLoS One*. 2012;7(3):e33297. doi:10.1371/journal.pone.0033297

87. Saleem M, Deal B, Nehl E, Janjic JM, Pollock JA. Nanomedicine-driven neuropathic pain relief in a rat model is associated with macrophage polarity and mast cell activation. *Acta Neuropathol Commun*. 2019;7(1):108. doi:10.1186/s40478-019-0762-y

88. Pepys MB, Gordon S, Helming L, et al. Multinucleated Giant Cells Are Specialized for Complement-Mediated Phagocytosis and Large Target Destruction. *Cell Rep*. 2015;13(9):1937-1948. doi:10.1016/j.celrep.2015.10.065

89. Chaplan SR, Bach FW, Pogrel JW, Chung JM, Yaksh TL. Quantitative assessment of tactile allodynia in the rat paw. *J Neurosci Methods*. 1994;53(1):55-63. doi:10.1016/0165-0270(94)90144-9

90. Saleem M, Stevens AM, Deal B, Liu L, Janjic J, Pollock JA. A New Best Practice for Validating Tail Vein Injections in Rat with Near-infrared-Labeled Agents. *J Vis Exp*. 2019;8(146):e59295. doi:10.3791/59295

91. Sebestyén MG, Budker VG, Budker T, et al. Mechanism of plasmid delivery by hydrodynamic tail vein injection. I. Hepatocyte uptake of various molecules. *J Gene Med*. 2006;8(7):852-873. doi:10.1002/jgm.921

92. Budker VG, Subbotin VM, Budker T, Sebestyén MG, Zhang G, Wolff JA. Mechanism of plasmid delivery by hydrodynamic tain vein injection. II. Morphological studies. *J Gene Med*. 2006;8(7):874-888. doi:10.1002/jgm.920

93. Lecocq M, Andrianaivo F, Warnier MT, Wattiaux-De Coninck S, Wattiaux R, Jadot M. Uptake by mouse liver and intracellular fate of plasmid DNA after a rapid tail vein injection of a small or a large volume. *J Gene Med*. 2003;5(2):142-156. doi:10.1002/jgm.328

94. Park S, Park H-M, Sun S-H. Single-dose Intravenous Injection Toxicity of Water-soluble Danggui Pharmacopuncture (WDP) in Sprague-Dawley Rats. *J pharmacopuncture*. 2018;21(2):104-111. doi:10.3831/KPI.2018.21.013

95. Zhang X, Nakajima T, Kim M, et al. Activatable fluorescence detection of epidermal growth factor receptor positive mediastinal lymph nodes in murine lung cancer model. *PLoS One*. 2018;13(6):e0198224. doi:10.1371/journal.pone.0198224

96. Liu G, Lv H, An Y, Wei X, Yi X, Yi H. Tracking of transplanted human umbilical cord-derived mesenchymal stem cells labeled with fluorescent probe in a mouse model of acute lung injury. *Int J Mol Med*. 2018;41(5):2527-2534. doi:10.3892/ijmm.2018.3491

97. Schindelin J, Arganda-Carreras I, Frise E, et al. Fiji: an open-source platform for biological-image analysis. *Nat Methods*. 2012;9(7):676-682. doi:10.1038/nmeth.2019

98. Sarker DK. Engineering of nanoemulsions for drug delivery. *Curr Drug Deliv*. 2005;2(4):297-310. https://www.ncbi.nlm.nih.gov/pubmed/16305433.

99. McClements DJ, Rao J. Food-Grade Nanoemulsions: Formulation, Fabrication, Properties, Performance, Biological Fate, and Potential Toxicity. *Crit Rev Food Sci Nutr*. 2011;51(4):285-330. doi:10.1080/10408398.2011.559558

100. Rajpoot P, Pathak K, Bali V. Therapeutic applications of nanoemulsion based drug delivery systems: a review of patents in last two decades. *Recent Pat Drug Deliv Formul*. 2011;5(2):163-172. https://www.ncbi.nlm.nih.gov/pubmed/21361870.

101. Kotta S, Khan AW, Pramod K, Ansari SH, Sharma RK, Ali J. Exploring oral

nanoemulsions for bioavailability enhancement of poorly water-soluble drugs. *Expert Opin Drug Deliv*. 2012;9(5):585-598. doi:10.1517/17425247.2012.668523

102. Shakeel F, Shafiq S, Haq N, Alanazi FK, Alsarra IA. Nanoemulsions as potential vehicles for transdermal and dermal delivery of hydrophobic compounds: an overview. *Expert Opin Drug Deliv*. 2012;9(8):953-974. doi:10.1517/17425247.2012.696605

103. Mitri K, Vauthier C, Huang N, et al. Scale-up of nanoemulsion produced by emulsification and solvent diffusion. *J Pharm Sci*. 2012;101(11):4240-4247. doi:10.1002/jps.23291

104. Muller RH, Harden D, Keck CM. Development of industrially feasible concentrated 30% and 40% nanoemulsions for intravenous drug delivery. *Drug Dev Ind Pharm*. 2012;38(4):420-430. doi:10.3109/03639045.2011.608681

105. Sacerdote P, Franchi S, Moretti S, et al. Cytokine modulation is necessary for efficacious treatment of experimental neuropathic pain. *J Neuroimmune Pharmacol*. 2013;8(1):202-211. doi:10.1007/s11481-012-9428-2

106. Barabas ME, Mattson EC, Aboualizadeh E, Hirschmugl CJ, Stucky CL. Chemical structure and morphology of dorsal root ganglion neurons from naive and inflamed mice. *J Biol Chem*. 2014;289(49):34241-34249. doi:10.1074/jbc.M114.570101

107. Collington SJ, Williams TJ, Weller CL. Mechanisms underlying the localisation of mast cells in tissues. *Trends Immunol*. 2011;32(10):478-485. doi:10.1016/j.it.2011.08.002

108. Schafers M, Marziniak M, Sorkin LS, Yaksh TL, Sommer C. Cyclooxygenase inhibition in nerve-injury- and TNF-induced hyperalgesia in the rat. *Exp Neurol*. 2004;185(1):160-168. https://www.ncbi.nlm.nih.gov/pubmed/14697327.

109. Wang Y, Zhang X, Guo QL, Zou WY, Huang CS, Yan JQ. Cyclooxygenase inhibitors suppress the expression of P2X(3) receptors in the DRG and attenuate hyperalgesia following chronic constriction injury in rats. *Neurosci Lett*. 2010;478(2):77-81. doi:10.1016/j.neulet.2010.04.069

110. Bailard NS, Ortiz J, Flores RA. Additives to local anesthetics for peripheral nerve blocks: Evidence, limitations, and recommendations. *Am J Heal Pharm*. 2014;71(5):373-385. doi:10.2146/ajhp130336

111. Opperer M, Gerner P, Memtsoudis SG. Additives to local anesthetics for peripheral nerve blocks or local anesthesia: a review of the literature. *Pain Manag*. 2015;5(2):117-128. doi:10.1103/PhysRev.96.1460

112. Hashimoto A, Ito H, Harato M, Fujiwara Y, Komatsu T. Complications of peripheral nerve block. *Japanese J Anesthesiol*. 2011;60(1):111-119. doi:10.1053/j.trap.2007.05.004

113. Moore RA, Chi CC, Wiffen PJ, Derry S, Rice ASC. Oral nonsteroidal anti-inflammatory drugs for neuropathic pain. *Cochrane Database Syst Rev*. 2015;10:CD010902.

doi:10.1002/14651858.CD010902.pub2

114. Kieffer BL, Evans CJ. Opioid receptors: From binding sites to visible molecules in vivo. *Neuropharmacology*. 2009;56 Suppl 1:205-212. doi:10.1016/j.neuropharm.2008.07.033

115. Stoeber M, Jullié D, Lobingier BT, et al. A Genetically Encoded Biosensor Reveals Location Bias of Opioid Drug Action. *Neuron*. 2018;98(5):963-976.e5. doi:10.1016/j.neuron.2018.04.021

116. Lai SM, Sheng J, Gupta P, et al. Organ-Specific Fate, Recruitment, and Refilling Dynamics of Tissue-Resident Macrophages during Blood-Stage Malaria. *Cell Rep*. 2018;25(11):3099-3109.e3. doi:10.1016/j.celrep.2018.11.059

117. Swirski FK, Nahrendorf M, Etzrodt M, et al. Identification of splenic reservoir monocytes and their deployment to inflammatory sites. *Science (80-)*. 2009;325(5940):612-616. doi:10.1126/science.1175202

118. Konishi H, Kiyama H, Okamoto T, Suzuki A, Namikawa K. Pancreatitis-Associated Protein-III Is a Novel Macrophage Chemoattractant Implicated in Nerve Regeneration. *J Neurosci*. 2006;26(28):7460-7467. doi:10.1523/jneurosci.0023-06.2006

119. Chen P, Piao X, Bonaldo P. Role of macrophages in Wallerian degeneration and axonal regeneration after peripheral nerve injury. *Acta Neuropathol*. 2015;130(5):605-618. doi:10.1007/s00401-015-1482-4

120. Jeong SR, Kim J, Hwang DH, et al. Contribution of Macrophages to Enhanced Regenerative Capacity of Dorsal Root Ganglia Sensory Neurons by Conditioning Injury. *J Neurosci*. 2013;33(38):15095-15108. doi:10.1523/jneurosci.0278-13.2013

121. Amulic B, Cazalet C, Hayes GL, Metzler KD, Zychlinsky A. Neutrophil Function: From Mechanisms to Disease. *Annu Rev Immunol*. 2012;30:459-489. doi:10.1146/annurev-immunol-020711-074942

122. Hitchens TK, Ye Q, Eytan DF, Janjic JM, Ahrens ET, Ho C. 19F MRI detection of acute allograft rejection with in vivo perfluorocarbon labeling of immune cells. *Magn Reson Med*. 2011;65(4):1145-1154. doi:10.1002/mrm.22702

123. Novikov DS, Kiselev VG, Jespersen SN. On modeling. *Magn Reson Med*. 2018;79(6):3172-3193. doi:10.1002/mrm.27101

124. Shin SH, Park EJ, Min C, et al. Tracking perfluorocarbon nanoemulsion delivery by 19FMRI for precise high intensity focused ultrasound tumor ablation. *Theranostics*. 2017;7(3):562-572. doi:10.7150/thno.16895

125. Rosales C. Neutrophil: A cell with many roles in inflammation or several cell types? *Front Physiol*. 2018;9:113. doi:10.3389/fphys.2018.00113

126. Delavary BM, van der Veer WM, van Egmond M, Niessen FB, Beelen RHJ. Macrophages

in skin injury and repair. *Immunobiology*. 2011;216(7):753-762. doi:10.1016/j.imbio.2011.01.001

127. Koh TJ, DiPietro LA. Inflammation and wound healing: the role of the macrophage. *Expert Rev Mol Med*. 2011;13:e23. doi:10.1017/S1462399411001943

128. Mantovani A, Biswas SK, Galdiero MR, Sica A, Locati M. Macrophage plasticity and polarization in tissue repair and remodelling. *J Pathol*. 2013;229(2):176-185. doi:10.1002/path.4133

129. Qian Y. Mast Cells and Neuroinflammation. *Med Sci Monit Basic Res*. 2014;20:200-206. doi:10.12659/msmbr.893093

130. Chen R, Fairley JA, Zhao M-L, et al. The Journal of Immunology. *J Immunol*. 2002;150(12):5585-5595. doi:10.4049/jimmunol.169.7.3987

131. Rodgers K, Xiong S. Contributions of inflammatory mast cell mediators to alterations in macrophage function after malathion administration. *Int J Immunopharmacol*. 1997;19(3):149-156. http://www.ncbi.nlm.nih.gov/pubmed/9306154. Accessed May 16, 2019.

132. Aich A, Afrin LB, Gupta K. Mast Cell-Mediated Mechanisms of Nociception. *Int J Mol Sci*. 2015;16(12):29069-29092. doi:10.3390/ijms161226151

133. Zhang XC, Kainz V, Burstein R, Levy D. Tumor necrosis factor-α induces sensitization of meningeal nociceptors mediated via local COX and p38 MAP kinase actions. *Pain*. 2011;152(1):140-149. doi:10.1016/j.pain.2010.10.002

134. Zhang X, Burstein R, Levy D. Local action of the proinflammatory cytokines IL-1β and IL-6 on intracranial meningeal nociceptors. *Cephalalgia*. 2012;32(1):66-72. doi:10.1177/0333102411430848

135. Levy D, Kainz V, Burstein R, Strassman AM. Mast cell degranulation distinctly activates trigemino-cervical and lumbosacral pain pathways and elicits widespread tactile pain hypersensitivity. *Brain Behav Immun*. 2012;26(2):311-317. doi:10.1016/j.bbi.2011.09.016

136. Vergnolle N, Wallace JL, Bunnett NW, Hollenberg MD. Protease-activated receptors in inflammation, neuronal signaling and pain. *Trends Pharmacol Sci*. 2001;22(3):146-152. doi:10.1016/S0165-6147(00)01634-5

137. Cobos EJ, Nickerson CA, Gao F, et al. Mechanistic Differences in Neuropathic Pain Modalities Revealed by Correlating Behavior with Global Expression Profiling. *Cell Rep*. 2018;22(5):1301-1312. doi:10.1016/j.celrep.2018.01.006

138. Hu P, McLachlan EM. Macrophage and lymphocyte invasion of dorsal root ganglia after peripheral nerve lesions in the rat. *Neuroscience*. 2002;112(1):23-38. doi:10.1016/S0306-4522(02)00065-9

139. Moalem G, Tracey DJ. Immune and inflammatory mechanisms in neuropathic pain. *Brain Res Rev*. 2006;51(2):240-264. doi:10.1016/J.BRAINRESREV.2005.11.004

140. Vega-Avelaira D, Géranton SM, Fitzgerald M. Differential Regulation of Immune Responses and Macrophage/Neuron Interactions in the Dorsal Root Ganglion in Young and Adult Rats following Nerve Injury. *Mol Pain*. 2009;5(1):1744-8069-5-70. doi:10.1186/1744-8069-5-70

141. Xanthos DN, Sandkühler J. Neurogenic neuroinflammation: Inflammatory CNS reactions in response to neuronal activity. *Nat Rev Neurosci*. 2014;15(1):43-53. doi:10.1038/nrn3617

142. Sorge RE, LaCroix-Fralish ML, Tuttle AH, et al. Spinal Cord Toll-Like Receptor 4 Mediates Inflammatory and Neuropathic Hypersensitivity in Male But Not Female Mice. *J Neurosci*. 2011;31(43):15450-15454. doi:10.1523/jneurosci.3859-11.2011

143. Mapplebeck JCS, Dalgarno R, Tu YS, et al. Microglial P2X4R-evoked pain hypersensitivity is sexually dimorphic in rats. *Pain*. 2018;159(9):1752-1763. doi:10.1097/j.pain.0000000000001265

144. Sorge RE, Mapplebeck JCS, Rosen S, et al. Different immune cells mediate mechanical pain hypersensitivity in male and female mice. *Nat Neurosci*. 2015;18(8):1081-1083. doi:10.1038/nn.4053

145. Rosen SF, Ham B, Drouin S, et al. T-Cell Mediation of Pregnancy Analgesia Affecting Chronic Pain in Mice. *J Neurosci*. 2017;37(41):9819-9827. doi:10.1523/jneurosci.2053-17.2017

146. Nag S, Mokha SS. Testosterone is essential for α2-adrenoceptor-induced antinociception in the trigeminal region of the male rat. *Neurosci Lett*. 2009;467(1):48-52. doi:10.1016/j.neulet.2009.10.016

147. Aloisi AM, Bachiocco V, Costantino A, et al. Cross-sex hormone administration changes pain in transsexual women and men. *Pain*. 2007;132(SUPPL. 1):S60-7. doi:10.1016/j.pain.2007.02.006

148. North RY, Li Y, Ray P, et al. Electrophysiological and transcriptomic correlates of neuropathic pain in human dorsal root ganglion neurons. *Brain*. 2019;142(5):1215-1226. doi:10.1093/brain/awz063

149. Becker L, Liu N-C, Averill MM, Yuan W, Pamir N. Unique Proteomic Signatures Distinguish Macrophages and Dendritic Cells. *PLoS One*. 2012;7(3):e33297. doi:10.1371/journal.pone.0033297

150. Landhuis E. Single-cell approaches to immune profiling technology-feature. *Nature*. 2018;557(7706):595-597. doi:10.1038/d41586-018-05214-w

151. Franchi L, Eigenbrod T, Muñoz-Planillo R, Nuñez G. The inflammasome: A caspase-1-

activation platform that regulates immune responses and disease pathogenesis. *Nat Immunol*. 2009;10(3):241-247. doi:10.1038/ni.1703

152. Hua KF, Chou JC, Ka SM, et al. Cyclooxygenase-2 regulates NLRP3 inflammasome-derived IL-1β production. *J Cell Physiol*. 2015;230(4):863-874. doi:10.1002/jcp.24815